

Electronic Theses and Dissertations, 2004-2019

2004

Stable Spatial Solitons In Semiconductor Optical Amplifiers

Erdem Ultanir
University of Central Florida

 Part of the [Electromagnetics and Photonics Commons](#), and the [Optics Commons](#)
Find similar works at: <https://stars.library.ucf.edu/etd>
University of Central Florida Libraries <http://library.ucf.edu>

This Doctoral Dissertation (Open Access) is brought to you for free and open access by STARS. It has been accepted for inclusion in Electronic Theses and Dissertations, 2004-2019 by an authorized administrator of STARS. For more information, please contact STARS@ucf.edu.

STARS Citation

Ultanir, Erdem, "Stable Spatial Solitons In Semiconductor Optical Amplifiers" (2004). *Electronic Theses and Dissertations, 2004-2019*. 42.
<https://stars.library.ucf.edu/etd/42>

**STABLE SPATIAL SOLITONS IN SEMICONDUCTOR
OPTICAL AMPLIFIERS**

by

ERDEM ULTANIR
B.S. Bilkent University, 1999
M.S. University of Central Florida, 2001

A dissertation submitted in partial fulfillment of the requirements
for the degree of Doctor of Philosophy
in the College of Optics and Photonics
at the University of Central Florida
Orlando, Florida

Fall Term
2004

© 2004 Erdem Ultanir

ABSTRACT

A spatial soliton is a shape invariant self guided beam of light or a self induced waveguide. Spatial solitons appear as a result of the balance of diffraction and nonlinear focusing in a system. They have been observed in many different *conservative* media in the last couple of years. Solitons are ubiquitous, because of the probability of using their interactions in optical data processing, communications etc. Up to now due to the power required to generate the solitons, and the response times of the soliton supporting media, these special waves of nature could not penetrate the applications arena. Semiconductors, with their resonant nonlinearities, are thought to be ideal candidates for fast switching, low power spatial solitons.

In this dissertation it is shown theoretically and experimentally that it is possible to observe stable spatial solitons in a periodically patterned semiconductor optical amplifier (PPSOA). The solitons have unique beam profiles that change only with system parameters, like pumping current, etc. Their coherent and incoherent interactions which could lead to all optical devices have been investigated experimentally and theoretically. The formation of filaments or modulational instability has been studied theoretically and yielded analytical formulae for evaluating the filament gain and the maximum spatial frequencies in PPSOA devices. Furthermore, discrete array amplifiers have been analyzed numerically for discrete solitons, and the prospect of using multi peak discrete solitons as laser amplifiers is discussed.

To my parents; Gurcan and Emel Ultanir

ACKNOWLEDGEMENTS

I started my PhD studies in CREOL at the end of the summer of 1999. I remember the first day I came to the building. The middle of August, a humid Florida summer day... Since I did not have a car, I walked to the campus through the University Blvd entrance, passed the Milican Hall and the fountain pool in front of the library. Ohhh, such a warm day it was; after leaving behind the science building, I remember it was like I took a shower- first lesson; never walk outside in FL sunshine-. Then I entered the freezing cold CREOL building, which was going to be my home for the next 5 years.

Although the building was always cold; except a couple of times with air conditioning problems, the people in this building were the most kindly, the warmest people I have ever met. It is impossible for me to thank all of them one by one, but I would like to mention couple of individuals in this building whom I am really indebted to.

George I. Stegeman; my utmost teacher, as he will always say; he believed in me, and encouraged me to stay focused on the project, even though I had difficult times. Thanks George, it was great to be in your group, and I am honored to be one of your young pupils. For the historical records, during my PhD studies, George I. Stegeman had nine optical laboratories that are full of tons of optical equipment, bunch of lasers on and even below the optical benches, access to clean room facilities, collaborations with numerous great scientists from all around the world. Such a great place to be...

I am also grateful to the Falk Lederer's group in University Jena. The idea of using periodical patterning was the result of the help that I got from Dirk Michaelis and Dr. Lederer, during my visit to their group in the summer of 2001. The invaluable discussions with Dr Christodoulides helped me to generate ideas in the final stages of my dissertation, moreover it was a great motivation to have him here in Creol and to discuss about optics, scientific approach and life. Many thanks to Dr LiKamWa and his group; I learned a lot from them about the fabrication techniques.

Many friends that I will always remember in alphabetical order; Bojan, Ferenc, Fumy, George, Joachim, Kostas, Ozan, Robert, and Waleed. Thank you all...

TABLE OF CONTENTS

LIST OF FIGURES.....	x
CHAPTER ONE: INTRODUCTION.....	1
1.1 Introduction.....	1
1.2 Scope of Research.....	5
CHAPTER TWO: SOA THEORY	9
2.1 Introduction.....	9
2.2 Semiconductor Physics	9
2.3 SOA modeling equations	16
2.4 Soliton Solutions and Their Stability	22
2.5 Conclusions.....	30
CHAPTER THREE: DISSIPATIVE SOLITON EXPERIMENT.....	31
3.1 Introduction.....	31
3.2 Solitons in QW semiconductors.....	31
3.3 Device fabrication.....	37
3.4 Initial Experiments.....	43

3.5 Comparison of InGaAs and InP based QW devices for dissipative soliton experiments...	51
3.6 Conclusions.....	53
CHAPTER FOUR: DISSIPATIVE SOLITON INTERACTIONS.....	54
4.1 Introduction.....	54
4.2 Dissipative nonlocal effects	56
4.3 Conclusions.....	66
CHAPTER FIVE: MODULATION INSTABILITY	67
5.1 Introduction.....	67
5.2 Theory and Simulations	68
5.3 Discussion of Experimental Possibilities.....	76
5.4 Conclusions.....	80
CHAPTER SIX: DISSIPATIVE DISCRETE SOLITONS	81
6.1 Introduction.....	81
6.2 Discrete Dissipative Solitons	88
6.3 Conclusions.....	95
CHAPTER SEVEN: INCOHERENT INTERACTIONS	96
7.1 Introduction.....	96

7.2 Incoherent Interactions in Gain Systems	99
7.3 Conclusions.....	108
CHAPTER EIGHT: CONCLUSIONS.....	109
LIST OF REFERENCES.....	111

LIST OF FIGURES

Figure 1.1 Diffraction of electron beams is related to the uncertainty principle	2
Figure 1.2 Liquid Crystal Solitons (a) the diffraction of a helium neon laser beam imaged from the top of the cell (b) spatial soliton when the nonlinearity of the liquid crystal is turned on by application of an electric field [1.2].....	3
Figure 2.1 Semiconductor heterojunction, p-p-n structure. The Fermi levels of the semiconductor align and form the barriers. When this device is forward biased, holes from the first semiconductor and electrons from the third semiconductor will enter the second semiconductor, and their recombination will occur in the middle region. In addition to these effects, generally the semiconductors with low bandgap energies, have higher refractive indices than the large bandgap energy semiconductors. This allows the optical confinement of light in the middle of the heterostructure.....	13
Figure 2.2 The refractive index (Δn) and absorption coefficient ($\Delta\alpha$) change as the absorption spectrum changes from the dashed line to solid line.	15
Figure 2.3, Semiconductor Optical Amplifier	17
Figure 2.4 The change in net modal power gain (a) and linewidth enhancement factor (b) of a InGaAs SQW semiconductor laser diode. The curve values increase with the sheet carrier densities given as 1.7×10^{12} , 3.5×10^{12} and 4.6×10^{12} cm^{-2} [from Ref. 2.11].....	20
Figure 2.5 Dissipative soliton profile showing that a dissipative soliton has regions of gain and loss over its field profile which balance to produce a stationary field profile.....	23

Figure 2.6	SOA bifurcation diagram	25
Figure 2.7	Propagation of an initially localized soliton-like solution in a uniformly pumped SOA; The solution is unstable and evolves into filament-like structures because of numerical noise in the simulation.....	25
Figure 2.8	Model device, with periodic contact pads (Openings on the top layer of the device could be used for current injection)	26
Figure 2.9	a) Gain and loss of the system vs. field intensity. The dotted curve shows the saturating loss (considered here as negative gain) in the non-pumped region, and the dashed curve is the saturated gain in the pumped region. The solid line represents the sum of these two contributions including the internal linear losses of the system, b) The PW and soliton bifurcation diagrams vs. δG . The thick solid line shows the PW solutions that subcritically bifurcate from the trivial solution. Between zero gain and the turning point the solution with negative slope is unstable. The dashed line indicates the peak intensity of the stable soliton which has a fine beam width along x axis. This branch terminates because of Hopf instabilities. The dotted line is the unstable trivial PW solution at positive small signal gain, and the thin solid line is the stable zero PW solutions. The fields shown here are averaged over the pumped and un-pumped segments.....	28
Figure 2.10	a) Soliton amplitude (solid line) and phase profile (dashed line). b) Evolution at δG =-0.106, of a 179.2 mW total power input beam with a constant phase, a sech^2 intensity distribution, and a 37.5 μm beam waist (FWHM) into a 24.5 μm beam waist (FWHM), 181.4 mW spatial soliton, using normalized parameters ($B=0.7, C=0.005, D=1.56, \alpha=0.067$).	30
Figure 3.1	Wafer structure is a single quantum well p-n junction waveguide.	32

Figure 3.2 Plot of the peak field level($\sqrt{mW / \mu m}$) of the solitons versus the small signal gain δG . The dashed line shows the unstable solutions, and the dark line shows the stable solitons Current values (horizontal axis-top scale) are calculated assuming 300 μm width contact patterns on a 1cm long device.	37
Figure 3.3 Current vs power and voltage characteristics of broad area diodes with SQW wafer grown in Jena.	38
Figure 3.4 The transverse and lateral mode profiles of broad area gain guided laser diodes for the SQW wafer grown in Jena.	39
Figure 3.5 Device fabrication steps: first samples are cleaved & cleaned; then the insulator is deposited followed by lithography and contact deposition.....	40
Figure 3.6 An optical microscope image of the top of the device.	42
Figure 3.7 Gold wired device on a TE cooled waveguide stage.....	42
Figure 3.8 The coupling setup	43
Figure 3.9 (Top) Input beam profile at $\lambda=965nm$, fitted to a Gaussian gave FWHM=16.5 μm , (Middle) Diffracted beam (to 62.5 μm FWHM at the output of sample), (Bottom) Output beam profile for $\lambda=950nm$, at 4A current injection.	44
Figure 3.10 (a) Collage of images from the output facet when the measured input at the front facet is 160mW & 16.5 μm FWHM. (b) Collage of numerical simulations of the output profile with a 55mW & 17.5 μm FWHM Gaussian input into the waveguide.....	45
Figure 3.11 The output behavior of the device (shown by red line) on the bifurcation diagram.	46
Figure 3.12 The behavior of the device's output on the bifurcation diagram when the input intensity is changed.....	47

Figure 3.13 (a) Images from the output facet at 4A pumping when the input optical power is increased. (b) Numerical simulation of the solitons at 4A pumping when the input intensity at the front facet is increased (50% coupling is assumed).....	48
Figure 3.14 Output beam waist versus a variable Gaussian input beam width for 160mW input power at the front facet, and 4A current injection.	49
Figure 3.15 Images from the output facet when the measured input at the front facet was 160mW & 16.5 μ m FWHM at wavelengths of (a) 941nm, (b) 946nm and (c) 950nm.....	50
Figure 3.16 Normalized soliton profiles at different gain (g), and linewidth enhancement parameter (h), but at the same current density ($\pi=9.4$). Solid line $g=104\text{cm}^{-1}$, $h=3$; dashed dotted line $g=60\text{cm}^{-1}$, $h=3$; dashed line $g=60\text{cm}^{-1}$, $h=1$	51
Figure 3.17 Left plot shows the powers required for stable solitons vs current. Right plot shows the Gaussian fitted beam waist of the solitons vs current.	52
Figure 4.1 Beam interactions in waveguides could be implemented with phase or amplitude modulators. Moreover defining output channel positions could be used for soliton based optical operations.....	55
Figure 4.2 a) Calculated soliton intensity profile and phase at 4A electrical pumping with the corresponding change (b) in the gain and refractive index in the waveguide. (The gain and refractive index change is calculated with respect to the case when there is no current in the device). (Current $I=\pi q d N_{tr} A_{contact} / \eta$, where $A_{contact} = 300\mu\text{m} \times 1\text{cm} \times 0.5$)	57
Figure 4.3 Experiment setup for investigating dissipative soliton interactions. Setting the distance between the beams and the relative propagation angles was facilitated by mirror M2.	

Moreover M2 was mounted on a piezoelectric stack in order to control the relative phase between the two arms of the interferometer.	58
Figure 4.4 Evolution of the beams due to interactions in the local limit. The two beams interact and after about 3cm propagation, the output intensity of the solitons are the same, because of the zero-parameter property of dissipative solitons. The relative input beam phase is given above the pictures.....	59
Figure 4.5 Output from the sample due to soliton interactions after 1cm propagation. The separation between the input beams is 15 μ m and 22 μ m at the output when each is excited separately. Top picture shows the numerical simulations, and the bottom the experiment results.	60
Figure 4.6 Numerical beam propagation over 3cms of soliton interaction (a) for 0 and (b) π phase difference. The initial separation between the input beams was 60.2 μ m and each had 38 mW power. (c) shows the gain profile around the solitons for 0 phase difference at the input.	62
Figure 4.7 Output from sample due to soliton interactions after 1cm propagation. The separation between the beams when excited separately was 70 μ m at the input and 66 μ m at the output. Top picture shows the numerical simulations, and the bottom gives the experiment results.	63
Figure 4.8 Output from sample due to solitons interacting with crossing trajectories after 1cm of propagation. The separation between the input beams was 56 μ m and the angle between them was 0.5 degrees. Top picture shows the numerical simulations, and the bottom the experiment results.	64

Figure 4.9 Output from sample due to soliton interactions after 1cm propagation. The separation between the input beams was 51 μ m and the separation of the positions of the output beams when separately excited was 50 μ m. Top picture shows the numerical simulations, and the bottom the experiment results..... 65

Figure 5.1 Solutions for the modulational instability gain, k_{zR} , versus spatial frequency “p” of the

perturbations: top plot for the case $k_{zR} = g - \sqrt{g^2 - (\frac{P^4}{4} + p^2hg)}$; the middle for

$k_{zR} = g + \sqrt{g^2 - (\frac{P^4}{4} + p^2hg)}$; and the bottom for $k_{zR} = g$ 73

Figure 5.2 (Left) The growth of the transverse sinusoidal perturbations at a current pumping level of $\pi=50$ ($h=3$), with increases in the propagation distance of 1cm between the curves.

(Right) The gain coefficient at 2 different spatial modulation frequencies. The dashed line shows the gain from Equation 5.15 and solid line is the result from BPM simulations..... 75

Figure 5.3 (a) Modulation gain vs spatial modulation frequency at $h=3$, for different current pumping levels. (b) For a pumping level of $\pi=9.4$, the change in the gain curves with linewidth enhancement factor h 75

Figure 5.4 The configuration of two beams used at the input of the sample to generate MI seeding..... 76

Figure 5.5 Top figure shows the intensity spectrum of the simulations. The bottom figure gives the intensity profile at the input (black line) and the intensity profile after 1cm propagation (blue line)..... 78

Figure 5.6 Contour plot of the modulation gain with propagation distance for a 8mW probe beam..... 79

Figure 5.7 Contour plot of the modulation gain with propagation distance for a 0.4mW probe beam.....	79
Figure 6.1 Ridge waveguide array with a period Λ	84
Figure 6.2 The FB band diagram for a waveguide array with $w_1=3\mu\text{m}$, $w_2=2.5\mu\text{m}$ and $\Delta n = 1.5 \times 10^{-3}$. Left: The index distribution in one lattice period with exponentially decaying tails assumed at the ridge edges which are similar to the experimental conditions. Right: The dispersion relation of FB bands with transverse k-vector (k_x).....	84
Figure 6.3 The FB wave field profiles in the first three bands at $k_x=0$ (a, b, c) and $k_x=\pi$ (d, e, f).	85
Figure 6.4 Proposed discrete PPSOA array structure	88
Figure 6.5 Dissipative lattice soliton (a) field intensity (b) phase (c) discrete phase difference k_x versus transverse distance x in the array. The inset in Figure 6.5(b) depicts an enlargement of the phase structure around the soliton intensity peaks shown in Figure 6.5(b).....	91
Figure 6.6 (a) Normalized soliton propagation constant as a function of pumping. The soliton existence loop lies within the first FB band. (b) Discrete soliton bifurcation diagram. Solid line represents the positive slope-branch whereas the dashed line identifies the unstable negative slope branch. BPM simulations for a soliton (c) on the stable branch at $\pi_0=25$, (d) on the unstable branch at $\pi_0=25$ and (e) on the stable branch at $\pi_0=40$	93
Figure 6.7 Bound lattice soliton intensity profiles ($\sqrt{W/cm}$) for $w_1=3\mu\text{m}$, $w_2=2.5\mu\text{m}$, $\Delta n = 1.5 \times 10^{-3}$, $\pi=25$ (a-c-e) . Figures (b-d-f) show the Fourier spectrum or far-field pattern of the soliton modes corresponding to (a-c-e) respectively.....	94

Figure 7.1 The soliton profiles found by relaxation simulations for a coupled nonlinear Schroedinger equation system given by Equations 7.1. The left figure shows profiles for $\alpha=1.01$ and the right for $\alpha=1.1$. The dashed line is u , and the solid line is v .	98
Figure 7.2 The output images for (a) the TS beam and (b) the LD beam obtained while TS power was increased.	101
Figure 7.3 Simulations of the output from the PPSOA for two color interactions after 1cm of propagation along the sample (a) TS power (b) LD power	104
Figure 7.4 Solid line $ \psi_1 $, dashed line $ \psi_2 $ (a) The peak field values ($\sqrt{mW / \mu m}$) of the two beams, and (b) the fitted sech waists (μm).	105
Figure 7.5 The peak field levels ($\sqrt{mW / \mu m}$) for two wavelength beam propagation simulations. (a) For $\mu=1.0$ and $\eta=0.95$, $ \psi_1 $ is shown by \diamond and $ \psi_2 $ by Δ ; and for $\mu=1.0$ and $\eta=0.95$, $ \psi_1 $ is \square , and $ \psi_2 $ is \circ . (b) For $\mu=1.0$ and $\eta=1.0$ coupled soliton formation occurs.	105
Figure 7.6 Propagation simulations based on the coupled quintic Ginzburg-Landau equations. (Left) Only one beam input. (Right) Two beams input.	107

CHAPTER ONE: INTRODUCTION

“The beginning is the most important part of the work.”
Plato

1.1 Introduction

The diffraction of light originates from a fundamental level, the uncertainty principle. From the fundamentals of quantum mechanics it is known that a photon, just like for example an electron, has a wave-particle duality. Since the uncertainty principle applies, localization in one dimension implies an uncertainty (spread) in the momentum in that dimension so that the wave function of the particle (in this case a photon) delocalizes on propagation.

Consider the well-known case in physics of an electron beam that is passing through a very narrow slit (w), and when projected onto a photographic plate which is further away from the slit, an Airy pattern could be seen on the plate (Figure 1.1). In view of the particle nature of the electrons, this is a very interesting result, since electrons should acquire a momentum parallel to the slit to form this pattern. The reason for this is the localization of the electron to the slit (w). This localization causes an uncertainty in the momentum in the same direction; $w \cdot \Delta p = h$. Using the momentum parallel to the slit and the momentum associated with the deBroglie wavelength, the range of incidence angles of the electrons is estimated on the photographic plate $\Delta p / p \approx (h/w)/(h/\lambda) \approx \theta$, which is in very good agreement with the first zero of the airy

diffraction pattern [1.1]. Therefore diffraction is the result of the wave nature of a particle which applies equally well to photons as it does to electrons.

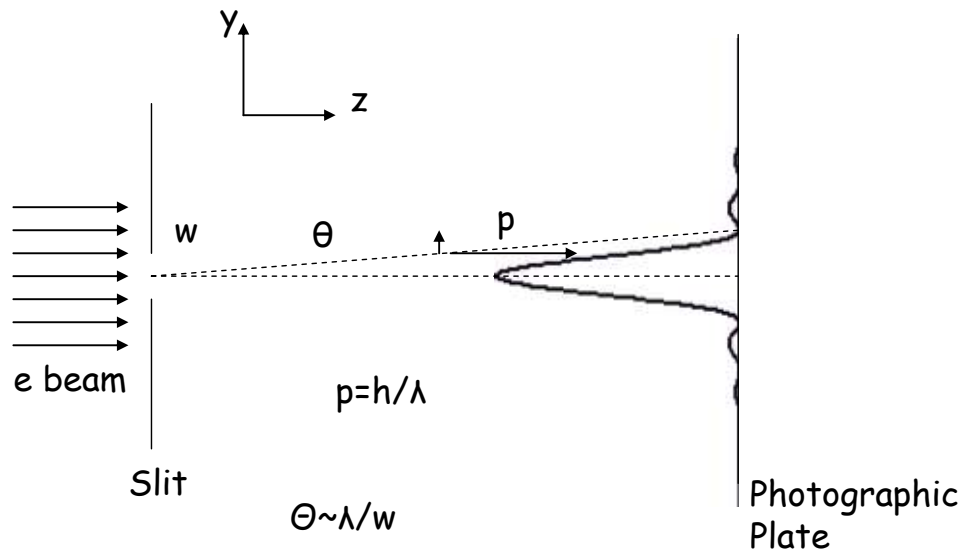


Figure 1.1 Diffraction of electron beams is related to the uncertainty principle

When photons in nonlinear media are considered, diffraction could be negated. A *spatial soliton* is a shape invariant self guided beam of light or a *self-induced waveguide*. In Figure. 1.2 the observation of the formation of a spatial soliton in a liquid crystal is shown. Liquid crystal cells show very good examples of soliton formation, since it is possible to take picture of the beam diffraction from the top of a liquid crystal cell [1.2]. Furthermore these pictures also prove that solitons are actually very stable entities, since the possibility to take a picture from top of a propagating soliton requires lots of scattering and hence propagation loss in the system. In the minds of many scientists, solitons are not only photons propagating bound together, but are also

particles. They could interact with other solitons, exchange energies and change system properties, refractive index, gain, etc.

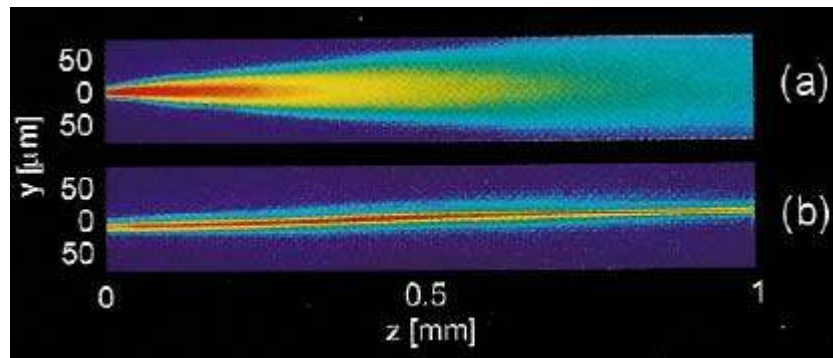


Figure 1.2 Liquid Crystal Solitons (a) the diffraction of a helium neon laser beam imaged from the top of the cell (b) spatial soliton when the nonlinearity of the liquid crystal is turned on by application of an electric field [1.2]

Solitons have been an attractive research area for about four decades. In 1964 Chiao, Garmire and Towns first showed that the beam spreading could be prevented by nonlinear interactions [1.3]. They used an intensity dependent refractive index change that formed a self induced waveguide for the propagating light. The balance of the self-focusing effect and diffraction formed a bright soliton. Subsequently the inverse scattering method by Zakharov and Shabat showed that this system is stable in one dimension [1.4]. For a Kerr nonlinearity their model has an infinite number of conserved quantities, therefore this 1-D model was fully integrable. Thus when two solitons collide with each other, in theory they survive and there is only a phase change as a result of the interaction. The first spatial soliton experiment in optics was done by Bjorkholm and Ashkin in the early 1970s [1.5]. The soliton field has developed in

the last ten years with a steady evolution of interest towards solitary waves in physical systems that are not described by the integrable partial differential equations (e.g. nonlinear Schroedinger equation). Many different solitons in systems in addition to the well-known Kerr media for SiO₂ fibers, have been found. The physical mechanisms supporting solitons have been enriched by many new ideas. Photorefractive solitons [1.6], quadratic solitons[1.7,1.8], Bragg solitons[1.9,1.10], discrete solitons[1.11,1.12], and cavity solitons [1.13-1.15] are the main current research areas.

Another classification of solitons could be made by considering system behavior. Integrable systems have solitons that can form one (or few) parameter families. Moreover they can be used as “modes” of the system to solve initial value problems, with a nonlinear superposition of modes approach [1.4]. In general systems in nature are Hamiltonian, and integrable systems can be considered as a simplification of these systems [1.16]. Solitons in Hamiltonian systems still form one (or few) parameter families like integrable systems, but they can collide inelastically and interact with radiative waves. When the medium becomes “*active*” (dissipative), the conditions for soliton formation are narrowed. In addition to the diffraction (or dispersion) balance by nonlinearity in Hamiltonian systems, dissipative systems require gain and loss balance. Therefore they usually do not form soliton families but are entirely determined by the parameters of the configuration (zero parameter solution). The shape, amplitude and width of solitons are all fixed, and depend on the parameters of the system. Dissipative solitons have become very attractive lately; giving new kinds of solitons and soliton properties, for example as found in cavity solitons [1.17], solitons in fiber rings [1.18, 1.19], and semiconductor resonator solitons[1.20, 1.21]. Most of these systems could be simplified to the complex Ginzburg-Landau

equations (CGLE), and CGLE soliton solutions have been found by Akhmediev and coworkers [1.16]. According to the best of our knowledge there has not been any work on semiconductor dissipative spatial solitons, although there were some preliminary experiments in standard semiconductor optical amplifiers (SOAs) [1.22, 1.23] which were subsequently proven to be unstable systems for soliton generation [1.24]. Therefore up to now all experimentally verified propagating solitons were in Hamiltonian systems, where at least energy is conserved and thus can be regarded as conservative solitons.

1.2 Scope of Research

The optical device market is based on semiconductor devices. Semiconductors are one of the most efficient ways of generating photons, with a very high wall plug efficiency. The main reason for having available high quality semiconductor optical amplifier (SOA) devices for soliton science is the development at the same time of an electronics market using semiconductor devices. As is well known, the semiconductor transistor is one of the greatest inventions of the last century. Therefore the optical market is shaped around semiconductor technology. For the last 2 decades, the fabrication of laser diodes, semiconductor waveguides, amplifiers and the driver electronics have been researched extensively to a high level of perfection. Today it is possible to buy commercial semiconductor devices emitting photons from UV to the far-infrared region of the spectrum. Their applications are not only limited to the telecommunications market, but also include medical, lightning, machining, sensing and military markets.

The main aim in this research is to connect spatial soliton applications to the optoelectronics market. Although temporal solitons in fibers have caught the attention of telecommunication researchers for some time, spatial solitons actually have never been able to get out of the labs of the scientists. There are obvious reasons behind this. First of all in most of the nonlinear media (quadratic and Kerr), the generation of solitons requires very high powers $>100\text{W}$ s. It is not possible to put that much power into a device in the continuous (cw) mode. Instead pulsed lasers $<100\text{ps}$ are used, because of the considerations of wall plug supply, and heat generation along the system plus the sample. Therefore these solitons require a delicate balance between the power, pulses and nonlinear media. On the other hand in some nonlinear media (liquid crystals and photorefractives), the nonlinear power threshold is very low, $<\text{mW}$ s, however the response time of these media are very slow (seconds). The power and response time limitations lead us to look for another nonlinear medium for soliton generation. Semiconductor resonant nonlinearities are known to be fast ($<\text{ns}$) and at the same time require reasonably low powers ($<100\text{mW}$ s). Besides the advantages of a nonlinear device which is already in the market, power and response time of semiconductors is also very attractive for soliton generation.

In this Phd Dissertation a new device is proposed and tested to generate spatial solitons using semiconductor resonant nonlinearities, and numerical simulations will be justified with experimental measurements. This Dissertation is organized as follows

Chapter 2 describes the basics of semiconductor physics and the semiconductor optical amplifier modeling equations that are used in the simulations. The equations are driven from the wave equation by using a nonlinear gain and index change coupled to the carrier generation and

loss rates. The stability of the solitons in the SOA has been analyzed using these simulations. In addition to these, the bifurcation behavior of the dissipative spatial solitons is explained.

In Chapter 3 the first observation of dissipative spatial solitons in periodically patterned semiconductor optical amplifiers (PPSOA) is described. The fabrication steps required for these devices in the clean room at CREOL are given. The properties of these solitons are verified with the experimental findings.

Solitons are not only interesting through their existence and formation, but also they could lead to all-optical applications with their interactions. In Chapter 4, the dissipative soliton interactions are investigated. Two coherent input beams are coupled to the device while controlling the relative phase difference between them. Interactions also led to the observation of non-local effects in the dissipative semiconductor amplifier solitons.

There are two completely numerical chapters in this thesis on modulation instability and discrete dissipative solitons. Modulation Instability is a process where a broad beam might form into filaments during propagation. The analytical analysis in Chapter 5 gives insight into the spatial frequency dependence of these filaments, and also how the soliton profiles could be affected by system parameters.

Chapter 6 is dedicated to the discrete dissipative solitons. Discrete systems are very attractive in order to change the propagation properties of light. When combined with the dissipative effects, the soliton properties could change radically. The discrete dissipative system is no longer zero parameter and could support multi-hump solitons. Furthermore the discrete solitons could propagate in a phase-locked manner.

The solitons do not always have to be coherent. It has been shown previously that even a white light source could generate solitons [1.25]. In the semiconductor system, incoherently coupled solitons seem to be unstable, as found in Chapter 7. However the interactions of incoherent solitons could lead to an exchange of energy which might be useful for soliton applications.

The principal contributions of this thesis are summarized in Chapter 8.

CHAPTER TWO: SOA THEORY

“It is the theory that decides what can be observed”
Albert Einstein

2.1 Introduction

Semiconductors are now used in various fields including microprocessors, memories, fiber communication systems, optical data storage, remote sensing, etc. In the optical domain the semiconductor lasers had the highest impact with their successful operation in CD players, laser printers, solid state laser pumping, and now even with high power diodes in the machining industry.

In the last thirty years a detailed understanding of semiconductor processes has been developed with the help of brilliant scientists. In this chapter the aim is to give an introduction into the optical processes in semiconductors, and semiconductor optical amplifiers. A detailed explanation of the semiconductor optical processes could be found in various resources [2.1-2.4]

2.2 Semiconductor Physics

A semiconductor is a crystalline or amorphous solid whose electrical conductivity lies between that of metals and insulators, and can be changed significantly by altering the impurity

concentration, light illumination or temperature. The energy bands in a crystal are found by the solution of Schrodinger equation for the electron's energy in a periodic potential created by the collection of atoms in the lattice. The bands are formed through the splitting of the energy levels. Valence bands are formed by a collection of electrons that are not attached to individual atoms, but form a system by themselves. The energy separation between the valence and conduction band, gives rise to the bandgap of the semiconductor. The bandgap width and energy determines most of the electrical and optical properties of the material.

In this Dissertation, the focus is mainly on GaAs based devices. GaAs is a direct bandgap semiconductor, where the bottom of the conduction band and the top of the valence band occur at the same effective momentum, or k equal to zero and therefore materials like GaAs are efficient photon emitters. In the case of indirect bandgap semiconductors, a transition from the valence to the conduction band requires a substantial change in momentum. Elemental semiconductors like Si are used mainly for microelectronics. However their bandgap is indirect. Therefore photon emission and the absorption coefficient of these materials are low. Compound semiconductors (like GaAs or other materials of group III-V, II-VI, IV-VI or IV-IV compounds) offer the desired properties for optoelectronics, and they are fabricated without much difficulty by mature technologies.

Doping of the semiconductors can change the number of carriers in a band. As an example, dopants with excess electrons will create dominance of mobile electrons in a semiconductor and then the material is called a n-type semiconductor. P-type semiconductors occur when the dopants that are used have a deficiency of valence electrons. P type doping will create holes in the valence band, which occur because of the escape of electrons. Holes can be

thought as positive charges in a band. The density of electrons and holes in a band also depends on the temperature. As the temperature is increased electrons can escape to the conduction band, leaving holes behind. The probability of the occupancy of energy level E depends on the Fermi function $f(E) = \frac{1}{\exp[(E - E_f)/k_B T] + 1}$, where E_f is a constant known as the Fermi energy or level, k_B is the Boltzmann's constant, and T is the temperature. For an undoped semiconductor the Fermi level lies between the conduction and valence band, and at 0° K the probability of an electron to be in the valence band is $f(E_{valence})=1$ (%100), and a hole in the conduction band is $1 - f(E_{conduction})=1$. For a p type semiconductor the Fermi level is near to the conduction valence band which generates the probability of holes in the valence band being larger than electrons in the conduction band.

Junctions are the core of semiconductor based devices. A p-n junction occurs when a p type semiconductor is brought in contact to an n type semiconductor. Through the diffusion of majority carriers (holes from p type, electrons from n type material), a narrow depletion region is formed at the contact of the materials. *Heterojunctions* are formed when a semiconductor layer is sandwiched between the p-type and n-type semiconductors. The heterojunction is one of the greatest inventions of the last century and was the topic of the Nobel Prize in physics for the year 2000 as a result of their applications in laser diodes, high speed modulators, etc [2.5, 2.6]. Heterojunctions could be used to select the regions where the light is emitted. Furthermore heterojunctions allow choosing different regions of the device through photon absorption. If the bandgap energy is bigger than the photon energy, the material will be transparent. Moreover it is

possible to generate different refractive index regions in a device via heterojunctions and this allows optical waveguiding (Figure 2.1).

If the heterostructures are grown in thin layers, quantum wells can be formed. The most common way to grow quantum wells (QW) is by molecular beam epitaxy (MBE) where molecular beams are directed onto a substrate under high vacuum conditions. When the layer thickness is smaller than the deBroglie wavelength of thermalized electrons (about 50nm for GaAs), the properties of bulk semiconductor do not apply. Quantum wells have discrete bands which are found by the solution of the time-independent Schroedinger equation. Therefore the density of electrons and holes in the bands takes on a “staircase” distribution. The advantages of using a quantum well are the ability to engineer the semiconductor bandgap (changing the absorption, and emission spectra), and also to have a very narrow region where electrons and holes interact while increasing the efficiency of the recombination mechanism, and the overall device efficiency.

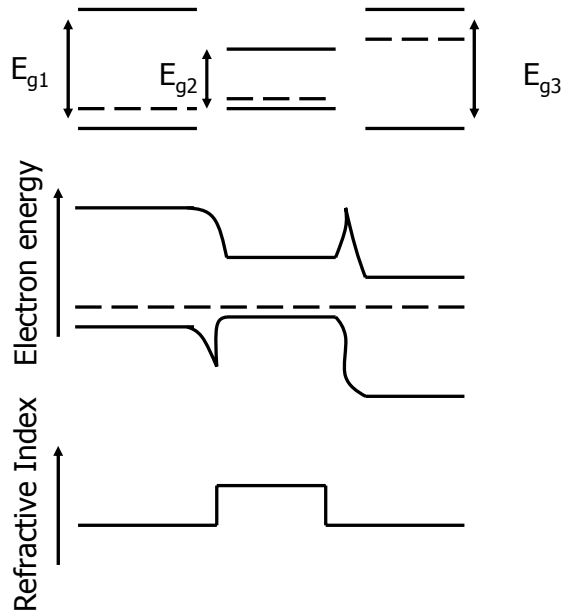


Figure 2.1 Semiconductor heterojunction, p-p-n structure. The Fermi levels of the semiconductor align and form the barriers. When this device is forward biased, holes from the first semiconductor and electrons from the third semiconductor will enter the second semiconductor, and their recombination will occur in the middle region. In addition to these effects, generally the semiconductors with low bandgap energies, have higher refractive indices than the large bandgap energy semiconductors. This allows the optical confinement of light in the middle of the heterostructure.

Photons interact (absorption and emission) with semiconductors through various ways. *Band to band transitions* occur when a photon is absorbed in the semiconductor through the movement of an electron from the valence band to the conduction band. When the hole and electron recombination occurs, there can be an emission of a photon. This kind of transition could be assisted by phonons (thermally excited vibrations in a material). *Impurity to band transitions* occur when an electron is transferred from the valence band to a donor band. They require lower energy photons than band to band transitions. *Free carrier interactions* happen

when a photon transfers its energy to an electron in the conduction band, and the electron moves to a higher energy level in that band. These are usually induced by low energy photons. The electron populations produced usually relax by interactions with thermal vibrations. *Exciton interactions* are a result of the absorption of a photon through a pair of electrons and holes which are already interacting with each other through Coulomb effects. This interaction is very strong, but it occurs only over a sharp and narrow peak in the absorption spectrum. (See Figure 2.2 for a typical absorption diagram which does not include semiconductor-exciton interactions.)

Semiconductor optical amplifiers are basically p-n junction diodes (Figure 2.3). When the current is applied to the diode with a forward bias voltage, carriers are injected into the heterojunction region and population inversion is achieved, which leads to stimulated emission.

The change of absorption in a semiconductor optical amplifier by the injection of current or by the absorption of photons will also cause a refractive index change at the same time. According to Kramers-Kronig relationship, this refractive index change (Δn) is proportional to;

$$\Delta n(\xi) = \frac{ch}{2\pi^2} \oint_{0 \rightarrow \infty} \frac{\Delta \alpha(\xi')}{(\xi')^2 - (\xi)^2} d\xi' \quad (2.1)$$

where ξ and ξ' are the photon energies corresponding to refractive index and absorption change spectrums, c is the speed of light, h is Planck's constant, $\Delta \alpha$ is the change in absorption coefficient. In Figure 2.2 when the absorption of a semiconductor increases (via a decrease in injection current, or a decrease in the amount of photons absorbed), there will be an increase in the refractive index for most of the region around the peak absorption change in the semiconductor and for energies below the peak. However, on the high energy side of the spectrum the refractive index decreases.

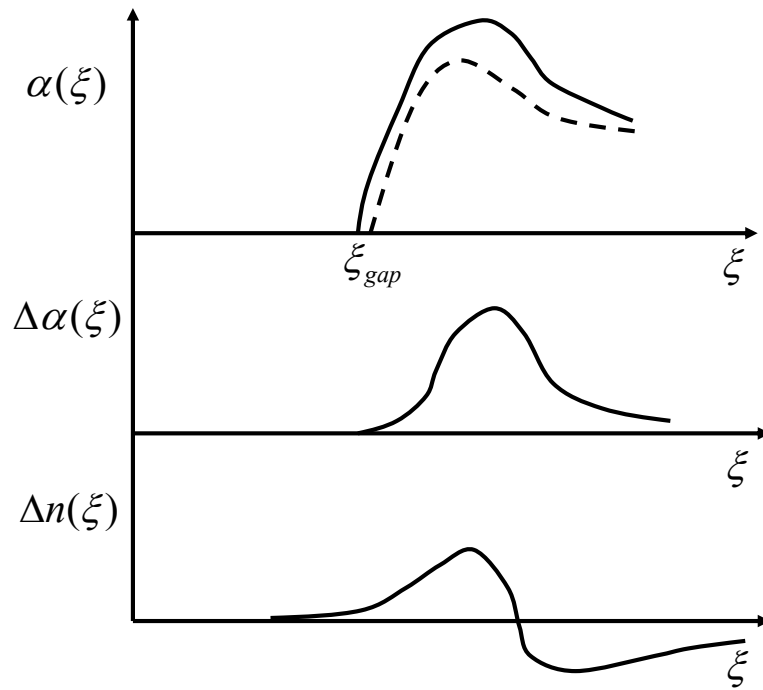


Figure 2.2 The refractive index (Δn) and absorption coefficient ($\Delta\alpha$) change as the absorption spectrum changes from the dashed line to solid line.

The analysis of beam propagation in semiconductor optical amplifiers has to include the effects of the Kramers-Kronig relationship since the refractive index change in a semiconductor medium could easily be on the order of 0.01.

2.3 SOA modeling equations

Semiconductor media are sometimes considered to exhibit features common to an ensemble of two-level atoms. However, in a semiconductor the different transition energies are defined by the electronic band structure and the resulting non-discrete states have different electron occupations. Therefore a two level model of the system does not give exact solutions for semiconductor systems. Nevertheless the rate equation model, based on the two level system, has been successfully employed in the semiconductor field for many years, because of its simplicity and intuitive appeal [2.7]. More exact methods using Bloch equations give accurate models when fluctuations, modulation or optical pulses are evolving on time scales less than picoseconds [2.8, 2.9]. Since the solitons for the continuous wave regime is considered, the two level model will be used here.

The two level model and its derivation from the 3D wave equation is given next;

The optical field $\mathbf{E}(\mathbf{r},t)$ satisfies the wave equation,

$$\nabla^2 \mathbf{E} - \frac{\varepsilon(r)}{c^2} \frac{\partial^2 \mathbf{E}}{\partial t^2} = 0 \quad (2.2)$$

and can be written as functions depending on y , z and x (for axes see Figure. 2.3).

$$\mathbf{E}(\mathbf{r},t) = \frac{1}{2} \mathbf{x} \phi(y) \psi(x,z) e^{i(kz - \omega t)} + c.c. \quad (2.3)$$

It is assumed that field distribution along y does not change with propagation, i.e. a waveguide is assumed. Using Equation (2,3) and the SVEA leads to,

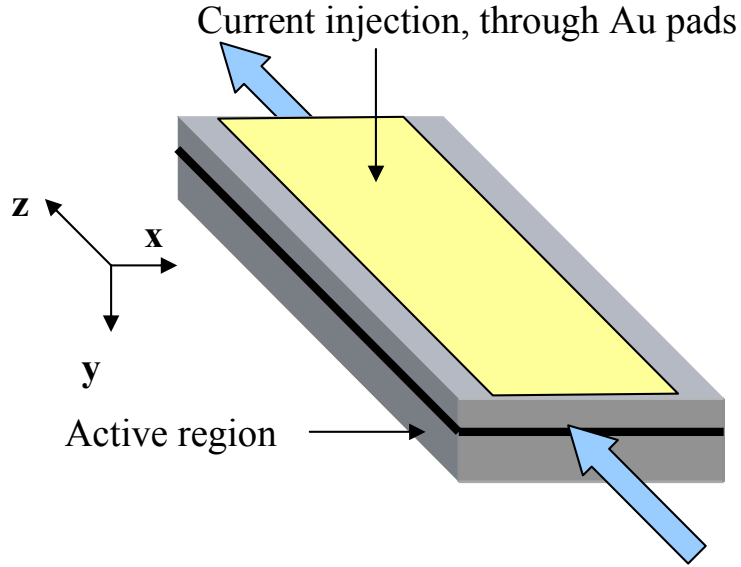


Figure 2.3, Semiconductor Optical Amplifier

$$\psi \frac{\partial^2 \phi}{\partial y^2} + \phi \frac{\partial^2 \psi}{\partial x^2} + \phi 2ik \frac{\partial \psi}{\partial z} - \phi k^2 \psi + \frac{\varepsilon(r)}{c^2} \omega^2 \phi \psi = 0 \quad (2.4)$$

Multiplying Equation (2.4) with $1/(\psi\phi)$, and separating it into two equations with a dependence of one on x,z and the other only y , the following equations are obtained.

$$\frac{\partial^2}{\partial y^2} \phi + (\varepsilon(r)k_0^2 - \beta^2)\phi = 0 \quad (2.5a)$$

$$\frac{\partial^2 \psi}{\partial x^2} + 2ik \frac{\partial \psi}{\partial z} + (-k^2 + \beta^2)\psi = 0 \quad (2.5b)$$

For a symmetric waveguide ε is defined as

$$\varepsilon(r) = \begin{cases} n_a^2 + \Delta\varepsilon_a & |y| \leq d/2 \\ n_b^2 + \Delta\varepsilon_b & o/w \end{cases} \quad (2.6)$$

where the subscript ‘‘a’’ identifies the active layer and ‘‘b’’ the surrounding layers, n_a and n_b are the corresponding refractive indices of those layers. The effective index for the waveguide mode n_{eff} ($k = k_0 n_{eff}$) is found by multiplying Equation 2.5a with ϕ^* , and then integrating the equation on the y axis gives Equation 2.7. A new parameter β is defined, using the confinement factor;

$$\Gamma = \frac{\int_{-d/2}^{d/2} |\phi|^2 dy}{\int |\phi|^2 dy} \text{ as}$$

$$-k_o^{-2} \frac{\int \left| \frac{\partial \phi}{\partial y} \right|^2 dy}{\int |\phi|^2 dy} + n_a^2 \Gamma + n_b^2 (1 - \Gamma) = n_{eff}^2 \quad (2.7)$$

$$\beta^2 = k^2 + \Delta\varepsilon_a k_0^2 \Gamma + \Delta\varepsilon_b k_0^2 (1 - \Gamma) \quad (2.8)$$

Then the field equation for ψ is reduced to

$$\frac{\partial^2 \psi}{\partial x^2} + 2ik \frac{\partial \psi}{\partial z} + (\Delta\varepsilon_a k_0^2 \Gamma + \Delta\varepsilon_b k_0^2 (1 - \Gamma)) \psi = 0 \quad (2.9)$$

where it is assumed for the active layer the permeability change is

$$\Delta\varepsilon_a = -an_a hN / k_0 - i(n_a / k_0)[(aN - aN_{tr})] \quad (2.10)$$

Here a linear gain dependence is assumed with transparency carrier density N_{tr} , $g(N) = a(N - N_{tr})$, where a is the gain coefficient, and $\frac{\partial n / \partial N}{\partial g / \partial N} = h$ is called the *linewidth enhancement factor*. In addition to these, there is an additional contribution to the absorption coefficient from the surrounding passive guiding layers which is denoted as,

$$\Delta \varepsilon_b = i(n_b / k_0) \alpha_p / \Gamma \quad (2.11)$$

where α_p is the absorption coefficient of these layers.

The nonlinear gain and refractive index is also a function of wavelength. It has been evaluated by various researchers [2.10] using amplified spontaneous emission measurements of Fabry-Perot peaks, and calculating the refractive index change from Kramers-Kronig relationships. Figure 2.4(a) shows the actual increase in the gain of a semiconductor laser medium with carrier density. As the pumping level is increased the peak gain shifts to lower wavelengths because of the band-filling effect. The linewidth enhancement factor does not become zero at the gain peak since the gain spectrum is not symmetric around the peak. Since the linewidth enhancement factor increases as the wavelength is increased, therefore higher index changes are achievable at longer wavelengths.

Various different fits (linear, logarithmic) have been used to find the dependence of the gain and linewidth enhancement factor on carrier rate. Principally depending on the material type, the fitting models change. Here the model with a linear gain dependence and a constant h factor will be used. This assumption is very reasonable as long as bulk materials are used in the vicinity of their gain peak.

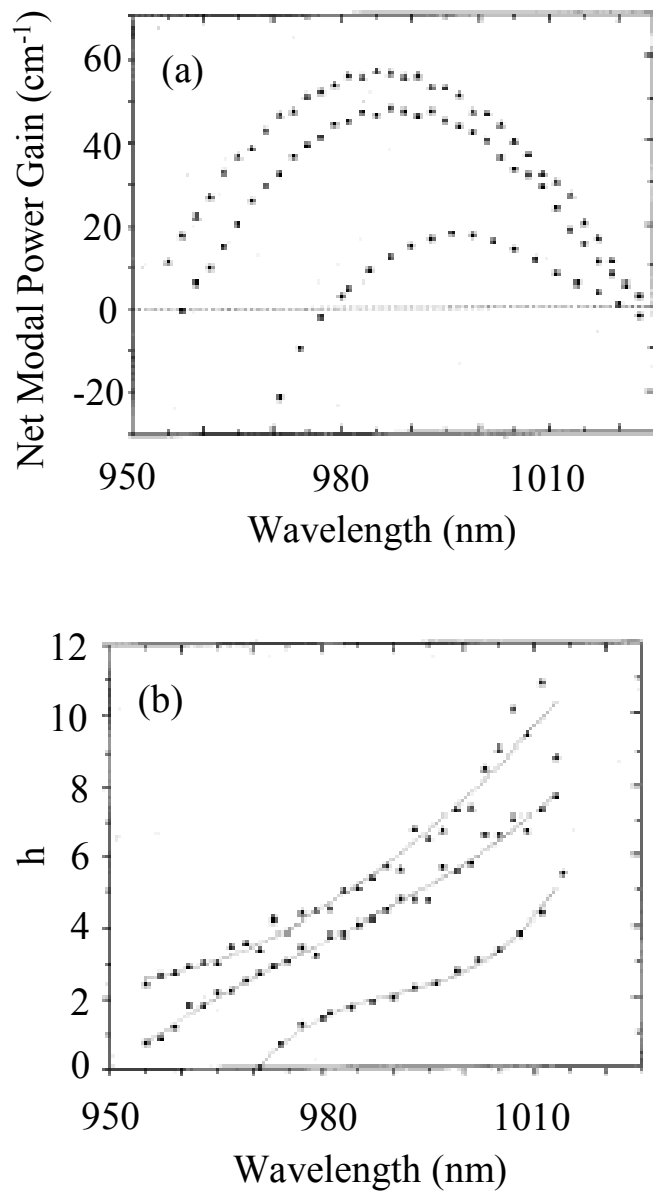


Figure 2.4 The change in net modal power gain (a) and linewidth enhancement factor (b) of a InGaAs SQW semiconductor laser diode. The curve values increase with the sheet carrier densities given as 1.7×10^{12} , 3.5×10^{12} and $4.6 \times 10^{12} \text{ cm}^{-2}$ [from Ref. 2.11]

The carrier rate equation gives the density of carriers N (cm^{-3}), coupled to the electric field vector $\mathbf{E}(\mathbf{r},t)$;

$$D\nabla^2 N = \frac{J(r)}{qd} + \frac{N}{\tau_{nr}} + BN^2 + CN^3 + \frac{g(N)}{\hbar\omega} |\mathbf{E}(\mathbf{r})|^2 \quad (2.12)$$

D is the diffusion coefficient, J the current density, τ_{nr} the nonradiative recombination time, B the spontaneous recombination coefficient, and C the Auger recombination coefficient. Since solitons are waves which are not changing along the propagation distance, the carrier diffusion along the propagation direction can be neglected, then the field and carrier rate equations are reduced to;

$$\psi_z = \frac{i}{2k} \psi_{xx} + \frac{ia\Gamma N_0}{2} (-\hbar N' - i(N' - 1) + i \frac{(1-\Gamma)\alpha_p}{aN_0\Gamma}) \psi \quad (2.13a)$$

$$DN_{xx} = -\frac{J}{qd} + \frac{N}{\tau_{nr}} + BN^2 + CN^3 + a \frac{(N - N_{tr})}{\hbar\omega} \Gamma |\psi|^2 \quad (2.13b)$$

Equation normalization facilitates the subsequent analysis of the equations. The normalized equations derived from Equation 2.13 are

$$\psi'_z = \frac{i}{2} \psi'_{x'x'} + (-i\hbar N' + (N' - 1) - \alpha) \psi' \quad (2.14a)$$

$$D' N'_{x'x'} = -\pi + N' + B' N'^2 + C' N'^3 + |\psi'|^2 \quad (2.14b)$$

where $N' = N / N_{tr}$, $D' = \tau k L D$, $B' = \tau N_{tr} B$, $C' = \tau N_{tr}^2 C$, $L = a \Gamma N_{tr} / 2$, $\alpha = (1 - \Gamma) \alpha_p / (2L)$ and ψ is normalized by ψ_s ; $|\psi_s|^2 = \hbar \omega / (a \Gamma \tau)$, $\pi = J \tau / q d N_{tr}$, $x' = x \sqrt{k L}$, $z' = z L$.¹

2.4 Soliton Solutions and Their Stability

Dissipative solitons (or autosolitons) are generated by a balance between linear and nonlinear effects, including loss and/or gain. Therefore they usually do not form soliton families but are entirely determined by the parameters of the configuration (zero parameter solution). Their stability is determined by the details of the operating conditions [2.12-2.14]. Their regions of stability can be identified from bifurcation diagrams that describe the solutions of the system-defining equations by changing the relevant control parameter, e.g., the system net gain. Bifurcation diagrams can be plotted both for stationary homogeneous (plane wave - PW) as well as for soliton solutions. Stable solitons may potentially exist around critical points of subcritical PW bifurcations [2.12], because the background (potential low power tails of a soliton) experiences loss thus suppressing its destabilization.

¹ The normalized coefficients are used in the rest of the document without the primed notation, as long as o/w is mentioned

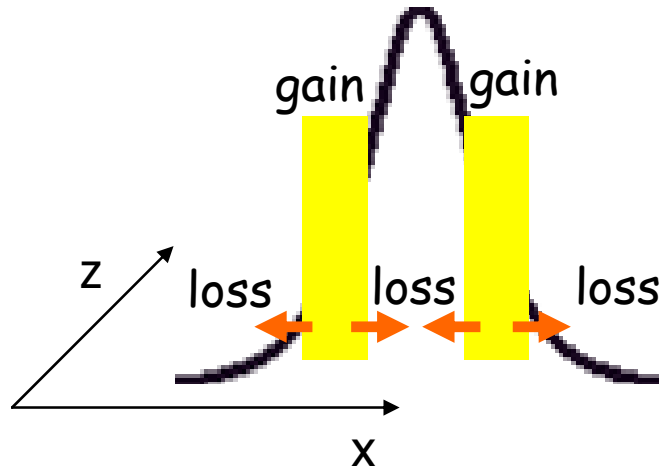


Figure 2.5 Dissipative soliton profile showing that a dissipative soliton has regions of gain and loss over its field profile which balance to produce a stationary field profile

Figure 2.5 illustrates the energy exchange on the dissipative soliton profile. The tails and the peak of the beam experience loss, and the regions between the peak and the tails see gain. Diffraction and nonlinearity will cause interactions between the gain and loss regions. The red lines in the figure show where the energy is trying to escape, however because of the loss in these regions, solitons can propagate in a stable fashion. The loss and gain behaviour of a dissipative soliton system makes it a soliton attractor- i.e. the soliton can spontaneously form by itself, even though the input beam profile to the dissipative system is not the same as the soliton's.

In a first step it is shown analytically that an isolated uniform SOA (uniform current pumping, $\pi(z) = \pi_0$) cannot support stable self-trapped beams. $B = C = 0$ can be assumed because these terms do not change the type of bifurcation and stability for a purely amplifying system. For small diffusion near the bifurcation point (for definition, see below) a generalized complex

Ginzburg-Landau equation can be derived. The equations derived in the preceding section are simplified and can be combined to give;

$$\frac{\partial \psi}{\partial z} = i \left(\frac{1}{2} - i\beta \right) \frac{\partial^2 \psi}{\partial x^2} + \left\{ \frac{(\pi_0 - 1)}{1 + |\psi|^2} (-ih + 1) - ih \right\} \psi - \alpha \psi \quad (2.15)$$

Here β accounts for the transverse carrier diffusion. The canonical Ginzburg-Landau equation, frequently used to describe beam propagation in a SOA or a laser diode gain medium, is recovered by expanding the denominator. To obtain the PW bifurcation behavior of the system a one-dimensional plane wave is assumed, i.e., $\psi = \psi_0 \exp(ikz)$ where k is the propagation constant. The small signal net gain of the system, which will serve as a control parameter, is $\delta G = \pi_0 - 1 - \alpha$.

Equation 2.15 has two solutions for $|\psi_0|$, the trivial one $|\psi_0| = 0$ and $|\psi_0| = \sqrt{\delta G / \alpha}$ (Figure 2.6) for $\delta G > 0$, both requiring the dispersion relation $k = -h \left(\pi + |\psi_0|^2 \right) / \left(1 + |\psi_0|^2 \right) = -h(1 + \alpha)$. Linear stability analysis reveals that the trivial solution destabilizes for $\delta G > 0$ but leaves the nontrivial solution stable. Thus stationary PW solutions in a conventional SOA bifurcate super-critically $\left(\partial |\psi_0|^2 / \partial \delta G > 0 \right)$ at $\delta G = 0$ (bifurcation point).

The consequence for soliton or self-trapped beam formation is that a positive net gain is required but, in turn, that will destabilize the soliton tail (growth of amplified spontaneous emission – ASE, see Figure 2.8). Therefore for $\delta G < 0$ the fields are absorbed and for $\delta G > 0$ the solutions are unstable due to the growth of any noise. These types of SOA structures have been analyzed theoretically [2.15, 2.16] and experimentally [2.17] in the past.

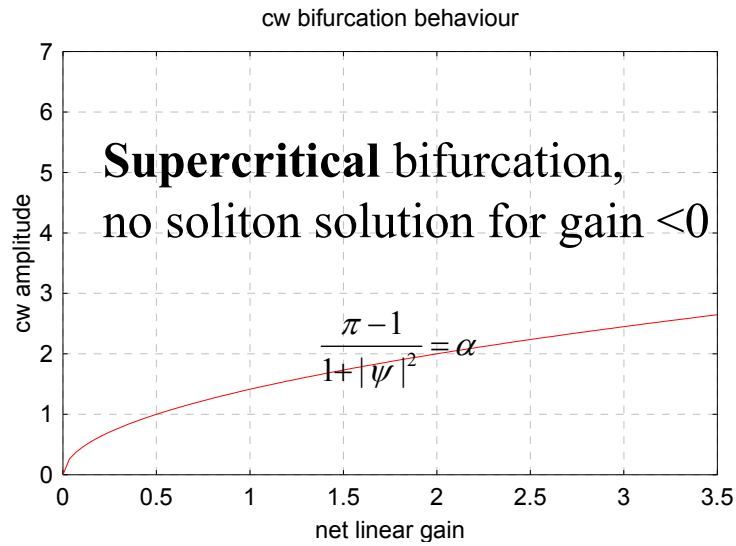


Figure 2.6 SOA bifurcation diagram

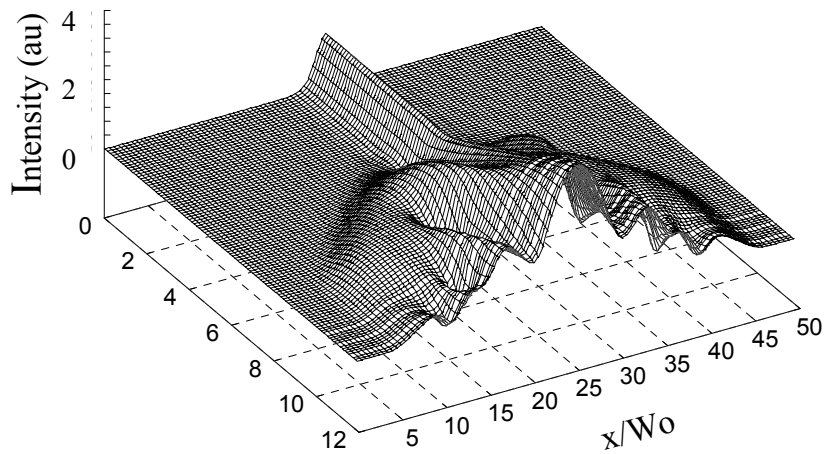


Figure 2.7 Propagation of an initially localized soliton-like solution in a uniformly pumped SOA; The solution is unstable and evolves into filament-like structures because of numerical noise in the simulation.

The key idea for creating stable solitons is to introduce a form of saturable absorption for noise reduction in the system.. (Note that the gain is always saturable in a SOA.) This can be achieved by introducing periodic losses into a SOA forming now a SOA/SA module (Figure 2.8).

In numerically solving the full system, of Equations 2.14 for stationary plane waves (PWs-no transverse field dependence) with periodic pumping ($\pi(z)=0$ for absorber regions and $\pi(z)=\pi_0$ for amplifier regions) again a trivial PW solution destabilizing at the bifurcation point $\delta G = 0$ (now $\delta G = 0.5\pi_0 - 1 - \alpha$) is obtained. Assumed here was that the pumping region has the same length as the un-pumped region. However now the nontrivial solution emanates subcritically ($\partial|\psi_0|^2/\partial\delta G < 0$) from $\delta G = 0$. Thus in a limited region ($\delta G_{\min} < \delta G < 0$) there are two stable PW solutions, the prerequisite for stable soliton formation (see Figure 2.9b).

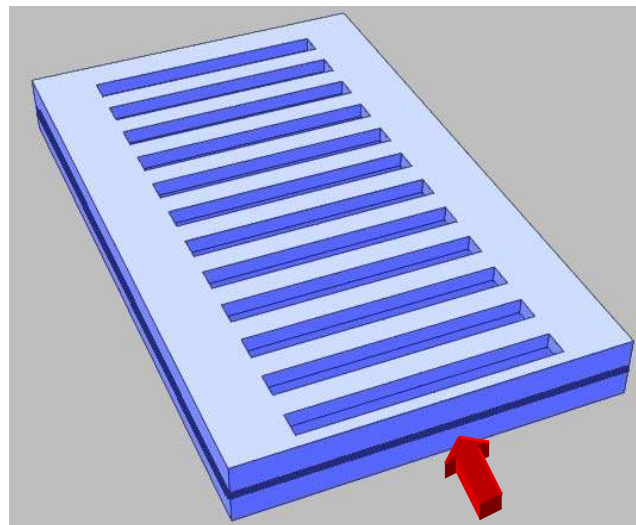


Figure 2.8 Model device, with periodic contact pads (Openings on the top layer of the device could be used for current injection)

The key for understanding this behavior is the fact that the pumped and the un-pumped regions saturate at different intensity levels resulting from the nonlinear dependence (spontaneous recombination $\propto N^2$ and Auger recombination $\propto N^3$) of the saturated carrier density on the field. Figure 2.9(a) shows the difference in the saturation curves for both the pumped and un-pumped regions of a GaAs SOA/SA module that lases at $0.82\mu\text{m}$. For the simulations a non-radiative recombination time of 5ns, a carrier diffusion constant of $33\text{cm}^2/\text{s}$, a gain parameter of $1.5 \times 10^{16} \text{ cm}^2$, a Henry factor (h) of 3, a spontaneous recombination coefficient of $1.4 \times 10^{-10} \text{ cm}^3/\text{s}$, an Auger coefficient of $1.0 \times 10^{-30} \text{ cm}^6/\text{s}$ and an internal loss (α) of 2.5cm^{-1} were used.

The intensity dependent net gain (solid line in Figure 2.9a) is the sum of gain (along the pumped region), loss (along the unpumped region) and of α (again both regions are assumed to be of equal length). As the pumping current is increased, the net gain vs. intensity curve has two zero gain crossings, which correspond to two points on the subcritical curve of Figure 2.9b. The crossing at lower intensity corresponds to an unstable solution since small perturbations in intensity will cause it to evolve towards either stable point, i.e., the trivial solution or the crossing point at high intensity. If the intensity decreases, the loss increases until it drives the system to zero field. If the intensity increases, this results in a net gain which drives the system towards the second zero. The latter one is stable because any small perturbation will eventually relax back to the zero net gain point. Specifically, if the intensity drops there is net gain which moves the system back to the zero point. Similarly an increase in the intensity results in net loss which again decreases the intensity back to the second zero. Therefore this second zero indicates that stable soliton solutions can exist.

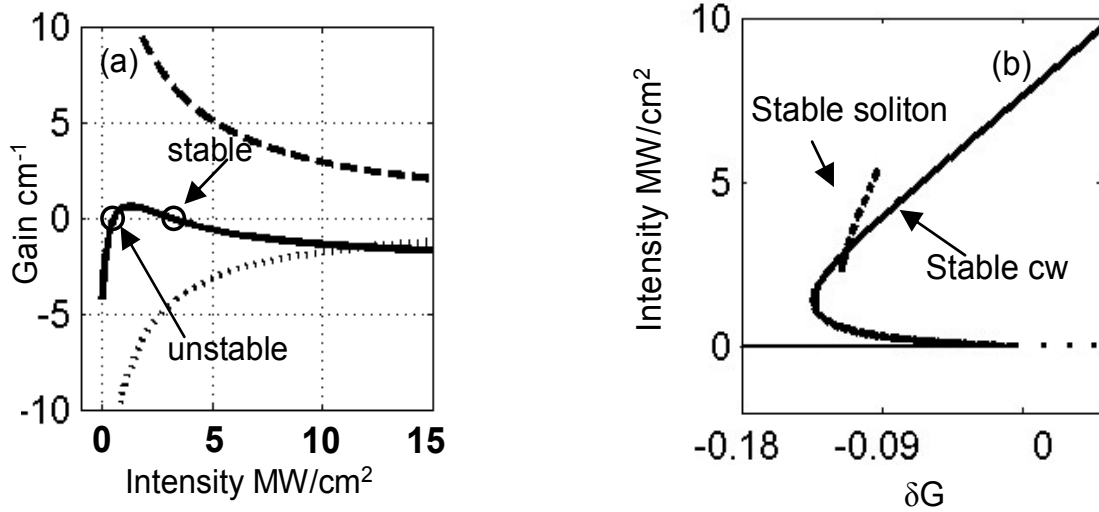


Figure 2.9 a) Gain and loss of the system vs. field intensity. The dotted curve shows the saturating loss (considered here as negative gain) in the non-pumped region, and the dashed curve is the saturated gain in the pumped region. The solid line represents the sum of these two contributions including the internal linear losses of the system, b) The PW and soliton bifurcation diagrams vs. δG . The thick solid line shows the PW solutions that subcritically bifurcate from the trivial solution. Between zero gain and the turning point the solution with negative slope is unstable. The dashed line indicates the peak intensity of the stable soliton which has a fine beam width along x axis. This branch terminates because of Hopf instabilities. The dotted line is the unstable trivial PW solution at positive small signal gain, and the thin solid line is the stable zero PW solutions. The fields shown here are averaged over the pumped and unpumped segments.

The whole suite of these solutions is displayed in Figure 2.9b, viz. peak intensity as a function of the small signal net gain which is controlled by the pump current. Three qualitatively different regions can be identified in that plot. For $\delta G < \delta G_{\min} \approx 0.134$ the SOA/SA module absorbs for any incident PW field. Increasing the pumping current results in $\delta G_{\min} < \delta G < 0$ and the system becomes bistable (stable upper and lower branches, unstable negatively sloped branch). If the pumping current is further increased and $\delta G > 0$ the beams will sit on an unstable

background and hence will be themselves unstable. This latter behavior is the same as for a conventional SOA bifurcation as discussed above.

The evolution with distance of the soliton solutions of the SOA/SA module (Equation 2.14) have been calculated by using a beam propagation (BPM) code (see for example Fig. 2.9b). The patterned amplifier was assumed to have $10\mu\text{m}$ contact layers with a $20\mu\text{m}$ period. A standard finite difference BPM algorithm is used [2.18]. The carrier density equation (Equation 2.14b) is calculated at each step of propagation using a Newton relaxation scheme explained in Chapter 3 (and also *Numerical Recipes* book [2.19]), and the effects of carrier density are added to the field (Equation 2.14a) using the half-step propagation technique [2.18].

It turned out that stable solitons exist near the upper branch of the subcritically bifurcating PW solution (see Figure 2.9.b, the soliton peak intensity curve). For $\delta G \rightarrow 0$ the soliton solution started to breathe indicating that it may undergo a Hopf bifurcation. Nevertheless, the numerics verify that in a certain domain of net small signal losses stable soliton propagation can be achieved.

As could be expected from the theory of dissipative solitons [2.20, 2.21] the stable SOA spatial solitons exhibit curved (chirped) phase fronts (see Figure 2.10 a) in contrast to the flat phases associated with conservative solitons. Although the phase of the soliton is highly chirped, BPM simulations have shown that these SOA spatial solitons evolve from a flat phase input (similar to the focal region of beam coupling) after a relatively short propagation distance of about 1-2 diffraction lengths [see Figure 2.10 b)]. The input power in this case was about 180 mW.

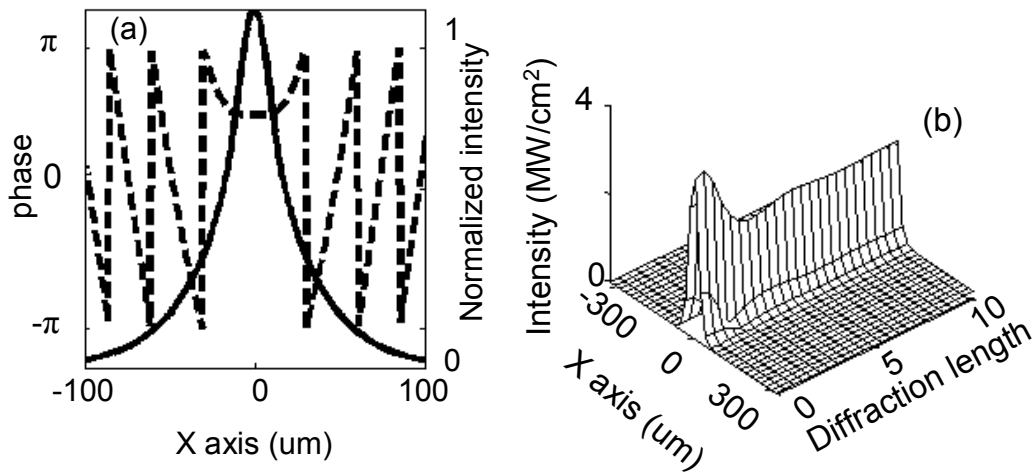


Figure 2.10 a) Soliton amplitude (solid line) and phase profile (dashed line). b) Evolution at $\delta G = -0.106$, of a 179.2 mW total power input beam with a constant phase, a sech^2 intensity distribution, and a $37.5\mu\text{m}$ beam waist (FWHM) into a $24.5\mu\text{m}$ beam waist (FWHM), 181.4 mW spatial soliton, using normalized parameters ($B=0.7$, $C=0.005$, $D=1.56$, $\alpha=0.067$).

2.5 Conclusions

In this chapter the stable dissipative propagating spatial solitons in SOAs were predicted theoretically in a modified amplifier device. It was shown that a conventional SOA has unstable solitons because of the supercritical bifurcation of its PW solutions. By including periodical lossy regions, it was found that PW solutions may bifurcate subcritically allowing for stable solitons to exist. These periodically pumped SOAs are very attractive for supporting stable spatial solitons at low powers.

CHAPTER THREE: DISSIPATIVE SOLITON EXPERIMENT

“No amount of experimentation can ever prove me right; a single experiment can prove me wrong.”
Albert Einstein

3.1 Introduction

The experimental verification of stable solitons was done on a single quantum well (SQW) sample. Thus the numerical values for soliton power, and current density where solitons can appear were recalculated in this chapter. The devices on SQW wafers were fabricated in the CREOL clean room, and tested using a continuous wave ti-sapphire laser. Finally the experimental results were compared with the numerical findings.

3.2 Solitons in QW semiconductors

In order to observe the theoretically predicted solitons, a QW sample, grown in the University of Jena was used. The sample consisted of a single QW InGaAs layer, surrounded by AlGaAs waveguiding layers, grown over an n-doped GaAs buffer.

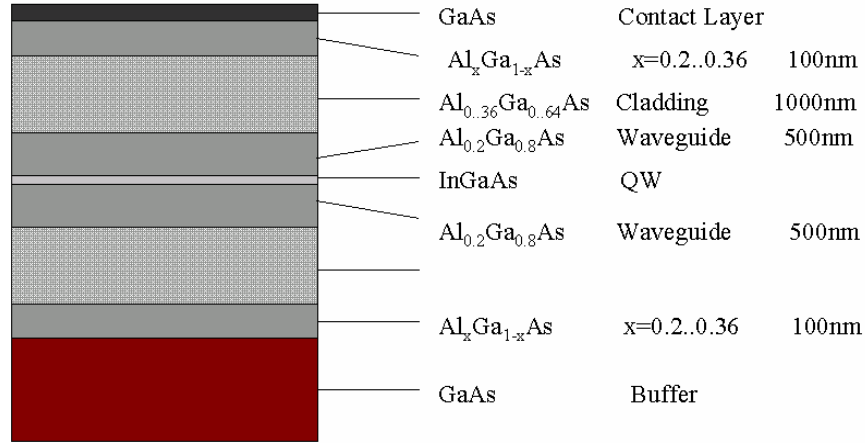


Figure 3.1 Wafer structure is a single quantum well p-n junction waveguide.

QWs have a higher material gain than bulk semiconductors, for a given current. The reason for this is the small volumes of carrier active regions in QWs. Therefore the gain model had to be modified from a linear assumption $g(N(\text{cm}^{-3})) = a(N - N_0)$ for the bulk case, to

$g(N(\text{cm}^{-3})) = a \ln\left(\frac{N + N_s}{N_{tr} + N_s}\right)$ for QWs, which models the saturation of the gain better than the

linear assumption [3.1]. Using this gain model, the normalized equations were;

$$\psi_z = \frac{i}{2}\psi_{xx} + \psi[f(N)(1 - ih) - \alpha] \quad (3.1a)$$

$$DN_{xx} + \pi(z) - BN^2 - CN^3 - f(N)|\psi|^2 = 0 \quad (3.1b)$$

Here it was assumed that $f(N) = \ln\left(\frac{NN_{tr} + N_s}{N_{tr} + N_s}\right)$, and N_s was the saturation carrier density. The

parameters in this gain equation were found by curve fitting to microscopic gain models. The

non-radiative recombination coefficient (A) was neglected since it is very small. Also the carrier density was normalized to N_{tr} , the transparency carrier density, and the field to the saturation field level $|\psi_s|^2 = \hbar\omega dN_{tr} / g$, where “d” is QW width and g the effective gain coefficient (aI).

The normalized axes z and x were, $z = z_{real}g$; $x = x_{real}\sqrt{2\pi n g / \lambda_o}$.

The SOA/SA device can be described by a space-averaged model which couples the carrier densities in the pumped ($N_1, \pi(z)=\pi_0$) and unpumped regions ($N_2, \pi(z)=0$) to the field equation. The gain function $f(N)$ was modified to $\bar{f}(N_1, N_2) = [f(N_1)w_1 + f(N_2)w_2]/(w_1 + w_2)$, where w_1 and w_2 are the widths of the pumped and unpumped regions respectively. These three coupled differential equations were solved for ψ (Equation 3.1a) and for N_1 and N_2 (Equation 3.1b) for equal widths of pumped and unpumped regions ($w_1=w_2$), by using parameters appropriate for an InGaAs SQW ($h = 3$, $\alpha = 0.024$, $N_{tr} = 2.5 \times 10^{18} \text{ cm}^{-3}$, $N_s = 0.6 \times 10^{18} \text{ cm}^{-3}$, $d=60\text{\AA}$, $g = 104 \text{ cm}^{-1}$, $D = 3.311$, $B = 3.0$ and $C = 0.219$) [3.1-3.3]. Here the stationary soliton solution $\psi(x)\exp(i\lambda z)$ which is independent of any initial condition was determined. $\psi(x)$ was the soliton shape and λ its propagation constant. A relaxation algorithm was used in order to find the soliton beam profiles. In the average model Equation 3.1 was rewritten as;

$$i\lambda\psi = \frac{i}{2}\psi_{xx} + \psi[\bar{f}(N_1, N_2)(1 - ih) - \alpha] \quad (3.2a)$$

$$DN_{1xx} + \pi_0 - BN_1^2 - CN_1^3 - f(N_1)|\psi|^2 = 0 \quad (3.2b)$$

$$DN_{2xx} - BN_2^2 - CN_2^3 - f(N_2)|\psi|^2 = 0 \quad (3.2c)$$

The partial differential equations in Equation 3.2 could be translated into finite difference schemes ($\frac{\partial^2 \psi}{\partial x^2} \cong \frac{1}{\Delta x^2}(\psi_{i-1} - 2\psi_i + \psi_{i+1})$). Then Equation 3.2 was written in the form of a function $F(\bar{\psi}, \bar{N}_1, \bar{N}_2) = 0$ where $\psi_i = \psi(\Delta x_i)$ with $\bar{\psi}$ being the soliton profile vector with elements ψ_i , and \bar{N}_1, \bar{N}_2 carrier profile vectors. If there is an initial guess profile for the field and the carrier densities, the function F could be written as an expansion around the initial guess vectors;

$$\begin{aligned}
F(\bar{\psi}, \bar{N}_1, \bar{N}_2) \cong & F(\bar{\psi}_{init}, \bar{N}_{1\ init}, \bar{N}_{2\ init}) + \left. \frac{\partial F}{\partial \psi} \right|_{\bar{\psi}_{init}} (\bar{\psi} - \bar{\psi}_{init}) + \\
& \left. \frac{\partial F}{\partial N_1} \right|_{\bar{N}_{1\ init}} (\bar{N}_1 - \bar{N}_{1\ init}) + \left. \frac{\partial F}{\partial N_2} \right|_{\bar{N}_{2\ init}} (\bar{N}_2 - \bar{N}_{2\ init}) \cong 0
\end{aligned} \tag{3.3}$$

Thus the difference between the soliton solutions and initial guess solutions could be calculated by just using the function values and derivatives at the initial guess vectors. The problem with this expansion technique was that for it to be exact, an infinite Taylor expansion was required. Since this was numerically impossible; another estimate for the soliton vectors could be calculated by using just the first order derivatives. This estimate will give another solution after it is applied to Equation 3.3, and so on. As long as the first initial guess was close enough to the soliton vectors, this technique will converge.

In the matrix form Equation 3.3 is;

$$\begin{bmatrix} \overline{\frac{\partial F_1}{\partial \psi_R}} & \overline{\frac{\partial F_1}{\partial \psi_I}} & \overline{\frac{\partial F_1}{\partial N_1}} & \overline{\frac{\partial F_1}{\partial N_2}} \\ \overline{\frac{\partial F_2}{\partial \psi_R}} & \overline{\frac{\partial F_2}{\partial \psi_I}} & \overline{\frac{\partial F_2}{\partial N_1}} & \overline{\frac{\partial F_2}{\partial N_2}} \\ \overline{\frac{\partial F_3}{\partial \psi_R}} & \overline{\frac{\partial F_3}{\partial \psi_I}} & \overline{\frac{\partial F_3}{\partial N_1}} & \overline{\frac{\partial F_3}{\partial N_2}} \\ \overline{\frac{\partial F_4}{\partial \psi_R}} & \overline{\frac{\partial F_4}{\partial \psi_I}} & \overline{\frac{\partial F_4}{\partial N_1}} & \overline{\frac{\partial F_4}{\partial N_2}} \end{bmatrix} \cdot \begin{bmatrix} \overline{\Delta \psi_R} \\ \overline{\Delta \psi_I} \\ \overline{\Delta N_1} \\ \overline{\Delta N_2} \end{bmatrix} = - \begin{bmatrix} \overline{F_1} \\ \overline{F_2} \\ \overline{F_3} \\ \overline{F_4} \end{bmatrix} \quad (3.4)$$

here $\overline{F_1}$, $\overline{F_2}$ are vectors that represent the real and imaginary components of Equation 3.2a. $\overline{F_3}$,

$\overline{F_4}$ are vectors that represent Equation 3.2b and c. The derivative matrices are partial derivatives

of equation 3.2a, b, c for $\overline{\psi}$, $\overline{N_1}$, $\overline{N_2}$ (for instance $\overline{\frac{\partial F_1}{\partial \psi_I}}$ is formed by taking partial derivatives of

the real components of Equation 3.2a with respect to the imaginary components of ψ ;

$\overline{\frac{\partial F_1}{\partial \psi_I}}_{i,j} = \frac{\partial F_1(\psi_{Ri}, \psi_{Ii}, N_{1i}, N_{2i})}{\partial \psi_{Ij}}$). It is also important to remember that the propagation

eigenvalue λ is another unknown. Including λ , there are $4m+1$ unknowns where m is the length

of the discrete vectors, the field solution is complex with $2m$ unknowns and the carrier densities

N_1 and N_2 each have m unknowns. However one unknown from the imaginary part of the field ψ

can be removed, since $\psi(x).e^{-\tan^{-1}(\psi_{Ik}/\psi_{Rk})}$ is also a soliton solution. Subsequently in the

matrix solution the place of ψ_{Ik} is taken by the λ . In order to help the convergence of this

relaxation scheme, the estimated solutions in every step could be calculated with the help of some functions;

$$\psi_{estimate} = \psi_{init} + \Phi(\Delta\psi) \quad (3.5)$$

Even though more complicated estimation functions could be used, the following linear function has been used throughout the simulations in this thesis; $\Phi(\Delta\psi) = \zeta.\Delta\psi$ and good convergence has been achieved for $0 < \zeta \leq 1.0$.

The peak field values for the dissipative solutions are plotted in Figure 3.2 as a function of the small signal gain coefficient (δG) that is defined as the net gain for the background ($\delta G = \overline{f}(N_1, N_2) - \alpha$) where N_1 and N_2 are calculated for $\psi \cong 0$ as the pumping level π is increased). The dissipative solutions bifurcate subcritically ($\partial\psi / \partial\delta G < 0$) from the $\delta G=0$ point. Equation (3.1) also has $\psi=0$ solutions, which are stable for $\delta G < 0$, and unstable for $\delta G > 0$. Stable dissipative solutions can only appear for $\delta G < 0$, since the background noise level has stable solutions ($\psi=0$) in that region. The threshold pumping current level for stable solitons was estimated to be 4A, for a 300 μ m wide and 1cm long device.

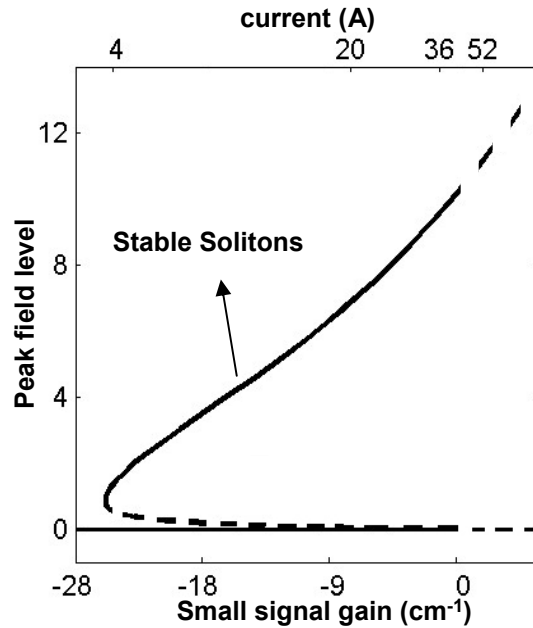


Figure 3.2 Plot of the peak field level($\sqrt{mW / \mu m}$) of the solitons versus the small signal gain δG . The dashed line shows the unstable solutions, and the dark line shows the stable solitons. Current values (horizontal axis-top scale) are calculated assuming 300 μm width contact patterns on a 1cm long device.

3.3 Device fabrication

The device was fabricated in the CREOL clean room. $\frac{1}{2}$ of a 2" wafer, which was grown by C. H. Lange in University of Jena-Germany, was used in the fabrication. These wafers were already tested previously in Jena for laser diode fabrication, and the diodes gave encouraging results (Figures 3.3 and 3.4). Having seen these results, a piece of this wafer was obtained for the PPSOA experiment

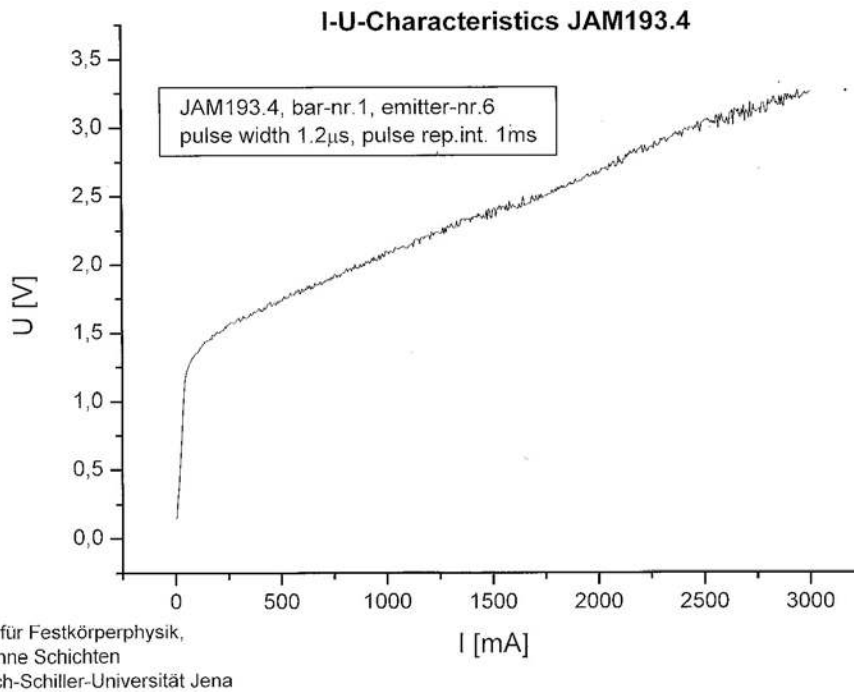
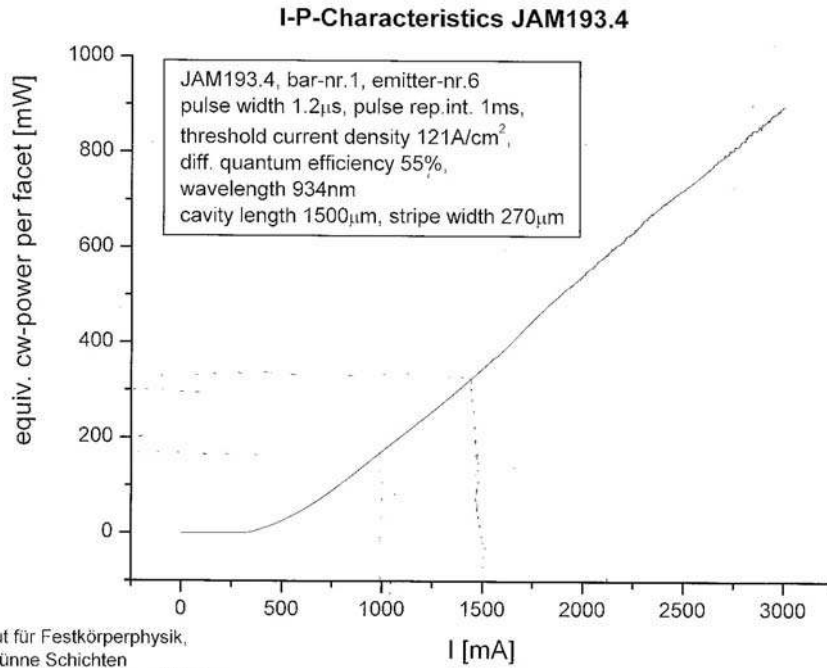
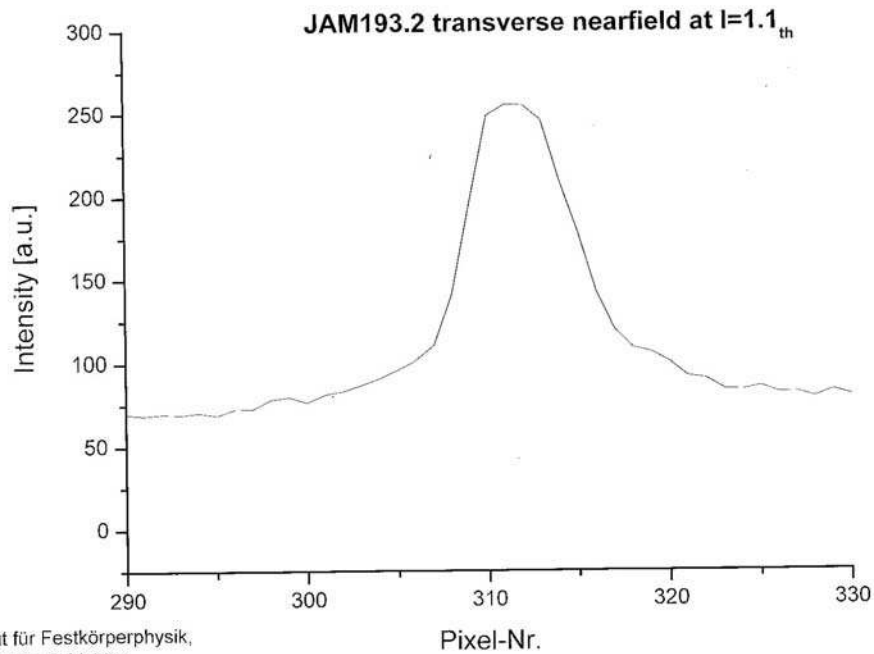
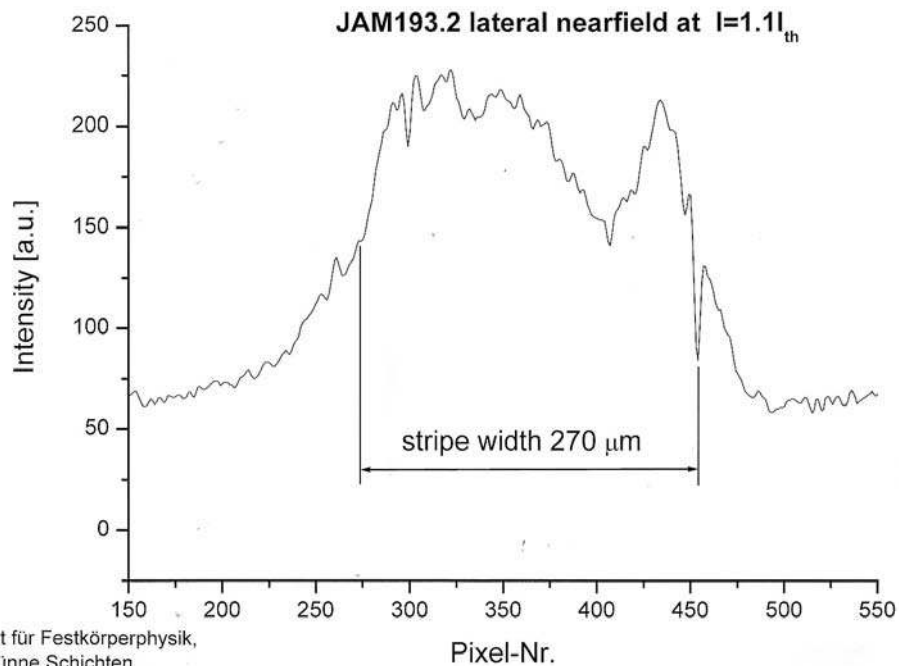


Figure 3.3 Current vs power and voltage characteristics of broad area diodes with SQW wafer grown in Jena.



Institut für Festkörperphysik,
AG Dünne Schichten
Friedrich-Schiller-Universität Jena



Institut für Festkörperphysik,
AG Dünne Schichten
Friedrich-Schiller-Universität Jena

Figure 3.4 The transverse and lateral mode profiles of broad area gain guided laser diodes for the SQW wafer grown in Jena.

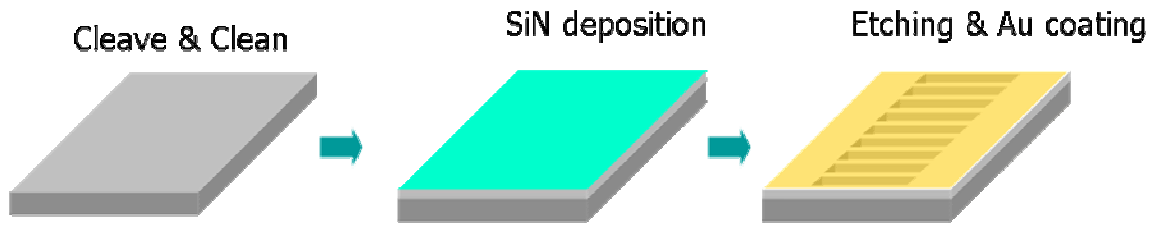


Figure 3.5 Device fabrication steps: first samples are cleaved & cleaned; then the insulator is deposited followed by lithography and contact deposition

Sample preparation;

1. First the 5mm by 1.5cm long samples were cleaved from the wafer, and standard alcohol cleaning procedures applied (5 min in acetone @ 119 °C, 5 min in methanol @ 150 °C, 5 min in isopropanol @ 150 °C). Later the sample was dipped into HF acid for about 1 min, in order to clean oxides from the surface layer. The samples were then rinsed in DI water, blow-dried with nitrogen. As a last step in the initial cleaning procedure, the samples are heated up and held at 150 °C on the stove for 5 min in order to evaporate the remaining liquids on the sample.
2. A plasma enhanced 150nm thick SiN layer was deposited as an insulator on the sample. SiN was preferred instead of SiO₂, since the deposition equipment in CREOL gave better surface profiles with SiN. As soon as the SiN deposition was finished, negative photoresist was spun onto the samples and was illuminated through a mask which had periodic lines of 10-50µm width, 300µm long with periods of 10-30µm. After lithography and developing, the openings of the photoresist layer on the SiN were used for dry etching with reactive ions. SiN etching was used to open the

- windows on the insulator oxide layer. The sample was chemically cleaned (as in step 1, but negative resist was removed with RR2-which is a negative resist remover chemical) one more time to remove the negative resist.
3. The contact layers were fabricated as follows. On the n-doped side of the semiconductor which is the bottom side of the device, the contact layer was composed of 5nm of Ni, 10nm of Ge and 200nm of Au. These metals were deposited with a thermal evaporator machine. Later the samples were flipped and top contact layers of 5nm of Au, 20nm of Zn and 300nm of Au were evaporated. Subsequently the devices underwent reactive thermal annealing
 4. The samples were cleaved using the crystal axes to create perfect facets for optical coupling. The devices were individually mounted on copper stages. The + and - contacts of the devices were separated by an insulator layer. Gold wires were bonded to the top of the device and + contact copper layer sheet. A silver conductive epoxy (EPO-TEK H20E) was used in order to mount the devices. The epoxy was heat cured at each step of the mounting around 100 °C for about 40 minutes.
 5. The mounted samples were put on a TE cooler as shown in Figure 3.7. The pulsed current source was soldered to the contact copper sheets by the special cable provided with the driver.

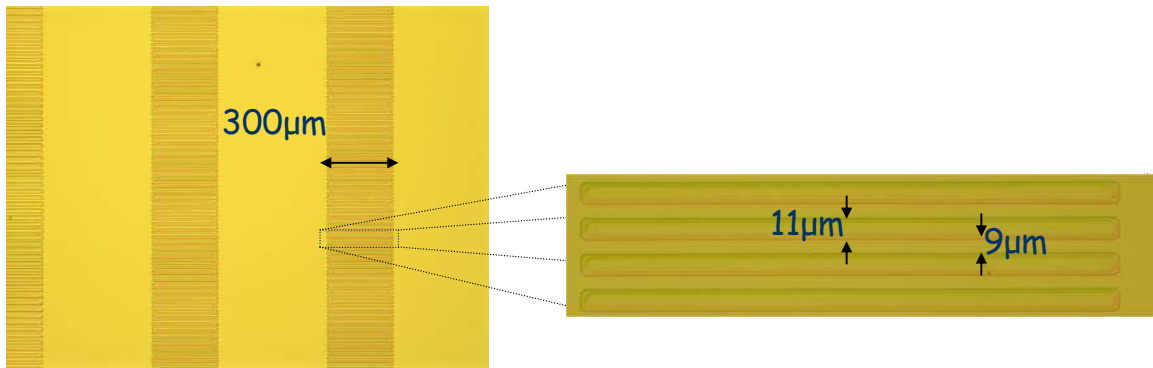


Figure 3.6 An optical microscope image of the top of the device.

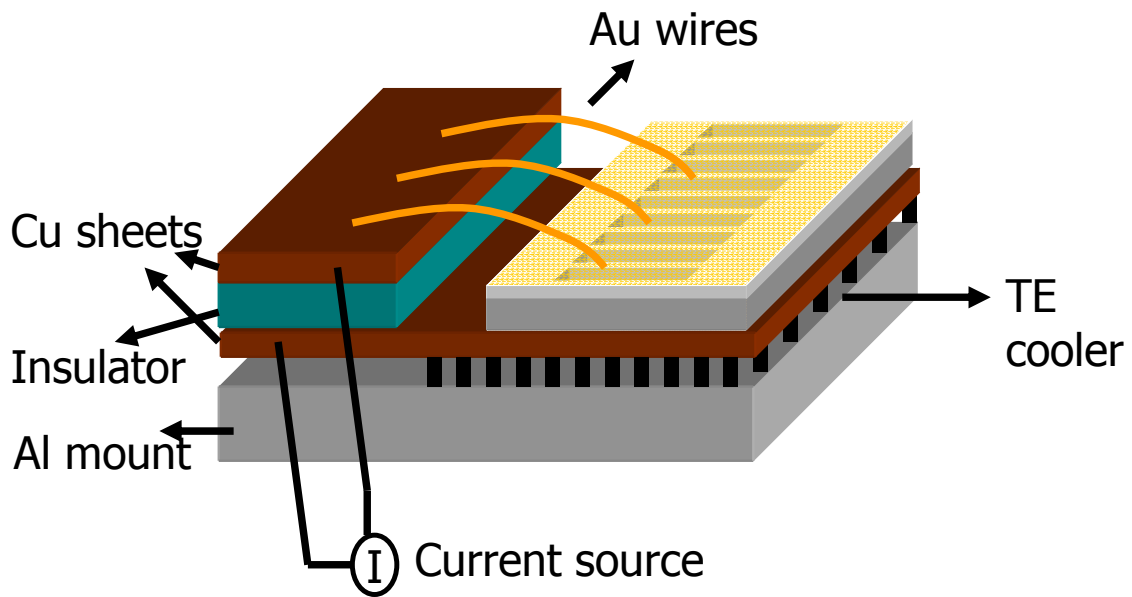


Figure 3.7 Gold wired device on a TE cooled waveguide stage.

3.4 Initial Experiments

The device length was about 1cm. In order to avoid thermal effects, a pulsed current source (400ns pulses at 1KHz repetition rate) was used. Stable temperatures ($\sim 21^\circ\text{C}$) for the devices in repeated experiments were guaranteed by mounting them on a TE cooled copper mount. Light input from a CW Ti:sapphire laser was shaped with a 2 lens elliptical telescope. A 40x microscope objective was used to couple the laser beam into the waveguide. Both focal planes (orthogonal (y-axis) and parallel (x-axis) to the waveguide) were carefully aligned to overlap after the microscope objective. This gave maximum coupling of light into the waveguide and a planar phase front at the input. The device was tilted about 2 degrees from normal incidence to avoid any back-reflections. The output of the sample was imaged onto a CCD camera with a microscope objective (see Figure 3.8).

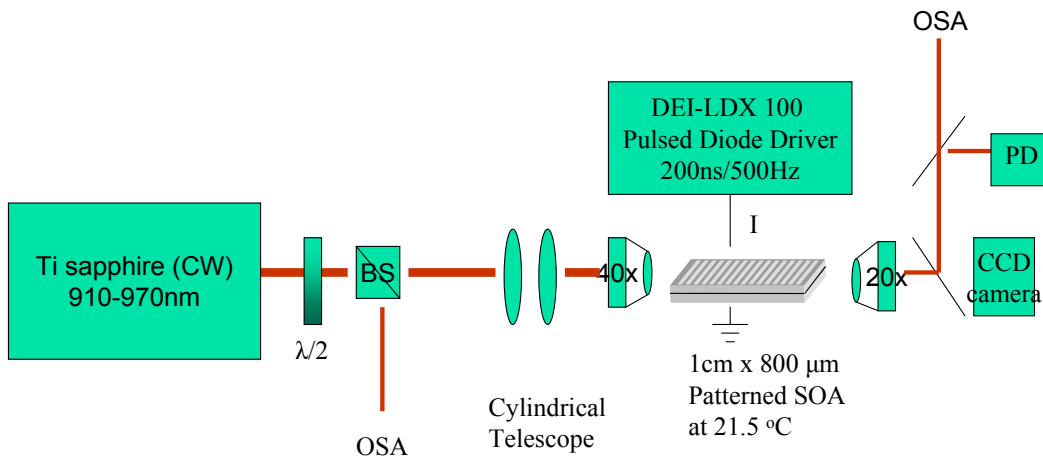


Figure 3.8 The coupling setup

When a 16.5 μm FWHM beam was coupled into the waveguide at a wavelength of 965nm (where the material is transparent), diffraction to 62 μm FWHM was observed as a result of the 3.6 diffraction lengths of linear propagation. When the wavelength was tuned inside the bandgap ($\lambda < 955\text{nm}$), and current was injected into the device, a localized spatial output beam with a FWHM of 21 μm at 950nm with 4A of current was observed (see Figure 3.9). Figure 3.10(a) shows the formation of such a localized beam. The device absorbed all the light until the current reached 3.8A. After this point the system followed the stable subcritical bifurcation branch (see Figure 3.11), and the peak intensity of the localized beam increases. The output profile does not show any formation of noise filaments up to 4.6A. At higher currents the amplified spontaneous emission increased above the subcritical branch, and generated noisy peaks on the sides of the soliton. By using a BPM code which uses Equation 3.1a and 3.1b, numerical simulations were performed for the patterned amplifier device. The simulations also supported the bifurcating behavior of the solitons with the corresponding threshold pumping current. See Figure 3.10(b) which indicates the turning point in the bifurcation diagram.

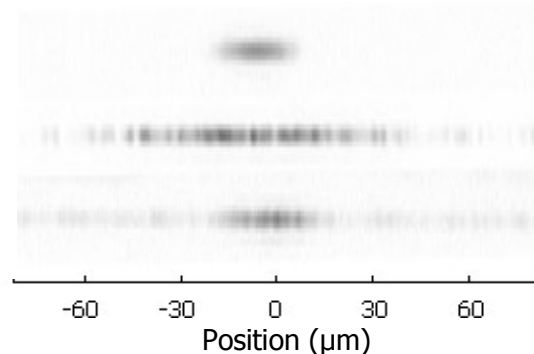


Figure 3.9 (Top) Input beam profile at $\lambda=965\text{nm}$, fitted to a Gaussian gave FWHM=16.5 μm , (Middle) Diffracted beam (to 62.5 μm FWHM at the output of sample), (Bottom) Output beam profile for $\lambda=950\text{nm}$, at 4A current injection.

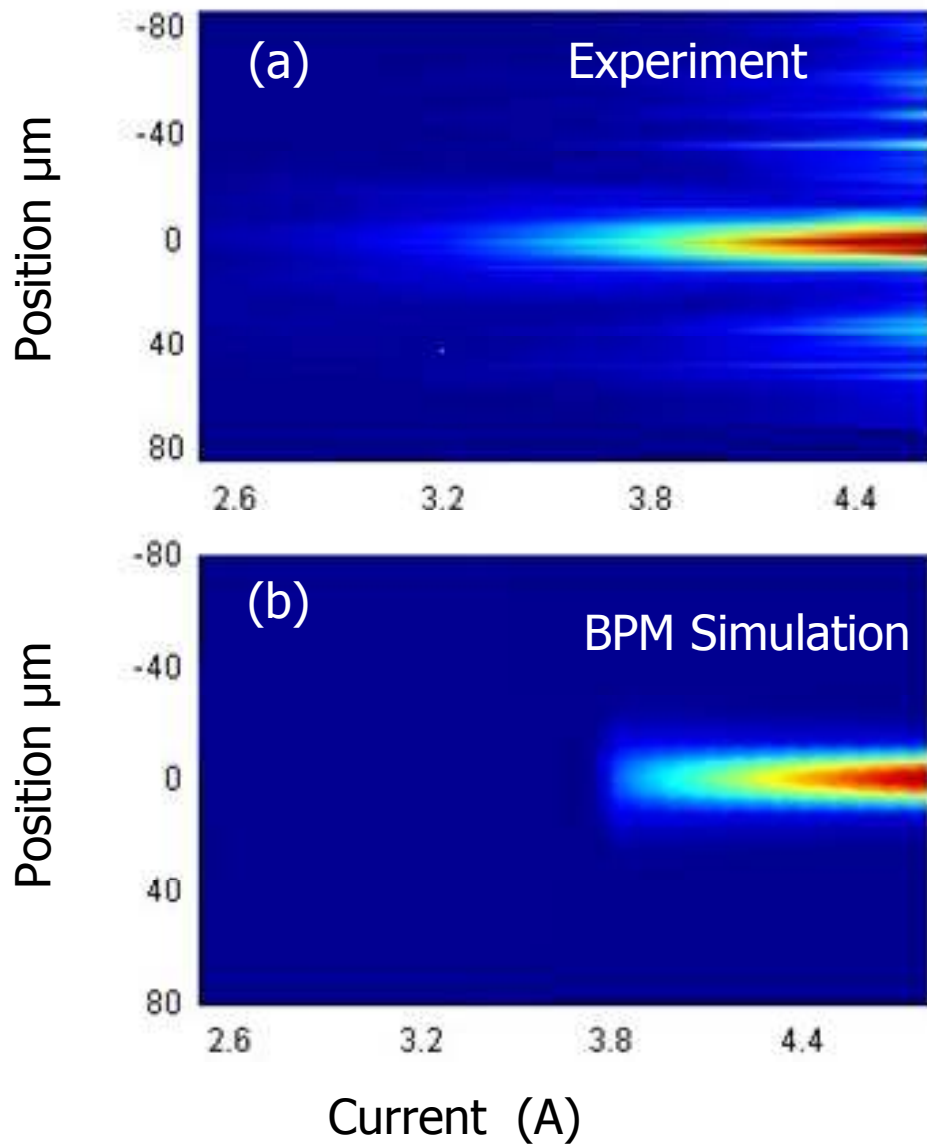


Figure 3.10 (a) Collage of images from the output facet when the measured input at the front facet is 160mW & 16.5 μ m FWHM. (b) Collage of numerical simulations of the output profile with a 55mW & 17.5 μ m FWHM Gaussian input into the waveguide.

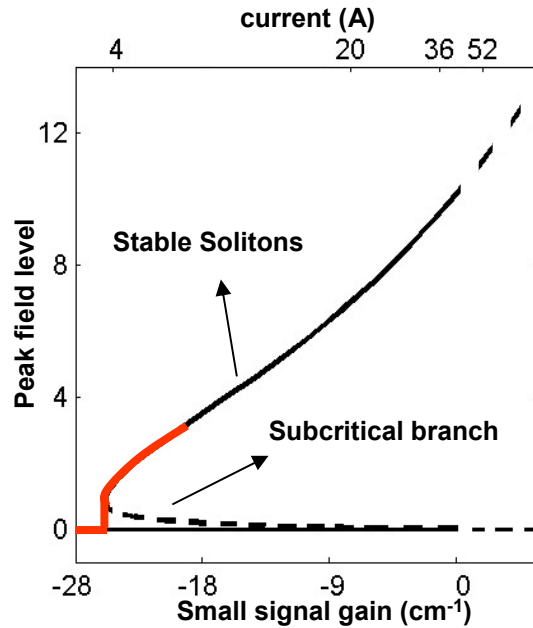


Figure 3.11 The output behavior of the device (shown by red line) on the bifurcation diagram.

Next the properties of the spatial soliton that identifies it as a dissipative soliton will be discussed. To this end it was shown that for fixed values of system parameters, most specifically material parameters such as the saturable loss and gain and the pumping current, the soliton is a stable attractor and no *families* of solitons exist at fixed parameters. Beyond 60mW input power, the beam forms a localized structure that does not change its shape or intensity, although the input power is increased, as expected for dissipative solitons. The sample facets were checked for defects by imaging after cleaving, and only perfectly cleaved samples have been used. In the region of attraction an arbitrary initial input beam will always converge towards one, distinct soliton (also called a *auto-signal recovery* property). By using a half wave plate and a polarizer

the input power was increased and a series of pictures of the output was taken, Figure 3.13(a). The striations observed in the experimental pictures were found to be the effect of sample defects inside the waveguide. It was observed that the stripe locations on the output image move with the sample when the sample is shifted perpendicular to the laser's propagation axis. Therefore they are a consequence of localized intrinsic defects in the waveguide. Numerical simulations in Figure 3.13(b) show that once the intensity exceeds the subcritical branch value for a given pumping current, the soliton does not change its intensity or width as observed in the experiment. This could easily be observed on the bifurcation diagram where there is only one stable crossing of the bifurcation diagram while the intensity is changing (Figure 3.12)

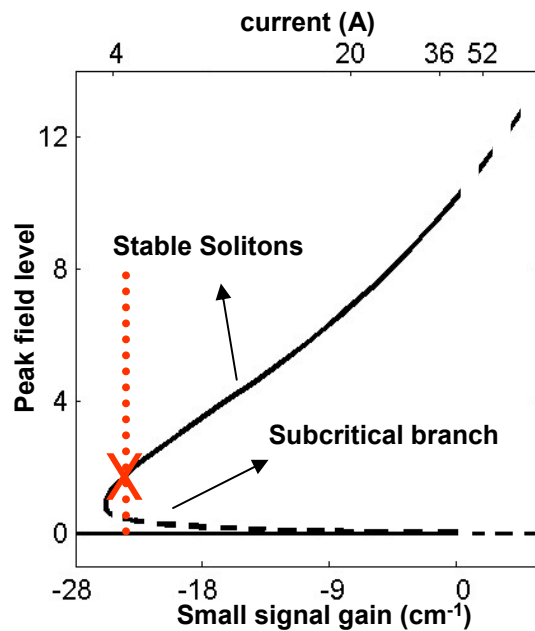


Figure 3.12 The behavior of the device's output on the bifurcation diagram when the input intensity is changed.

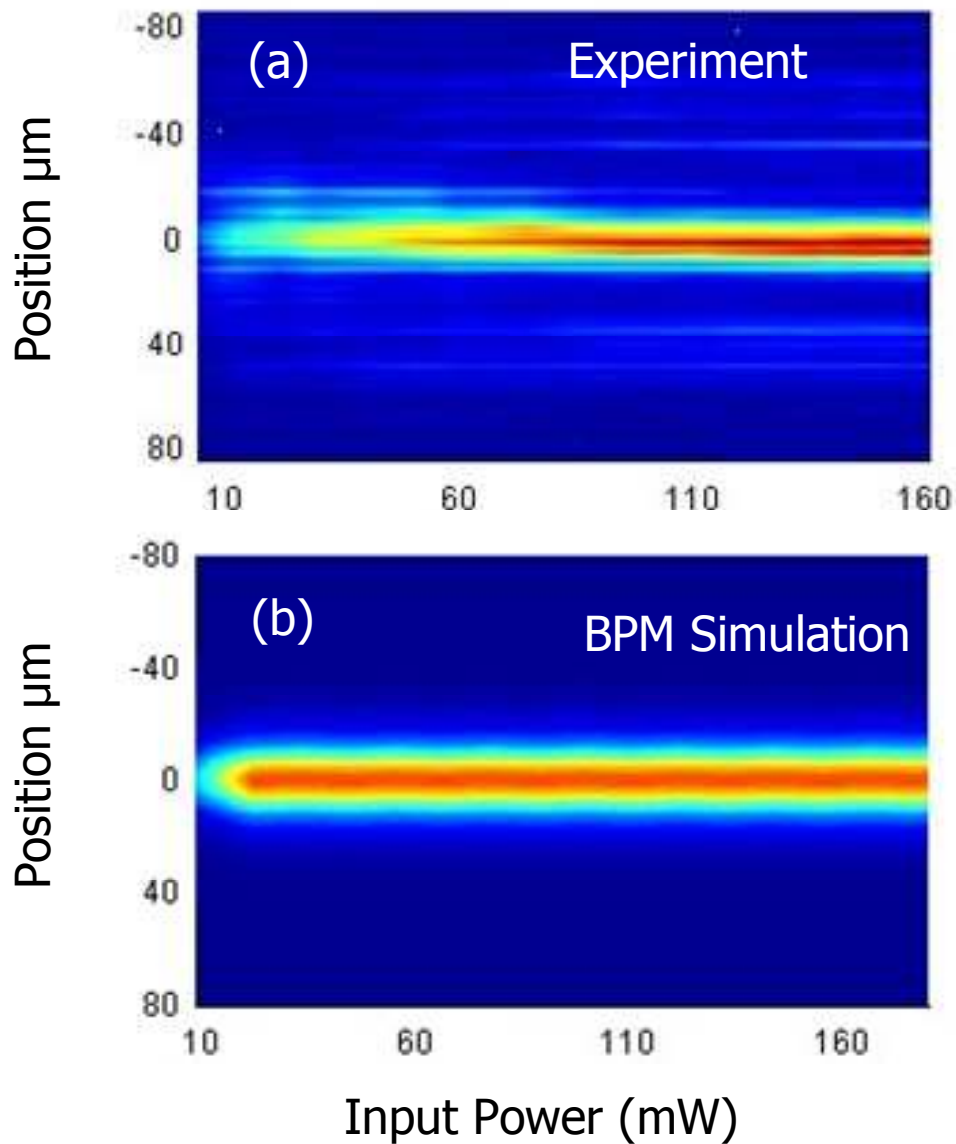


Figure 3.13 (a) Images from the output facet at 4A pumping when the input optical power is increased. (b) Numerical simulation of the solitons at 4A pumping when the input intensity at the front facet is increased (50% coupling is assumed).

Also analyzed was the change in the output beam waist induced by increasing the input beam waist from $7\mu\text{m}$ FWHM to $60\mu\text{m}$ FWHM (Figure 3.14). For an input beam waist smaller

than $13\mu\text{m}$, the beam diffracted very fast, and numerical simulations show that it gets totally absorbed if the propagation continues after the 1cm device length. From $15\mu\text{m}$ to $35\mu\text{m}$ input FWHM, a stable localized soliton without a significant change in the output beam waist was formed. Larger input beam waist coupling did not give any soliton for a 1cm device length, since the diffraction length at these beam waists was greater than 1cm. However numerical simulations show that for longer propagation distances, formation of multi-solitonic structures is possible.

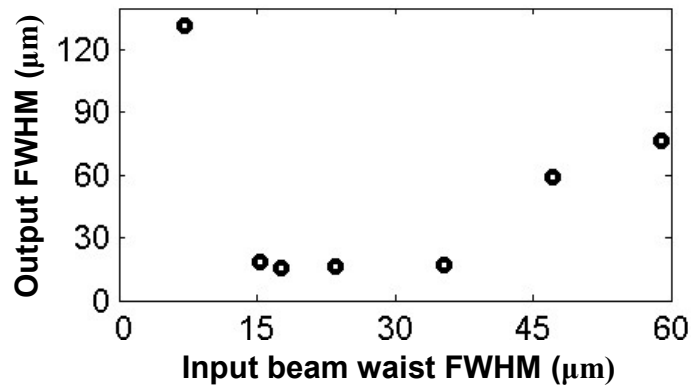


Figure 3.14 Output beam waist versus a variable Gaussian input beam width for 160mW input power at the front facet, and 4A current injection.

Six different devices from the same wafer were investigated. All of them gave essentially the same output images for similar conditions. Thus it was concluded that these solitons are very robust since dissipative solitons are strong attractors in these systems.

The wavelength dependence of the solitons was another interesting issue, since the semiconductor gain and linewidth enhancement factor change with frequency as shown in Figure

2.4. In the results shown in Figure 3.15, at 4.6A pumping, the output beam waist at FWHM was 39.3 μm , 15.9 μm and 15.3 μm , for a, b and c, respectively. It was not possible to tune the wavelength continuously because of the birefringent tuning mechanism in the laser. Numerical soliton solutions also show that there is an increase of soliton waist with a decrease in gain and linewidth factor which occurs as the wavelength is decreased (see Figure 3.16). Also the peak intensity of the solitons decreases at the same time.

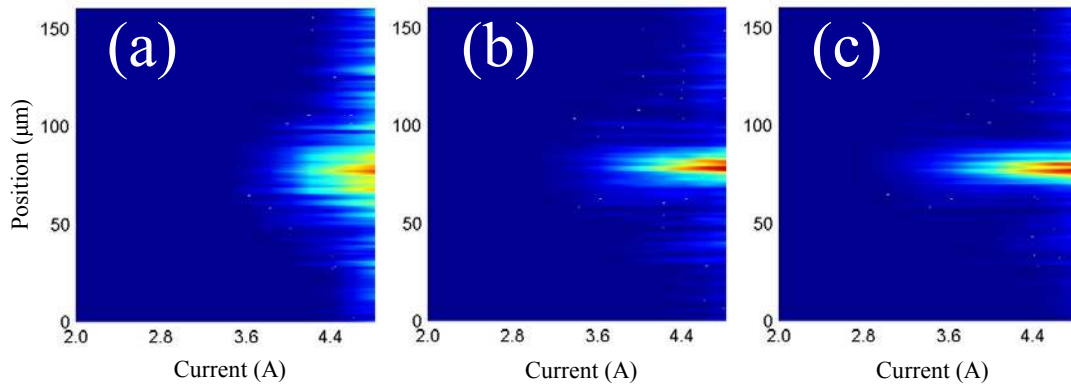


Figure 3.15 Images from the output facet when the measured input at the front facet was 160mW & 16.5 μm FWHM at wavelengths of (a) 941nm, (b) 946nm and (c) 950nm

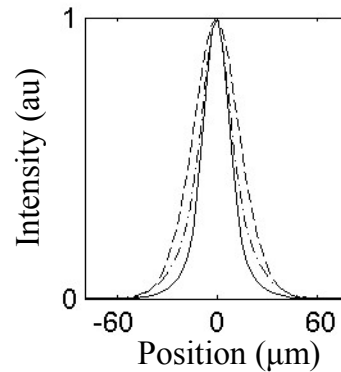


Figure 3.16 Normalized soliton profiles at different gain (g), and linewidth enhancement parameter (h), but at the same current density ($\pi=9.4$). Solid line $g=104\text{cm}^{-1}$, $h=3$; dashed dotted line $g=60\text{cm}^{-1}$, $h=3$; dashed line $g=60\text{cm}^{-1}$, $h=1$

3.5 Comparison of InGaAs and InP based QW devices for dissipative soliton experiments

The profiles of the dissipative solitons in PPSOA devices are dependant on the material properties. It was interesting to examine how the soliton profiles could have changed if we had used an InP wafer which was operating at 1550nm wavelength. 1550nm lies inside the main band of long distance optical communication networks, because of the low loss coefficients of single mode fibers around this wavelength.

InP technology is very similar to that of GaAs based devices. However GaAs wafer production has excelled as a result of the large amounts of laser diode production for CD players, and high power laser diodes. Thus the gain of the commercially available InP wafers are usually lower.

In 1.55 μm calculations, the parameters are changed for the gain and carrier model. Other parameters are assumed to be the same, but normalized coefficients are scaled by the wavelength, $\alpha = 0.052$, $N_{tr} = 2.2 \times 10^{18} \text{ cm}^{-3}$, $N_s = 1.3 \times 10^{18} \text{ cm}^{-3}$, $d = 60 \text{ \AA}$, $g = 48 \text{ cm}^{-1}$, $D = .966$, $B = 2.64$ and $C = 0.169$ [3.1].

The graphs of Figure 3.17 show the stable branch of the bifurcation diagram starting from the lowest current levels that supports solitons. It is seen that the power requirements at the same current for GaAs based QW (0.98 μm) and InP based QW (1.55 μm) solitons are very similar. However the main difference is in the beam waist of the solitons.

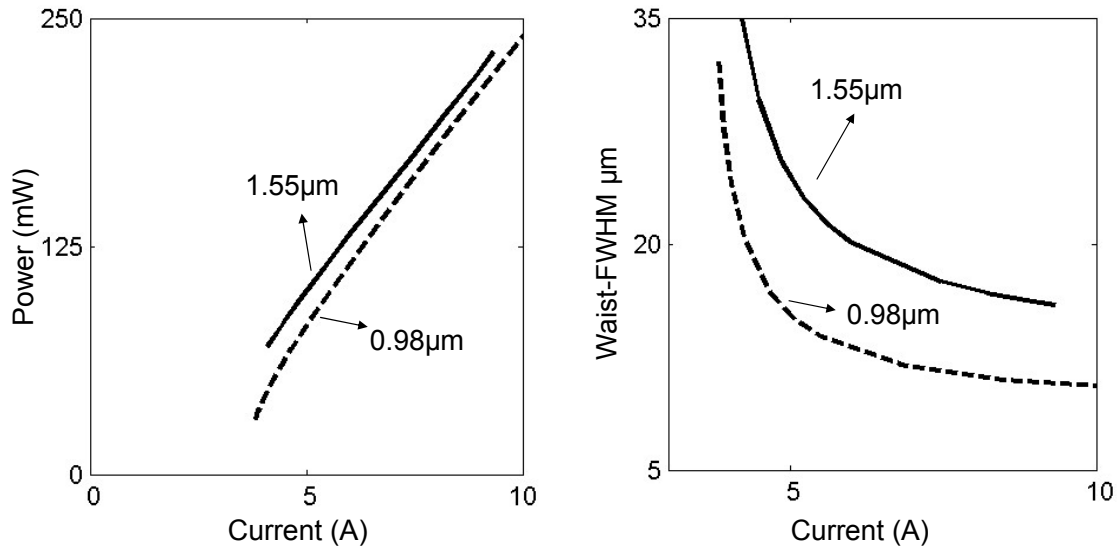


Figure 3.17 Left plot shows the powers required for stable solitons vs current. Right plot shows the Gaussian fitted beam waist of the solitons vs current.

Although this gives an idea about different wavelength based dissipative solitons, it is very difficult to generalize these results. It is probable that a quantum well device can be engineered to give very high gain and index change that will support a well confined low power soliton at 1550nm.

3.6 Conclusions

In conclusion, stable spatial dissipative solitons in a semiconductor optical amplifier device have been observed for the first time. The numerical simulations were modified to include the quantum well effects. Numerical simulations fit very well with the experiment results. With input powers of about 60mW for excitation, these solitons are very exciting for potential soliton applications.

CHAPTER FOUR: DISSIPATIVE SOLITON INTERACTIONS

“The true worth of an experimenter consists in pursuing not only what he seeks in his experiment, but also what he did not seek”

Claude Bernard

4.1 Introduction

The interactions between spatial optical solitons can have very interesting applications, such as all-optical switching, logic operations and soliton junctions [4.1]. As an example let's consider two beams from the same laser source injected into a waveguide (Figure 4.1). It is possible to modulate the phase or intensity of the beam using modulators (up to 40Ghz with commercial lithium niobate modulators). If one defines discrete output locations as output channels, soliton interactions should be able to function as optically controlled operations, as fast as the nonlinear response of the material. A good example of these operations in liquid crystals could be found in reference [4.2].

However the critical issue in implementing any such soliton application is to have a medium in which both the solitons can be generated with reasonable input powers (mWs), the response time is fast, preferably in the picosecond range, and the output optical signals are not attenuated on throughput to enable cascability. The PPSOA devices not only support fast switching and low power solitons, but are also compatible with standard semiconductor processing technologies and can be integrated with other semiconductor devices for operation

with optical communication networks (fibers, modulators, etc). Therefore they have significant advantages over solitons in photorefractive media which are slow and require holding beams, or in quadratic or Kerr media which require powers $>100\text{W}$.

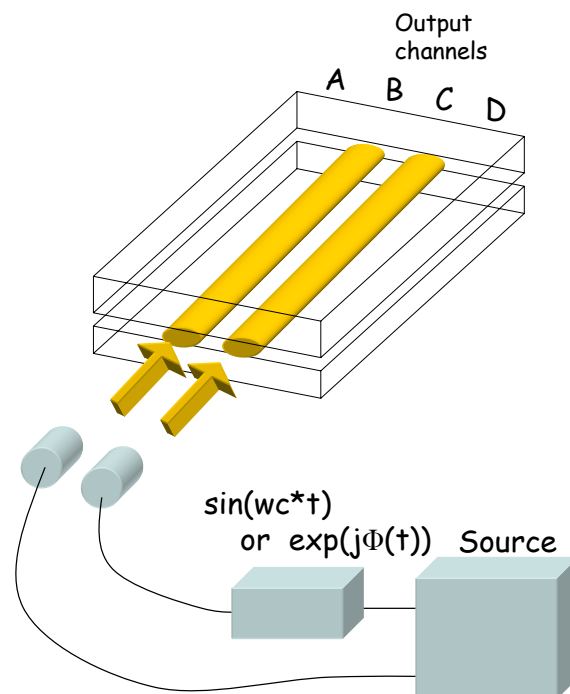


Figure 4.1 Beam interactions in waveguides could be implemented with phase or amplitude modulators. Moreover defining output channel positions could be used for soliton based optical operations.

Although a significant amount of work has been done on soliton interactions in general, the nature of dissipative soliton field interactions has not been addressed. Although there were preliminary numerical findings [4.3], the experimental verification of the simulations did not exist.

The interactions between two coherent dissipative solitons have been reported in PPSOAs for the first time [4.4]. The interactions have been investigated for pairs of solitons of equal power and width by changing the relative launch angle, distance and the relative phase between them.

4.2 Dissipative nonlocal effects

The solitons in PPSOA devices appear as a result of carrier dependant nonlinear effects (see Chapter 2). Therefore their interactions will not only include interference effects between the beams, but also the gain and refractive index are changed by the carrier induced nonlinearity. Carrier induced gain and refractive index distribution could be calculated by using Equation 3.1 where

$$\begin{aligned}\Delta g &= [f(N_1)w_1 + f(N_2)w_2]/(w_1 + w_2) - \alpha \\ \Delta n &= [[f(N_1)w_1 + f(N_2)w_2]/(w_1 + w_2)]x - h\end{aligned}\tag{4.1}$$

here Δg and Δn are gain and refractive index change respectively.

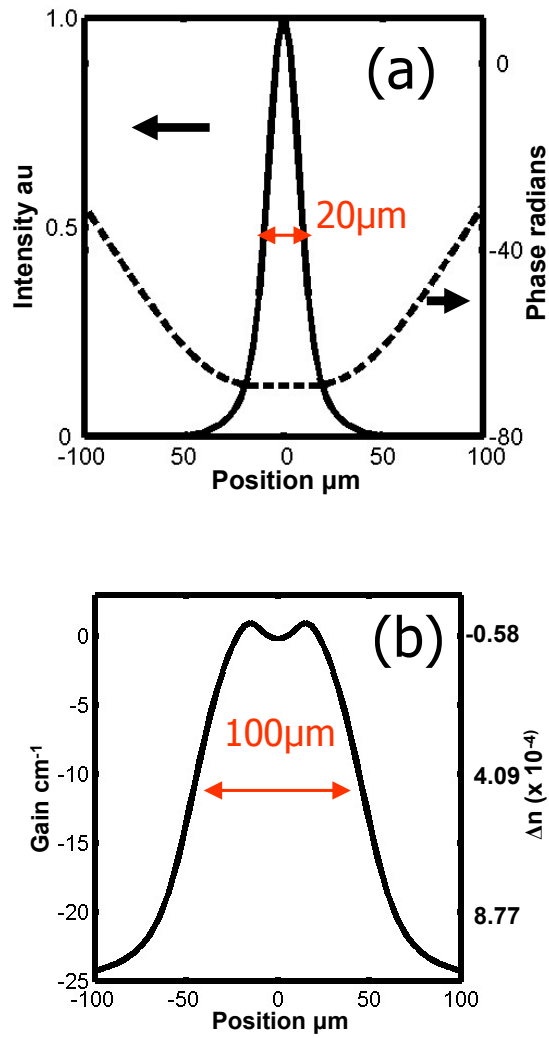


Figure 4.2 a) Calculated soliton intensity profile and phase at 4A electrical pumping with the corresponding change (b) in the gain and refractive index in the waveguide. (The gain and refractive index change is calculated with respect to the case when there is no current in the device). (Current $I = \pi q d N_{tr} A_{contact} / \eta$, where $A_{contact} = 300 \mu\text{m} \times 1 \text{cm} \times 0.5$)

In Figure 4.2, it is clear that because of the carrier diffusion effects, the nonlinearity is inherently nonlocal. A *nonlocal nonlinearity* is usually defined for refractive index effects when the index distribution induced by electric field has a wider spatial distribution than the field itself. In this case not only refractive index but also the gain profile have larger beam waist than the field. This should give different effects than nonlocal soliton interactions found in Hamiltonian systems [4.2, 4.5]. The refractive index change induced at the lowest possible current values that support the dissipative PPSOA solitons is about 10^{-3} in the waveguide.

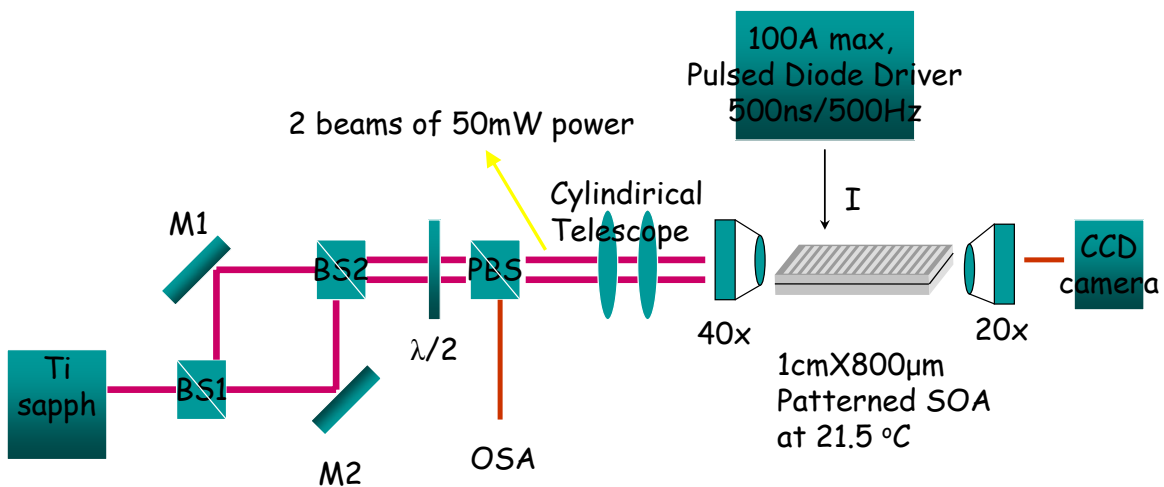


Figure 4.3 Experiment setup for investigating dissipative soliton interactions. Setting the distance between the beams and the relative propagation angles was facilitated by mirror M2. Moreover M2 was mounted on a piezoelectric stack in order to control the relative phase between the two arms of the interferometer.

The relative phase of the beam interactions was controlled by a Mach-Zender interferometer (Figure 4.3), and each beam had about 50mWs of power. The beams were elliptically shaped to 20μm FWHM at the input of the waveguide.

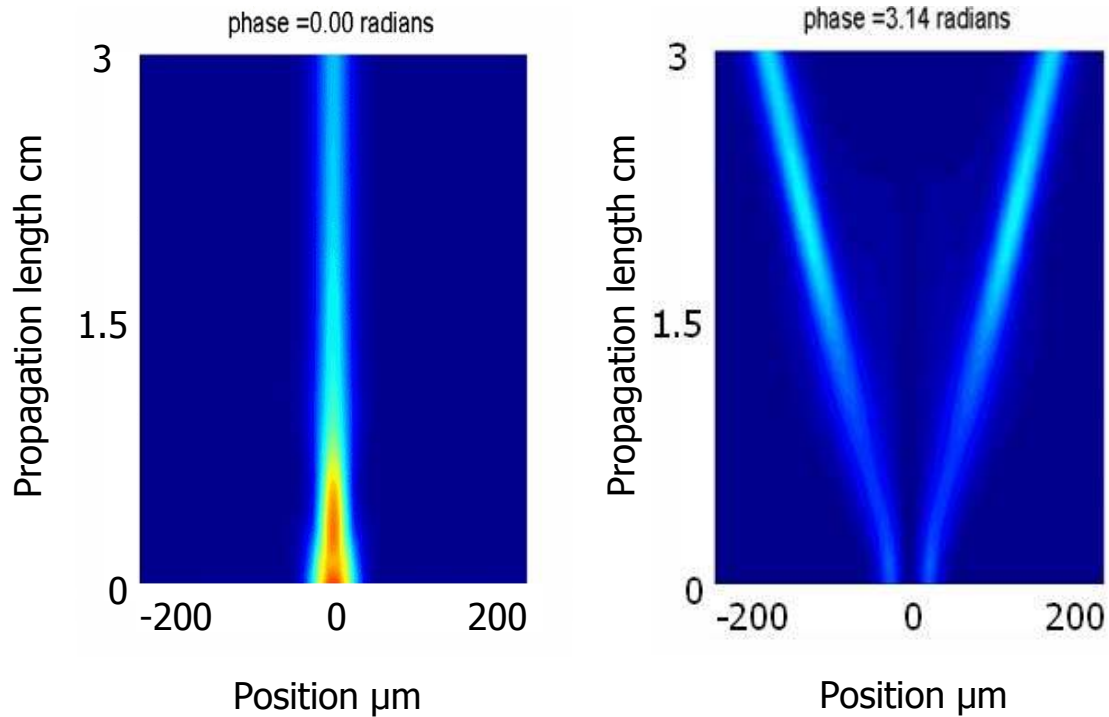


Figure 4.4 Evolution of the beams due to interactions in the local limit. The two beams interact and after about 3cm propagation, the output intensity of the solitons are the same, because of the zero-parameter property of dissipative solitons. The relative input beam phase is given above the pictures

First the interaction between parallel solitons separated by about one optical beam waist of 15 μ m was examined, i.e. in the local limit. The numerical simulations were done using a finite difference beam propagation code with the coupled equations 3.1a and b. Estimates of the coupling loss of 50% and a 30% loss due to Fresnel reflection were assumed for the simulations which utilized two Gaussian inputs inside the sample, each with a 15 μ m FWHM width and 38mW power. Figure 4.4 shows the numerical simulations for 0 and π phase difference. It is interesting to note the *automatic signal restoration property* of the interactions, which is

uniquely a dissipative soliton effect. The simulations were made for different relative phases and the beam profiles after 1cm of propagation are plotted vs phase in Figure 4.5 at $4A$ pumping. The solitons fused and were steered in angle except where the phase difference between them was π . At π phase, the two solitons repelled each other, and two peaks were observed at the output facet.

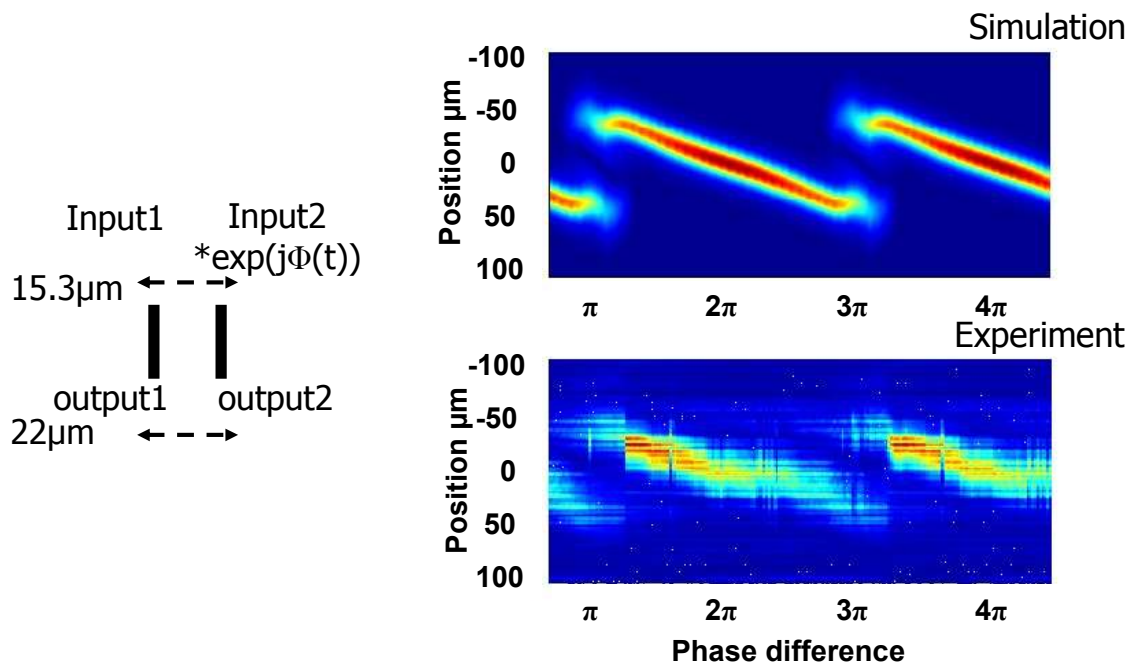


Figure 4.5 Output from the sample due to soliton interactions after 1cm propagation. The separation between the input beams is $15\mu\text{m}$ and $22\mu\text{m}$ at the output when each is excited separately. Top picture shows the numerical simulations, and the bottom the experiment results.

Experimentally, the difference between the two separately excited solitons at the output facet was measured to be $22\mu\text{m}$, so the angle between the two beams was about 0.04° . The output facet was imaged and data acquired at 200 pictures/30sec with the piezo-controlled mirror arm of the interferometer moving in every picture to change the relative phase. The experiment results

in Figure 4.5 (bottom) are in very good agreement with the simulations (Figure 4.5 (top)). The calibration of the phase difference (x axis) for the experiment was done using the simulation results as a reference, and the same calibration scheme was used for the subsequent experiments as long as there was no change in voltage control of the piezo. The striations in the output images were a result of interior defects in the waveguide as discussed previously [4.6]. Thus when the soliton fields are strongly overlapped, the interaction force mainly depends on the relative phase just as in Kerr, photo-refractive and quadratic solitons [4.7]. When the two solitons are in phase, the total intensity in the area between them increases, and thus there was a local increase in the refractive index so that the beams attracted each other. The opposite happens for the out-of-phase case. However, note that because these are zero parameter solitons, the soliton outputs all have identical intensity, in contrast to other soliton interactions where the total energy is either conserved (1D Kerr case) or diminished due to radiative losses.

Next the separation between the beams was increased at the input while keeping the angle between them at almost 0° . Over a small range of input beam separations for zero relative phase, 3 soliton-like outputs were predicted in Figure 4.6a with one well-defined high intensity soliton traveling along the initial propagation axis and the two other localized solitons diverging. The creation of the central soliton was a consequence of the non-local nature of the nonlinearity (or carrier density profile) so that the addition of the two gain profiles of the input solitons evolves with distance to form another “waveguide” that could support a soliton (Figure 4.6c). Note that the central soliton initially had a higher intensity than either of the satellite solitons due to the different nonlinearity and gain distributions in the center versus the wings. Further numerical simulations showed that all 3 solitons stabilized to equal intensities (to zero parameter solutions)

when they propagate far enough so that the gain profiles no longer overlap significantly. On the other hand when the relative input phase difference is around π , no additional peak in the gain occurs and only two solitons are obtained at the output (Figure 4.6b). Although the formation of a middle soliton at first sight appears very strange, it is however important to note that even though the beams are very far apart from each other, there is always an interaction through the tails. This small interference in the tails is seeding the middle gain guide, and creating a soliton. At π phase difference the interference on the tails is a dark region and because of that there is no seeding of the gain guide in between and the beams do not interact.

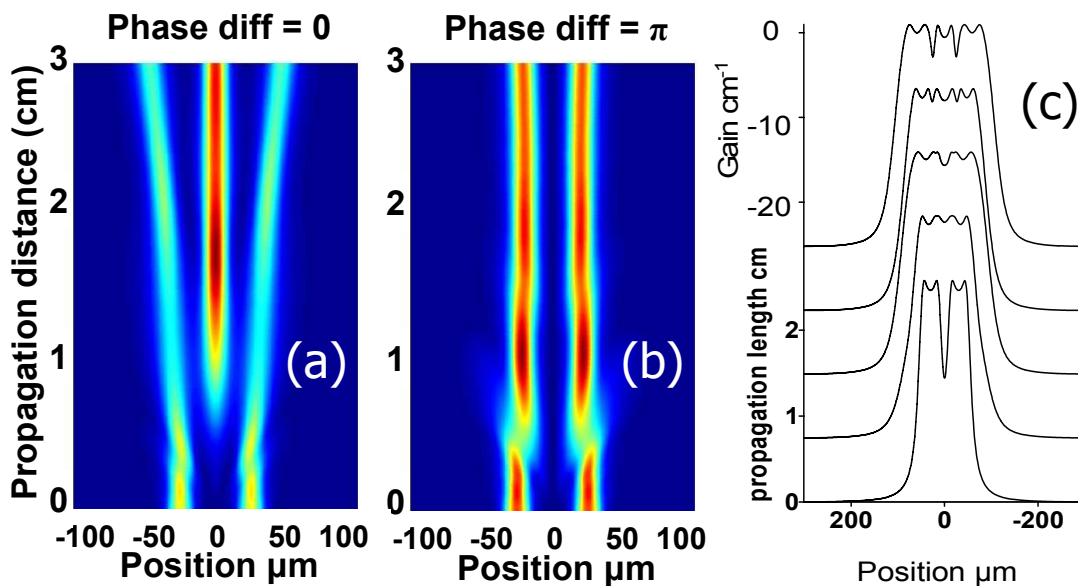


Figure 4.6 Numerical beam propagation over 3cms of soliton interaction (a) for 0 and (b) π phase difference. The initial separation between the input beams was $60.2 \mu\text{m}$ and each had 38 mW power. (c) shows the gain profile around the solitons for 0 phase difference at the input.

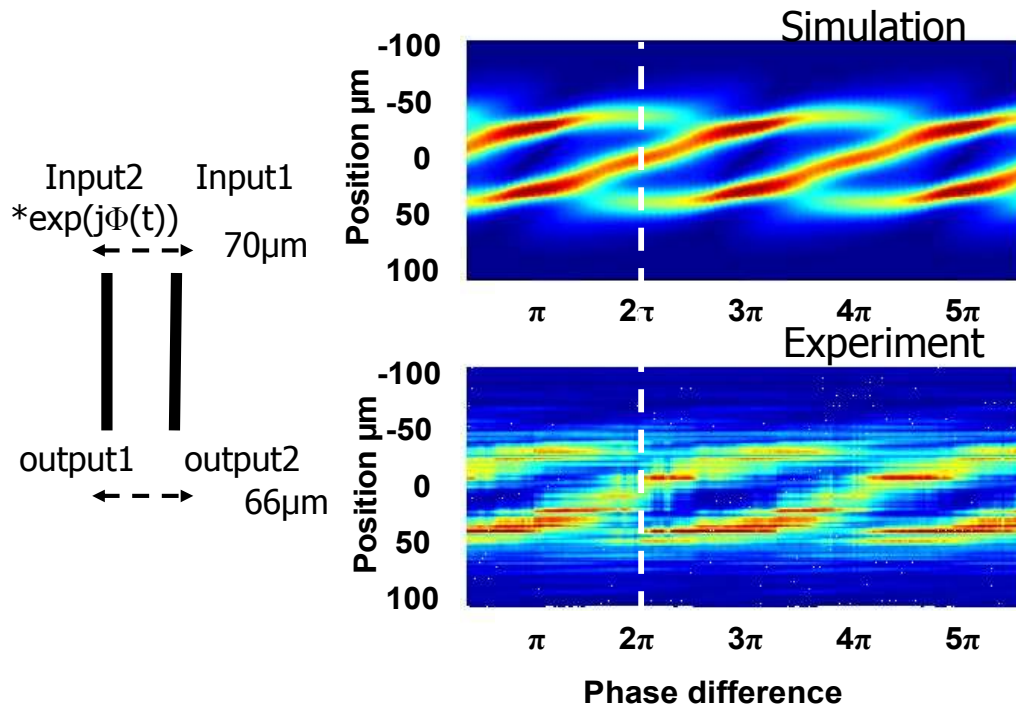


Figure 4.7 Output from sample due to soliton interactions after 1cm propagation. The separation between the beams when excited separately was $70\mu\text{m}$ at the input and $66\mu\text{m}$ at the output. Top picture shows the numerical simulations, and the bottom gives the experiment results.

Figure 4.7 shows the experimental results for the two soliton interaction with an initial $70\mu\text{m}$ separation between them. The solitons were separated by multiple soliton beam waists; thus there was only a non-local nonlinear interaction initially between the beams. However the phase in the soliton tails still affected the interaction as explained in the previous paragraph. This feature is different from the nonlocal Hamiltonian interactions [4.2, 4.5]. Note that at relative phases which were even multiple of 2π , there is evidence of three solitons present. Further simulations and experiments have shown that non-interacting solitons only occurred when the

separation between them was larger than $\sim 100\mu\text{m}$, since the gain profiles no longer overlapped significantly.

Another interesting case is the collision between incident solitons initially launched with crossing trajectories (non-collinear collisions). These interactions could be used in all optically induced junctions and logic operations [4.8, 4.9]. The collisions for a relative angle of around 0.5° have been investigated. The collision results were in very good agreement with the previously predicted simulations on slow velocity dissipative soliton interactions [4.10] for laser resonators (see Figure 4.8).

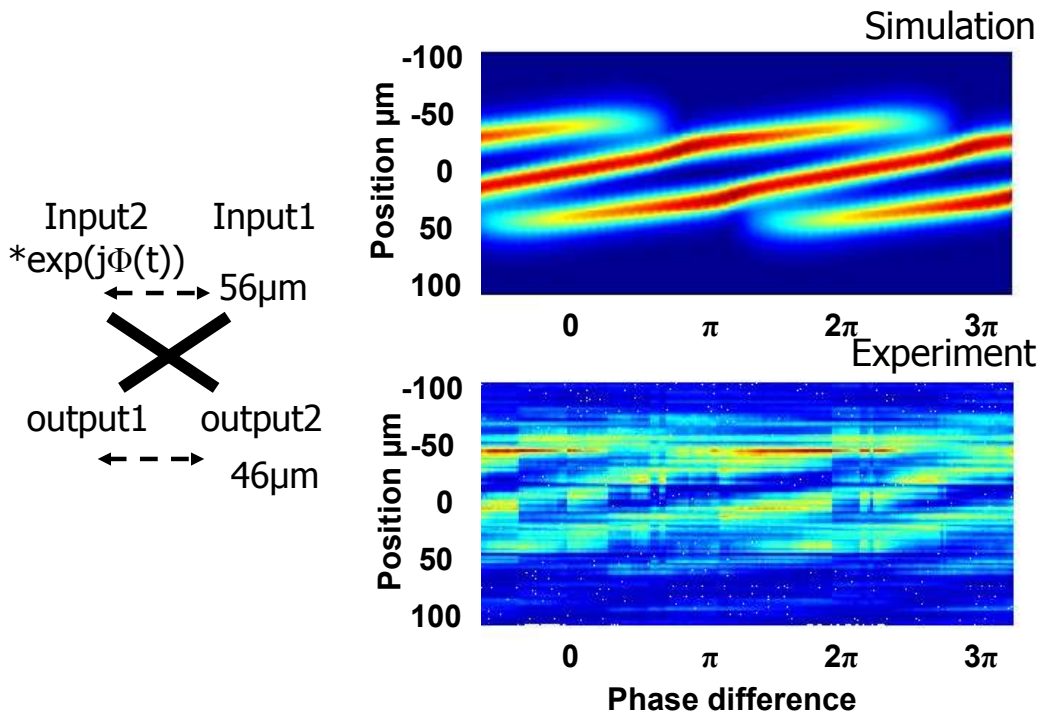


Figure 4.8 Output from sample due to solitons interacting with crossing trajectories after 1cm of propagation. The separation between the input beams was $56\mu\text{m}$ and the angle between them was 0.5° . Top picture shows the numerical simulations, and the bottom the experiment results.

Additional cases have also been analyzed; for example $50\mu\text{m}$ separated parallel interactions (Figure 4.9). The achievement in these simulations and experiments is significant, since there is very good agreement in all cases.

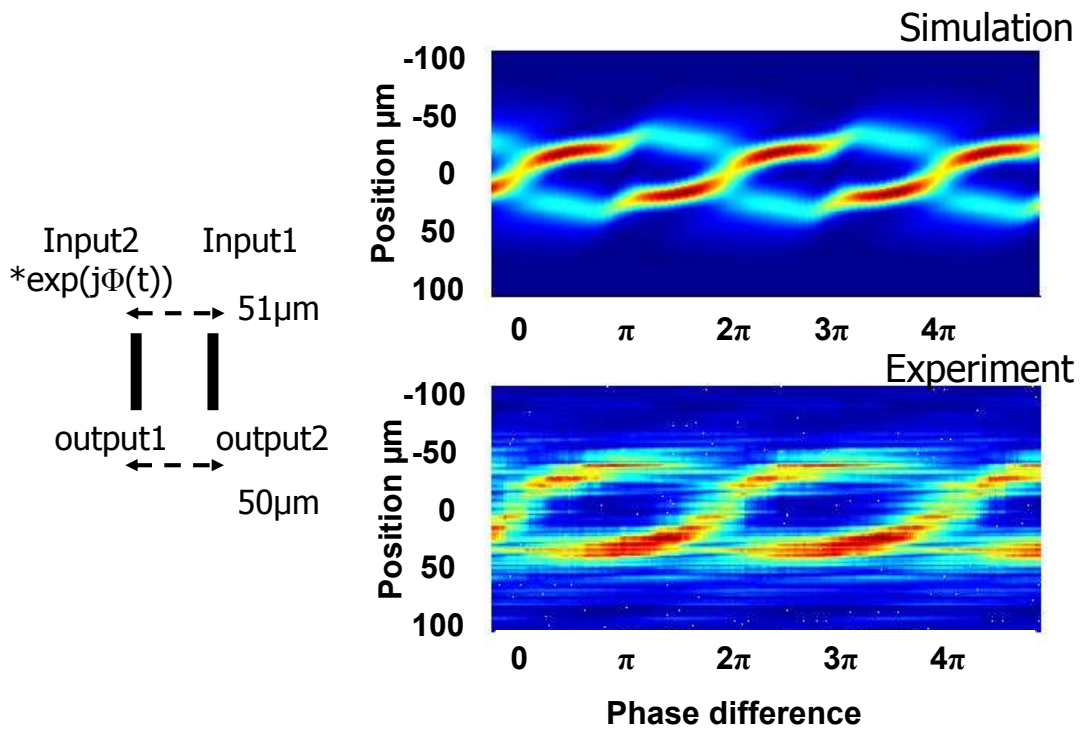


Figure 4.9 Output from sample due to soliton interactions after 1cm propagation. The separation between the input beams was $51\mu\text{m}$ and the separation of the positions of the output beams when separately excited was $50\mu\text{m}$. Top picture shows the numerical simulations, and the bottom the experiment results.

4.3 Conclusions

In conclusion the properties of zero parameter, dissipative, spatial soliton interactions in SOAs have been predicted and verified experimentally. The interaction between the beams can be either local or a non-local one, which, combined with the gain nature of the system, led to the generation of new solitons during collinear and non-collinear interactions. Due to the low powers required (<60mW for each soliton outside the sample) and the fast response time of the semiconductor device, all optical switching and logic devices based on soliton interactions can become a reality.

CHAPTER FIVE: MODULATION INSTABILITY

“There are things which seem incredible to most men who have not studied mathematics”
Aristotle

5.1 Introduction

Modulation Instability (MI) appears in nonlinear systems as a result of the growth of small amplitude and/or phase perturbations due to the interplay between nonlinearity and diffraction. The sources of the perturbations could be scattering, noise or external seeding. Broad optical beams or quasi-plane waves under appropriate conditions, will form filaments throughout propagation. Typically MI appears in the same parameter region (e.g. peak intensities) as bright solitons. The relationship between MI and solitons is apparent when the filaments formed through MI can actually evolve into trains of solitons.

This is certainly the case for dissipative PPSOAs. During the initial simulations of the patterned amplifier system, broad optical beams (usually beams with a rectangular profile with exponential decaying tails) were used as inputs. Patterns formed over the broad beam as a result of MI, and the periods of these beams were used as initial guesses of the sech profile inputted into BPM simulations for finding solitons.

MI in one dimension (1D) has been previously investigated for numerous nonlinear processes; in coherent [5.1, 5.2] and incoherent systems [5.3]. Periodic patterns in two dimensions have also been observed [5.4]. Modulational instability in time in dissipative systems

has been analyzed for laser oscillators [5.5, 5.6], and in space for semiconductor microresonators [5.7]. There have also been experimental [5.8] and analytical studies [5.9] of MI in SOAs. To the best of our knowledge, this is the first analytical investigation of dissipative spatial patterns for a nonlinear propagating system with gain that supports *stable* solitons.

5.2 Theory and Simulations

A broad spatial beam may form periodic filaments that grow in amplitude in the spatial frequency domain. The initial growth of these MI filaments can be analyzed with a small signal analysis [5.10]. In order to see which frequencies are favored by the system, the small signal perturbations are assumed to be periodic functions. Naturally the perturbations in the devices have a very broad spectrum. The sources of this spectrum could be fabrication non-uniformities in wafers, seeding noise on the input, and thermal fluctuations along the device, etc. As long as the effect of these non-uniformities is small compared to the plane wave (PW) -homogenous- solutions of the system, the results of MI analysis are valid.

The “average” model equations for this analysis, i.e. where the absorption and gain effects are included in the same propagation equation as discussed in Chapter 3 are as follows;

$$\psi_z = \frac{i}{2}\psi_{xx} + \psi[\bar{f}(N_1, N_2)(1 - ih) - \alpha]$$

$$DN_{1xx} + \pi - BN_1^2 - CN_1^3 - f(N_1)|\psi|^2 = 0 \tag{5.1}$$

$$DN_{2xx} - BN_2^2 - CN_2^3 - f(N_2)|\psi|^2 = 0$$

here $\bar{f}(N_1, N_2) = f(N_1)\bar{w}_1 + f(N_2)\bar{w}_2$; $f(N_{1(2)}) = \ln((N_{1(2)} \cdot N_{tr} + N_s)/(N_{tr} + N_s))$;

$\bar{w}_{1(2)} = w_{1(2)}/(w_1 + w_2)$. Assuming a perturbation for the field and carrier density of the form;

$$\psi = (\psi_0 + \varepsilon(x, z)) \exp(j\beta z); N_{1(2)} = N_{10(20)} + n_{1(2)}(x, z), \quad (5.2)$$

ε , n_1 , n_2 are small perturbations of the homogenous plane wave solution parameters ψ_0 , N_{10} and N_{20} . $\varepsilon(x, z)$ is written as a sum of two periodic modulations on x , i.e. $\varepsilon(x, z) = a(z) \exp(jpx) + b(z) \exp(-jpx)$ where “ p ” is the spatial frequency. Plane wave analysis (ignoring diffraction and the perturbations) for ψ_0 , N_{10} and N_{20} gives;

$$j\beta\psi_0 = \psi_0[\bar{f}(1 - ih) - \alpha]; \quad \beta = -\alpha h; \quad \bar{f} = \alpha \quad (5.3)$$

These PW solutions could also be used to plot the saturation curves of the absorber and amplifier sections in a PPSOA in order to see the PW bifurcation behavior (see Chapter 2 for system gain saturating behavior vs intensity). Equations 5.1 are then linearized for the small signal quantities defined in Equation 5.2 which results in coupled small signal equations of the form;

$$\varepsilon_z = \frac{j}{2} \varepsilon_{xx} + r_o [\bar{N}_1 \bar{w}_1 n_1 + \bar{N}_2 \bar{w}_2 n_2] (1 - ih) \quad (5.4a)$$

$$D.n_{1(2)xx} + \gamma_{1(2)} n_{1(2)} - f_{1(2)} r_o (\varepsilon^* + \varepsilon) = 0 \quad (5.4b)$$

here $\bar{N}_{1(2)} = N_{tr}/(N_{10(20)} N_{tr} + N_s)$; $\gamma_{1(2)} = -2BN_{10(20)} - 3CN_{10(20)}^2 - \bar{N}_{10} r_o^2$. Linearization is achieved by using series expansion of the nonlinear terms in Equation 5.1 around the

homogenous solutions; ψ_0 , N_{10} and N_{20} . Equations 5.4 describe the evolution of the perturbations with propagation distance.

The homogenous field solution is assumed to be real; $\psi_0 = r_0$. Actually it can in principle be complex $\psi_0 = r_0 e^{j\theta}$. However the phase is not dependent on the propagation direction. Thus there is no loss of generality by using a real field for the analysis or defining a new perturbation with $\varepsilon_{\text{new}} = \varepsilon \cdot e^{-j\theta}$, rewriting the perturbed field as $(r_0 + \varepsilon_{\text{new}})e^{j\theta}$ and then the phase cancels from the equations. The spatial Fourier Transform (FT) of the small signal parameters were defined as $\hat{n}_1 = \int n_1 e^{-j2\pi x} dx$; $\hat{\varepsilon} = \int \varepsilon \cdot e^{-j2\pi x} dx$, and taking the FT of Equation 5.4, the Fourier coefficients of the carrier density fluctuations were found to be

$$\hat{n}_{1(2)} = \frac{f_{1(2)} \cdot r_0 [(a^* + b)\delta(2\pi\nu + p) + (a + b^*)\delta(2\pi\nu - p)]}{D \cdot (-j2\pi\nu)^2 + \gamma_{1(2)}} \quad (5.5)$$

The inverse FT of this equation gives the fluctuations in the carrier density back in space domain as;

$$n_{1(2)} = \frac{f_{1(2)} \cdot r_0 [(a^* + b)e^{-jpx} + (a + b^*)e^{jpx}]}{-D \cdot p^2 + \gamma_{1(2)}} \quad (5.6)$$

The small signal field propagation Equation (5.4a) was rewritten by substituting Equation 5.6 to give;

$$a_z \cdot e^{jpx} + b_z \cdot e^{-jpx} = \frac{j}{2} (-p^2) (a \cdot e^{jpx} + b \cdot e^{-jpx}) + G(p) [(a^* + b)e^{-jpx} + (a + b^*)e^{jpx}] \quad (5.7)$$

It is now possible to rewrite Equation 5.7 in terms of two coupled equations;

$$a_z = \frac{jp^2}{2}a + G(p)(b^* + a) \quad (5.8)$$

$$b_z = \frac{jp^2}{2}b + G(p)(a^* + b)$$

where $G(p) = r_0^2(1-ih)\left(\frac{f_1\bar{N}_1\bar{w}_1}{-Dp^2 + \gamma_1} + \frac{f_2\bar{N}_2\bar{w}_2}{-Dp^2 + \gamma_2}\right)$. Equation 5.8 could be simplified further by

defining $a = a_0.e^{k_z z}$; $b = b_0.e^{k_z z}$; $A' = -jp^2/2 + g(p)(1-ih)$; $B = g(p)(1-ih)$;

$k_z = k_{zR} + jk_{zI}$; $g(p) = r_0^2\left(\frac{f_1\bar{N}_1\bar{w}_1}{-Dp^2 + \gamma_1} + \frac{f_2\bar{N}_2\bar{w}_2}{-Dp^2 + \gamma_2}\right)$ where the real part of k_z ; k_{zR} , specifies the

exponential small signal gain of the perturbation $\varepsilon(x, z) = (a_0 e^{+jpx} + b_0 e^{-jpx})e^{(k_{zR} + jk_{zI})z}$. The result

is

$$a_z = A'.a + B.b^* \quad (5.9)$$

$$b_z = A'.b + B.a^*$$

$$(k_{zR} + jk_{zI} - A').a_0 = \frac{|B|^2 a_0}{(k_{zR} + jk_{zI} - A'^*)} \quad (5.10)$$

Equation 5.10 has solutions only when the real and imaginary parts of the left and right side of the equation are equal to each other. For the real part;

$$k_{zR}^2 - k_{zI}^2 - 2\text{Re}\{A'\}k_{zR} + \text{Re}\{A'\}^2 + \text{Im}\{A'\}^2 = |B|^2 \quad (5.11)$$

$$k_{zR}^2 - k_{zI}^2 - 2gk_{zR} + p^4/4 + p^2hg = 0 \quad (5.12)$$

and for the imaginary part;

$$k_{zI}(k_{zR} - g) = 0 \quad (5.13)$$

When $k_{zI} = 0$, there is no phase oscillation on the small signal field and it is only exponentially growing (or attenuating, depending on the sign of k_{zR}). In this case, the resulting gains of the small signal coefficients for $k_{zI} = 0$ are;

$$k_{zR} = g \pm \sqrt{g^2 - \left(\frac{p^4}{4} + p^2hg\right)}, \quad (5.14)$$

Another solution from Equation 5.13 sets the gain of the small signal coefficient to $k_{zR} = g$, and the phase oscillations are dependent on k_{zI} ;

$$k_{zI} = \pm \sqrt{-g^2 + p^2hg + p^4/4} \quad (5.15)$$

Modulation instability follows from the maximum gain from these solutions.

The three possible solutions for the MI gain k_{zR} are plotted in Figure 5.1 and the gain is positive only for $k_{zR} = g - \sqrt{g^2 - \left(\frac{p^4}{4} + p^2hg\right)}$. Therefore this represents the modulation instability gain coefficient.

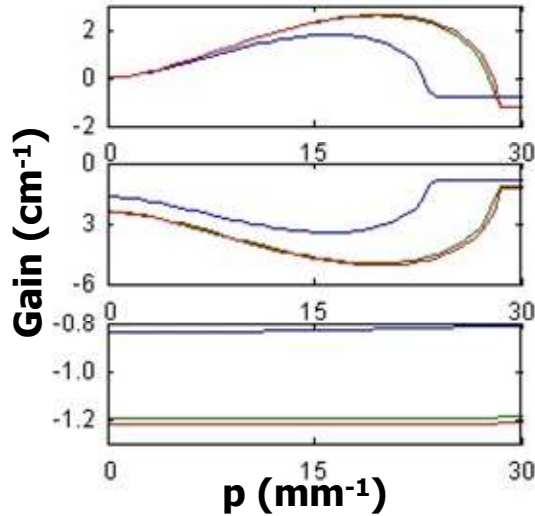


Figure 5.1 Solutions for the modulational instability gain, k_{zR} , versus spatial frequency “p” of the perturbations: top plot for the case $k_{zR} = g - \sqrt{g^2 - (\frac{p^4}{4} + p^2hg)}$; the middle for $k_{zR} = g + \sqrt{g^2 - (\frac{p^4}{4} + p^2hg)}$; and the bottom for $k_{zR} = g$.

This solution was verified by using the BPM code. The input beam was assumed to be a plane wave with sinusoidal perturbations of the form discussed in Equation 5.2. This led to the growth of the seeded spatial frequencies following the gain as indicated in Figure 5.2. The modulation gain is found by taking the FT at each propagation step and calculating the change of spectral intensity at the input perturbation frequencies. The right-hand-side picture shows the formation of filaments with propagation distance. Initially the input perturbation spatial frequency content sees a lower gain. The reason for this could be the fact that even though an input plane wave intensity that is calculated from the bifurcation diagrams is seeded, in order to

reach the actual homogenous solution the beam has to propagate for some short distance. However Figure 5.2 shows a very good fit between the results from Equation 5.15 (dashed lines) and the numerical simulations (solid lines) for longer propagation distances. As the propagation length is increased, the linearized equations no longer give a good agreement with the simulations. The oscillations occur in the numerical gain (solid line generated by the BPM simulations), since the small signal analysis does not hold for such large amplitude modulation.

Figure 5.3 shows the dependence of the modulation gain on the spatial modulation frequency. These curves are very similar in shape to those obtained for both cubic [5.1] and quadratic nonlinearities [5.11, 5.12]. Note that the peak of the modulation gain coefficient curve has a saturating behavior when the current density is increased. Therefore increasing the current density to very high levels does not decrease the perturbation period continuously. However the linewidth enhancement factor is very effective in changing the peak gain and its position. The larger the h is, the smaller the period of the filament perturbations that can grow. This could be an important indication of an operating regime for achieving smaller beam waist solitons by changing the wavelength of the input beam, an interesting question which should be pursued in further work.

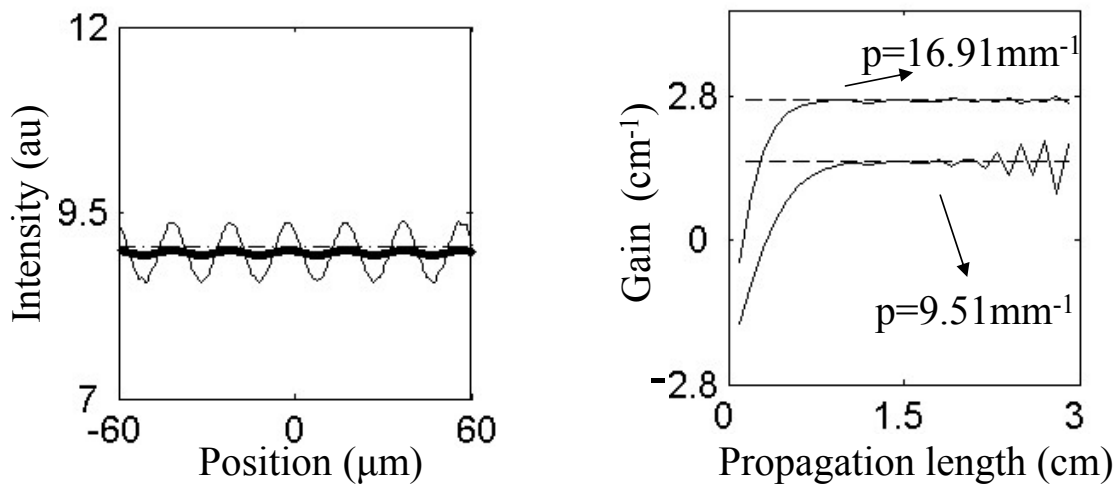


Figure 5.2 (Left) The growth of the transverse sinusoidal perturbations at a current pumping level of $\pi=50$ ($h=3$), with increases in the propagation distance of 1cm between the curves. (Right) The gain coefficient at 2 different spatial modulation frequencies. The dashed line shows the gain from Equation 5.15 and solid line is the result from BPM simulations.

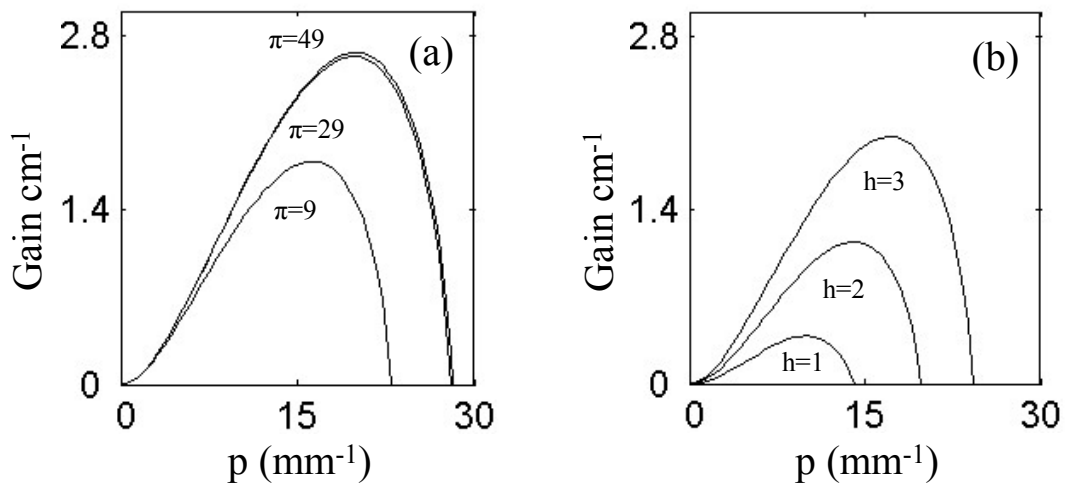


Figure 5.3 (a) Modulation gain vs spatial modulation frequency at $h=3$, for different current pumping levels. (b) For a pumping level of $\pi=9.4$, the change in the gain curves with linewidth enhancement factor h .

5.3 Discussion of Experimental Possibilities

Although the MI analysis presented here is strictly valid only for the small signal growth regime for periodic modulation of a plane wave background, it is also possible to observe MI behavior for broad (relative to a spatial soliton of the same peak intensity) Gaussian beams through periodic modulation seeding. The possibility of observing experimentally MI in broad area PPSOA devices, using a two beam interaction technique was also analysed numerically. In the simulations a $240\mu\text{m}$ waist, 300mW peak power Gaussian pump beam and a 10mW input power weak probe beam that has the same Gaussian profile were assumed to propagate at a small relative angle. These two beams were overlapped at the input of the sample in order to generate a periodic modulation of the pump beam (see Figure 5.4). This seeding technique is very useful for short sample lengths where the net growth from small noise may not be experimentally measurable. The spatial frequency of the modulations can be changed by tuning the angle of interaction.

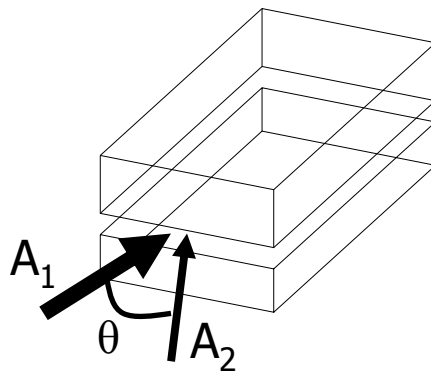


Figure 5.4 The configuration of two beams used at the input of the sample to generate MI seeding.

Beam propagation simulations were used to analyze the effects of seeding. Although the MI analysis given by Equation 5.15 is applicable in any current regime, because of the spontaneous emission in the devices, it is necessary to analyze the system around the low current regime. Figure 5.5 shows the simulations for pumping current density $\pi=9.4$, and $h=3$ (max MI gain frequency for these parameters is 16.91mm^{-1}), and seeding frequency of 31.55mm^{-1} . By taking the FT of the profiles during propagation one can investigate the MI effects in specific parts of the spatial frequency domain.

Since MI is a small signal analysis, it may not be applicable for all propagation distances. This has already been demonstrated in Figure 5.2. When the seeding is not a plane wave, the beam evolution is much more complex so that the observation and quantitative analysis of MI gain depends on the beam profiles, intensities, and the propagation distance. In Figure 5.6 was plotted the propagation behavior of a Gaussian beam with superimposed periodic modulation. The modulation gain was defined as; $S_{output}(z, f) / S_{input}(0, f)$, where S is the intensity spectral content of the beam profile which is a function of propagation distance and frequency f . The figure shows that maximum gain at all frequencies occurs around 1.2cm propagation distance and the peak gain frequency at this propagation distance is $\sim 17\text{mm}^{-1}$. The gain profile has some resemblance to Figure 5.3 in which a sharp decrease in gain is observed at higher frequencies. The propagation in excess of 1.5cm starts to create interactions between the MI filaments making the current MI analysis no longer applicable.

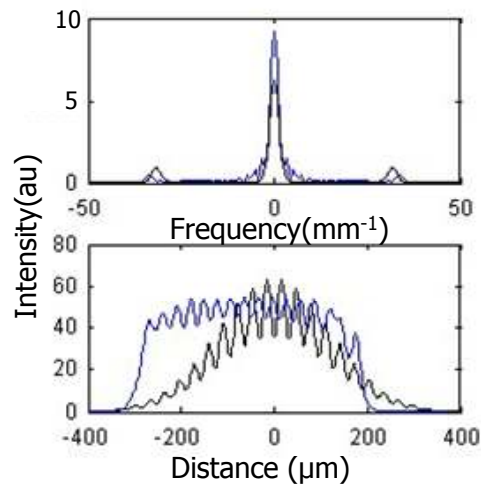


Figure 5.5 Top figure shows the intensity spectrum of the simulations. The bottom figure gives the intensity profile at the input (black line) and the intensity profile after 1cm propagation (blue line).

The modulation gain with distance changes significantly with the probe power. Figure 5.7 shows that when the probe power is decreased to 0.4mW, the required propagation distance for MI observation is about 2cm. Therefore probe input power could also be used as a control parameter in the MI observation, since the sample length is usually constant during this kind of experiment.

Although numerical simulations shows that it is possible to observe the MI effects by carefully choosing the input parameters, it is still important to remember the effects of sample defects on the beam profile (Chapter 3). These defects might be a problem for MI formation, and operability of MI analysis for broad input beams.

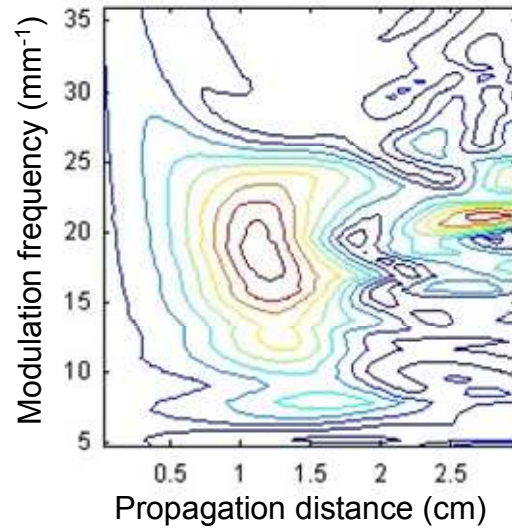


Figure 5.6 Contour plot of the modulation gain with propagation distance for a 8mW probe beam.

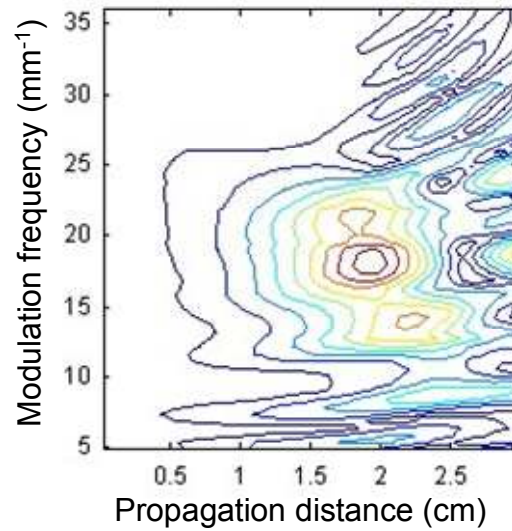


Figure 5.7 Contour plot of the modulation gain with propagation distance for a 0.4mW probe beam

5.4 Conclusions

MI of PPSOA devices was investigated analytically. The maximum MI gain was observed around 17mm^{-1} for the parameters that were used in the observation of solitons. This spatial frequency led to a $58\mu\text{m}$ spatial filamentation period. The spatial soliton full width at half maximum was calculated to be around $20\mu\text{m}$ at the same current density. Assuming that each filament could evolve into a spatial soliton, the half period of the filaments is very similar to spatial soliton waist. This is a consequence of the relation between the MI and the solitons. Finally the MI analytical results could be very useful in evaluating the spatial soliton profile vs system parameters, since the soliton profile can not be calculated analytically in the PPSOA system.

CHAPTER SIX: DISSIPATIVE DISCRETE SOLITONS

“Einstein explained his theory to me every day, and on my arrival I was fully convinced that he understood it”

Chaim Weizmann

6.1 Introduction

Photonic lattices have been at the focus of optics recently as a way to mold light into discrete states. Periodic modulations in index make an environment for optical waves analogous to that experienced by electrons traveling in a semiconductor crystal. Photons take on periodic wave patterns (or Floquet-Bloch modes), which are similar to electron wave functions in crystals. The resemblance comes from the fact that the crystals are also periodic structures of atoms. When atoms in a crystal come close to each other, they form periodic potential wells that have discrete energy states, and the electrons location is described by periodic probability functions. In optics, equivalent potential wells could be formed by refractive index distributions.

The first application of molding light periodically in optics was via Bragg gratings. Bragg gratings use the interference of light resulting from reflections from many periodical structures (ideally infinite), and depending on the periodicity vs the optical wavelength, the amount of light transmitted (or reflected) could be controlled. Later arrays of evanescently coupled waveguides were realized as a way of changing the properties of diffraction in bulk media [6.1, 6.2]. Most

recently photonic crystals which use the same effect as Bragg gratings have been investigated in both 3 dimensions [6.3] and 2 dimensions [6.4].

One dimensional arrays and photonic crystals can both exhibit photonic bandgaps which stop the transmission of light, or at least change its dispersion characteristics. In order to see the similarity, one can study electromagnetic waves propagating in the xy plane in a photonic crystal consisting of optical rods with a periodic dielectric constant $\varepsilon(r)$ defined along the z axis [6.5].

For the TM polarization (E-field parallel to the rods, i.e. $\vec{E}(r) \equiv (0,0,E(\vec{r}))$), one obtains from Maxwell's equations the wave equation

$$\left(\frac{\partial^2}{\partial x^2} + \frac{\partial^2}{\partial y^2}\right)E(\vec{r}) + \frac{\omega^2 \varepsilon(\vec{r})}{c^2} E(\vec{r}) = 0. \quad (6.1)$$

According to the Floquet-Bloch theorem, the periodic solutions of Equation 6.1 have to obey the relationship

$$E_{\vec{k}}(\vec{r} + \vec{a}_i) = e^{j\vec{k}\vec{a}_i} E_{\vec{k}}(\vec{r}) \quad (6.2)$$

where $i=1,2$. The wave vector \vec{k} belongs to the first Brillouin zone and is known as the crystal momentum. If in the discrete array case the lattice period is much larger than the wavelength and for a beam which is propagating parallel to the lattice, the propagation equation for electric field in the normalized form (see chapter 2 for normalizations) can be written as

$$\psi(x, z) = \frac{j}{2} \psi_{xx}(x, z) + jk_0 \Delta n(x) \psi(x, z) / L \quad (6.3)$$

Here k_0 is the propagation vector of the electric field in vacuum and $\Delta n(x)$ is the refractive index change which defines the waveguides in the array.

These equations have “plane” wave solutions for discrete arrays. They are of the form

$$\psi(x, z) = \psi(x) e^{j\lambda_{FB}z}, \quad (6.4)$$

$$j\lambda_{FB}\psi(x) = \frac{j}{2}\psi_{xx}(x) + jU(x)\psi(x). \quad (6.5)$$

Here the propagation wavevector (k) in the z direction is modified by the effect of the array as $k + L^* \lambda_{FB}$ (L is the normalization constant from chapter 2) and $U(x) = \Delta n(x)k_0 / L$. The periodic solutions of this array could be found using the Floquet-Bloch (FB) theorem which defines $\psi(x + \Lambda) = \psi(x) e^{jk_x \cdot \Lambda}$, where Λ is the period of the array. This equation is similar to Equation 6.2 in one dimension. Using the FB theorem it is possible to rewrite the field equation as $\psi(x) = \psi_{k_x}(x) e^{jk_x \cdot x}$, the function $\psi_{k_x}(x)$ is the FB function and is only defined over $[-\Lambda/2, \Lambda/2]$. In the Fourier domain, equation 6.5 could be rewritten in terms of FB functions as

$$\lambda_{FB} \Psi_{k_x}(v) = \frac{1}{2}(-k_x^2 + k_x v + \frac{v^2}{2}) \Psi_{k_x}(v) + \bar{U}(v) \otimes \Psi_{k_x}(v). \quad (6.6)$$

Here the Fourier transforms are defined by $\Psi_{k_x}(v) = \int \psi(x) e^{-jvx} dx$, $\bar{U}(v) = \int U(x) e^{-jvx} dv$, and \otimes is the convolution function. Equation 6.6 can be solved as an eigenvalue problem for each k_x .

Using this expansion technique the FB bands have been calculated and $\psi(x) = \psi_{k_x}(x) e^{jk_x \cdot x}$ for different values of k_x . The array used in these calculations had ridge waveguides with widths of $2.5\mu\text{m}$ (w_2) and the separation between the waveguides was $3.0\mu\text{m}$ (w_1) (see Figure 6.1). The refractive index difference between the ridge and the underlying slab region was 1.5×10^{-3} . The

coupling coefficient for this waveguide array at 980nm was 9.48cm^{-1} , and coupling length was 1.65mm (the refractive index for the slab was assumed to be 3.31).

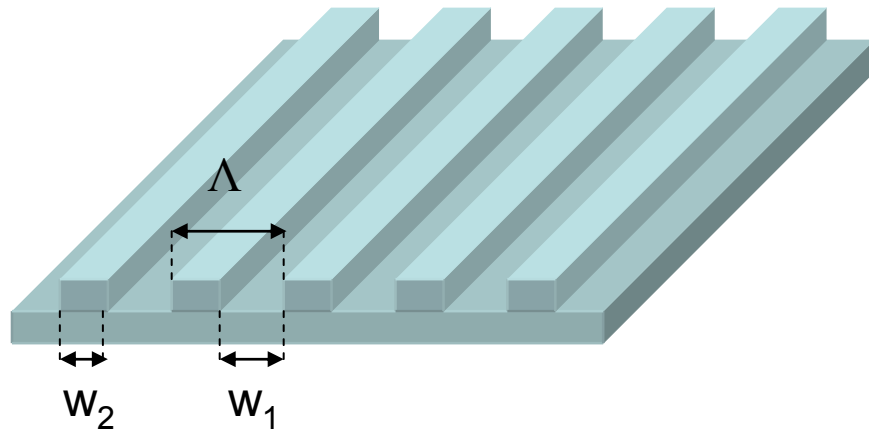


Figure 6.1 Ridge waveguide array with a period Λ

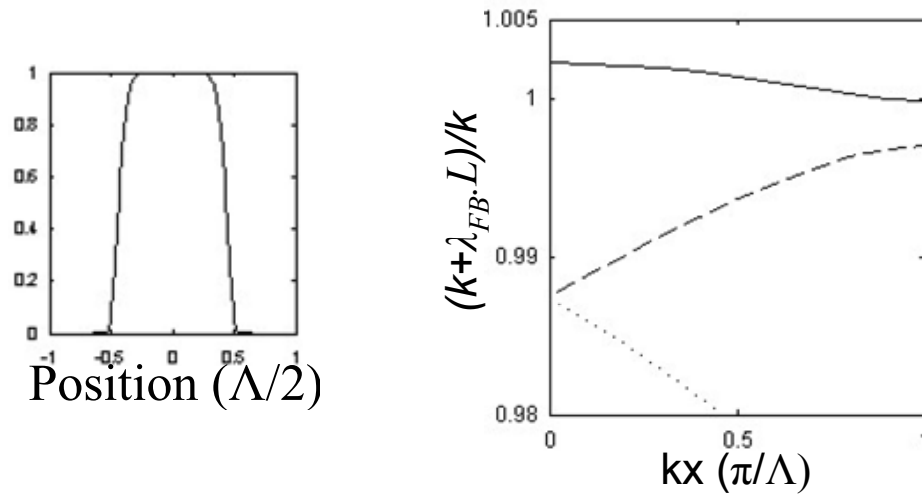


Figure 6.2 The FB band diagram for a waveguide array with $w_1=3\mu\text{m}$, $w_2=2.5\mu\text{m}$ and $\Delta n = 1.5 \times 10^{-3}$. Left: The index distribution in one lattice period with exponentially decaying tails assumed at the ridge edges which are similar to the experimental conditions. Right: The dispersion relation of FB bands with transverse k -vector (k_x).

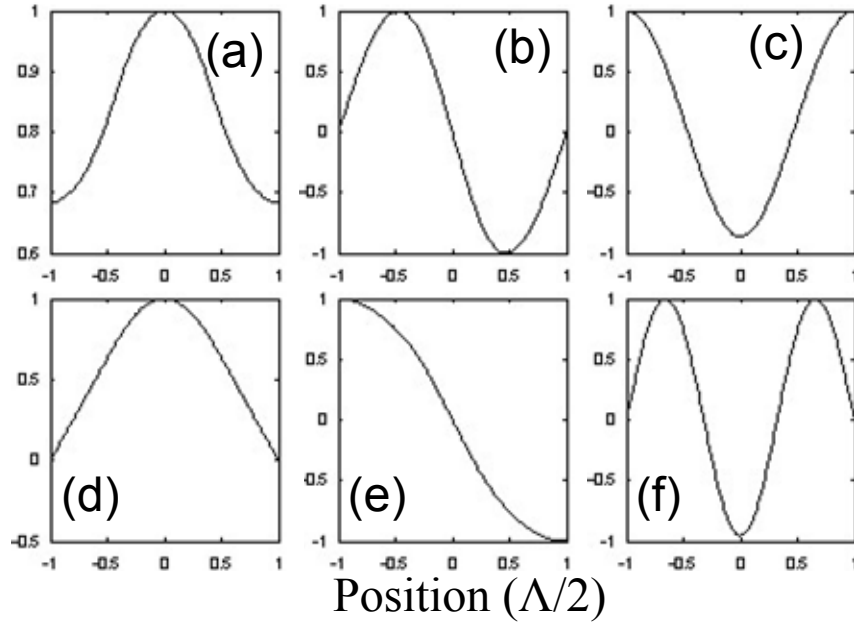


Figure 6.3 The FB wave field profiles in the first three bands at $k_x=0$ (a, b, c) and $k_x=\pi$ (d, e, f).

In the linear regime, wave propagation in the arrays is subject to the periodic potential which is formed by the refractive index distribution, and as a result the dispersion relation (Figure 6.2). The dispersion relation exhibited both allowed bands and bandgaps. Periodic waves were only allowed to travel if their propagation eigenvalues $k+L*\lambda_{FB}$ fell in the allowed band, while the wave functions with propagation constant in the bandgaps decayed exponentially in the transverse direction.

In Figure 6.3, the wave functions $\psi(x) = \psi_{k_x}(x)e^{jk_x \cdot x}$ are plotted. In the first band the beam profile has a peak in the ridge (a, d) where-as in the higher order bands multiple peaks and

zeros occur within the ridge. It is interesting to note that the first optical observation of FB wavefunctions was experimentally achieved using arrays only quite recently [6.6].

The addition of nonlinearity changes the propagation properties of linear lattices, and the normal modes of any nonlinear lattice system are called discrete solitons [6.7]. These self-localized states can exist when the on-site nonlinearity exactly balances the effects of discrete diffraction/dispersion arising from linear coupling among adjacent waveguides/cavities. Thus far, discrete solitons have been experimentally observed in Kerr AlGaAs [6.8], quadratic waveguide arrays [6.9] and in optically induced photorefractive lattices [6.10]. Quite recently, dissipative solitons have been successfully observed in cavities [6.11] and semiconductor optical amplifier systems [6.12]. This latter soliton family is possible in dissipative systems exhibiting intensity dependent gain and loss in addition to an optical nonlinearity in the refractive index. Given the wealth of possible processes in discrete systems [6.13], the question arose as to whether discrete solitons exist in dissipative lattices.

Discrete dissipative solitons were recently examined for general models, specifically the discrete Ginzburg-Landau model [6.14, 6.15], and nonlinear optical cavities [6.16]. Moreover in a recent study the possibility of observing similar localized structures in multicore Yb-fiber arrays was also considered [6.17].

Before discussing the detailed investigation of nonlinear dissipative photonic lattices, it is important to note the immense amount of research done in the past by Botez and coworkers on phase-locked semiconductor arrays and its purpose [6.18]. Phase locking is a way of generating a coherent output beam profile from a number of different sources. The main reason for the use of this technique is the uncontrollable filament formation in wide area semiconductor devices

because of thermal and electronic nonlinearities [6.19]. As the device area increases, the gain guiding or index guiding could be affected by the nonlinearities or imperfections, mostly in the central region of the device. Multiple peak-like filaments were seen: Actually it is now known that these were observations of MI in an unstable background system. Therefore increasing the device area is not a good solution for generating high power devices. In the phase locking technique, each waveguide area that forms the array is small enough so that semiconductor nonlinearities do not change the beam profile in the waveguide. The coherence between the waveguides is achieved by coupling through the tails of the modes. When the gain and index guiding regions occur in the same region, semiconductor devices prefer to operate in an out-of-phase mode. The reason this occurs is because the in-phase-mode (the output of all waveguides have the phase profile, the corresponding FB mode is Figure 6.3a) has higher losses since the fields are non-zero in the overlap region of the evanescent tails, i.e. in the w_1 region, whereas the out-of-phase ($k_x = \pi$) mode crosses zero intensity level between the waveguides and thus experiences lower net loss. Following this result, it was found that if the gain regions were put between the waveguide regions, leaky coupling gave stable in-phase-modes. These leaky modes, as calculated in Figure 6.3, are not in the first band but in the higher bands. Since the uniform gain semiconductor amplifier system is unstable for soliton generation [6.20], up to now there has not been any investigation of stable solitons-like waves in semiconductor arrays.

This chapter deals with theoretical predictions of optical discrete solitons in dissipative arrays or lattices. These dissipative lattices can be implemented by utilizing periodically patterned semiconductor optical amplifiers and absorbers. It is shown that unlike their continuous counterparts [6.12, 6.20], this new class of solitons exhibits several interesting

characteristics because of discreteness. For instance, *these new solutions no longer belong to a zero parameter family* and their nature depends on their Floquet-Bloch band structure. The prospect of observing such low power dissipative lattice solitons is discussed next in terms of pertinent examples.

6.2 Discrete Dissipative Solitons

Figure 6.4 shows a proposed discrete device where such dissipative lattice solitons should be observable. As defined previously, w_2 is the width of the ridge waveguides and w_1 is the distance between the ridges. The periodic contact patterning is done only over the ridge waveguides and between the ridges the device behaves like a saturable absorber. This kind of a structure can be easily fabricated using chemical etching and contact deposition techniques. Note that unlike previous laser array designs [6.18], what is proposed here is a sequence of saturable absorbers (SA) and semiconductor optical amplifiers (SOAs) (along the propagation coordinate z) that is known to significantly alter the propagation dynamics [6.12].

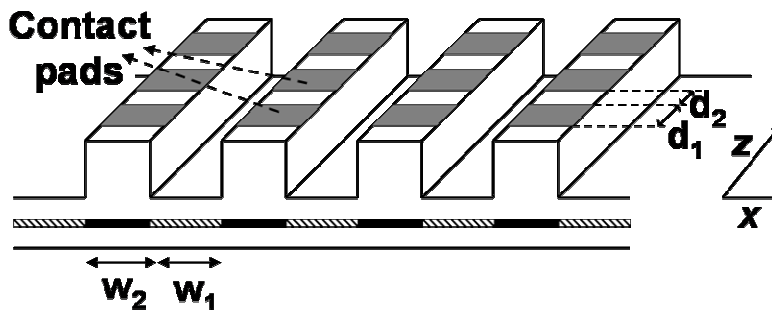


Figure 6.4 Proposed discrete PPSOA array structure

Spatial solitons in a discrete semiconductor array were modeled using two coupled equations for the carrier density (N) and the evolution of the TE polarized optical field (ψ);

$$\psi_z = \frac{j}{2}\psi_{xx} + [\bar{f}(N_1, N_2)(1 - jh) - \alpha]\psi + jU(x)\psi \quad (6.7)$$

$$DN_{1xx} + \pi(x) - BN_1^2 - CN_1^3 - f(N_1)|\psi|^2 = 0 \quad (6.8)$$

$$DN_{2xx} - BN_2^2 - CN_2^3 - f(N_2)|\psi|^2 = 0 \quad (6.9)$$

where $f(N)$ is the carrier dependent gain and for the quantum well device suggested here a logarithmic gain dependence is assumed, i.e., $f(N_{1(2)}) = \ln\left(\frac{N_{1(2)}N_{tr} + N_s}{N_{tr} + N_s}\right)$ with N_s being a fitting constant. In Equation (6.7), $\bar{f}(N_1, N_2) = [f(N_1)d_1 + f(N_2)d_2]/(d_1 + d_2)$ is an average gain in z , and $d_{1,2}$ represent the length (in z) of the pumped and un-pumped regions respectively. In these equations, h is the linewidth enhancement (Henry's factor) and $\pi(x)$ represents the normalized current density or pumping ($\pi(x) = \pi_0$ on the ridge, at the contact sites and 0 for absorber sections-where no contacts exist, for the parameters see Chapter 3 and reference [6.21]). The discreteness in the system arises from the array index modulation function $U(x) = k_0\Delta n(x)$ and from the periodic pumping coefficient $\pi(x)$. The index modulation $\Delta n(x)$ exhibits a maximum index contrast Δn between the ridges and the etched layers.

In this system, for a given set of parameters (π_0 , Δn , w_1 and w_2) lattice solitons can be identified using a relaxation code (as explained in Chapter 3) and by assuming $\psi(x, z) = |\psi(x)|e^{i(\lambda z + \theta(x))}$, where $|\psi(x)|^2$, $\theta(x)$, λ are the soliton intensity profile, and the

complex phase and propagation constant eigenvalues respectively. Figure 6.5 shows the calculated soliton intensity and phase profile for $w_1=3\mu\text{m}$, $w_2=2.5\mu\text{m}$, $\Delta n = 1.5 \times 10^{-3}$, at $\pi_0=20$ (corresponding to $J = 564A/cm^2$). In this example, the total power of the discrete soliton was $35 mW$ and the field exhibited a chirped phase around its tails in a way similar to that encountered in the continuous regime [6.20]. Moreover, in contrast to the discrete solitons previously identified in conservative systems, these solitons had a complex-discrete phase behavior around their peak (Figure 6.5(b) inset). An important parameter associated with the power flow within these dissipative solitons is the phase difference $k_x\Lambda = \theta((m+1)\Lambda) - \theta(m\Lambda)$ between successive lattice sites. Here $\Lambda=w_1+w_2$ is the spatial period of this array and m is the waveguide number. The phase difference parameter corresponding to the lattice soliton of Figure 6.5(a) is found to approach the asymptotic limit (~ 0.7) in the soliton tails as shown in Figure 6.5(c). Note that for a “cold” array (without any carrier effects, ie. $\bar{f}(N_1, N_2) \approx 0$), k_x corresponds to the Floquet-Bloch (FB) mode wavenumber or lattice momentum [6.22, 6.23], and the FB modes assume the form $\psi_{k_x}(x)e^{i(\lambda z + k_x x)}$ where $\psi_{k_x}(x)$ is a periodic function with the lattice period (Λ). In addition the low intensity tails of these solitons fitted well the linear FB modes since the nonlinear effects (gain+nonlinear index change) which disturb the cold lattice are absent in these regions.

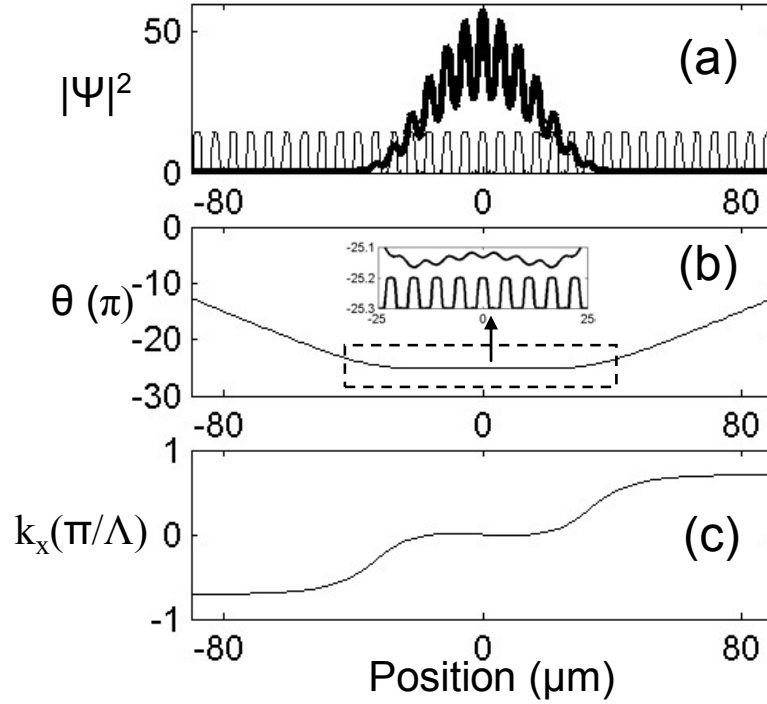


Figure 6.5 Dissipative lattice soliton (a) field intensity (b) phase (c) discrete phase difference k_x versus transverse distance x in the array. The inset in Figure 6.5(b) depicts an enlargement of the phase structure around the soliton intensity peaks shown in Figure 6.5(b).

Figure 6.6(a) shows the normalized propagation constant $k_{sol}/(k_0 n_{eff}) = 1 + \lambda/(k_0 n_{eff})$ associated with the family of dissipative discrete solitons, modeled according to Figure 6.5. In the latter expression n_{eff} is the index of the etched region. The shaded areas in this graph represent the first two FB bands of the periodic structure within the first Brillouin zone. The lattice soliton propagation constant is plotted here against the pumping parameter π from 0 to 120 ($J=3.38kA/cm^2$). In this case, the eigenvalues of all the solitons belonging to this family lie at the upper edge of the first FB band where $\lambda/k_{neff}>0$. Note that

unlike passive discrete solitons where the eigenvalue appears within the semi-infinite band gap, here the eigenvalue enters the band because of dissipative effects. Just as in the continuous case [6.12] the discrete soliton peak-intensity diagram (Figure 6.6 (b)) exhibits a subcritical bifurcation. The soliton branch with negative slope is unstable. The stability of the solitons corresponding to the positive slope branch is then analyzed using beam propagation methods (BPM with random numerical noise superimposed on the soliton solutions). It turns out that these solitons are stable in the region after the turning point of the bifurcation curve (from negative slope to positive slope). However as the current increases the lattice solitons start to become unstable. This behavior is to some extent reminiscent of the continuous case [6.20]. The eigenvalue “loop” on which this family exists is shown in Figure 6.6(a) where its upper branch corresponds to the positive-slope part of the bifurcation diagram Figure 6.6(b). Figure 6.6(c) depicts propagation simulations of both stable and unstable dissipative lattice solitons corresponding to different points on the bifurcation diagram.

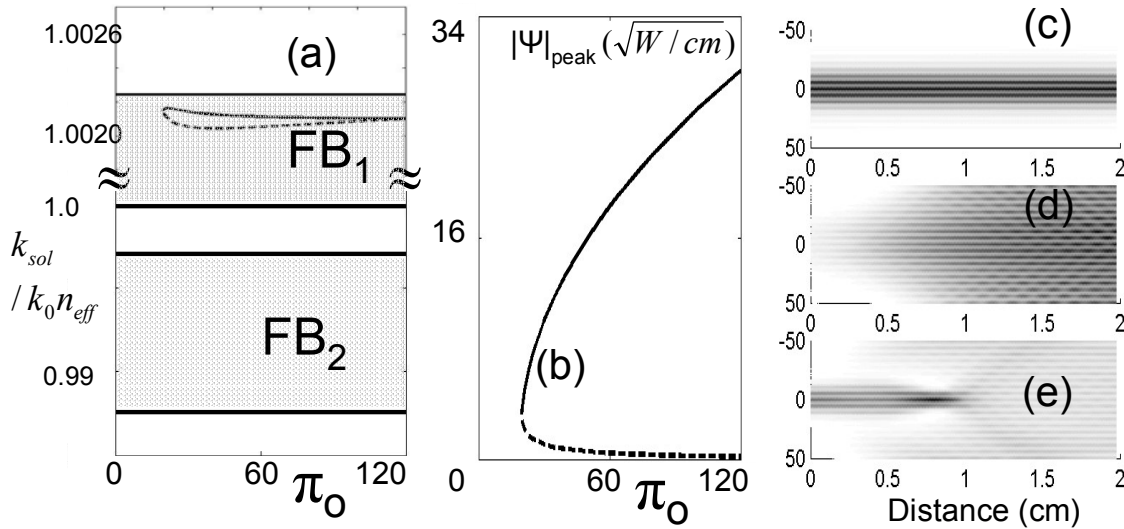


Figure 6.6 (a) Normalized soliton propagation constant as a function of pumping. The soliton existence loop lies within the first FB band. (b) Discrete soliton bifurcation diagram. Solid line represents the positive slope-branch whereas the dashed line identifies the unstable negative slope branch. BPM simulations for a soliton (c) on the stable branch at $\pi_0=25$, (d) on the unstable branch at $\pi_0=25$ and (e) on the stable branch at $\pi_0=40$.

As discussed in the previous chapters, stable dissipative solitons in continuous PPSOA systems belong to a zero parameter family [6.12, 6.20]. However in the discrete case, the discrete soliton states (for the same pumping and system parameters) exhibit multi-hump behavior that would have been otherwise impossible in the continuous regime. In other words, discreteness breaks the zero parameter property. These localized states can propagate undistorted in spite of their multi-peak structure as shown in (Figures 6.7a,c,e). Hence the discreteness of the system prevents any internal interactions between the humps and as a result these multi-hump solitons [6.24] can propagate in a stable fashion. The far-field profiles of these modes are important, since there could be a possibility to use such solitons from a discrete array amplifier

as a coherent phase-locked source [6.18]. Figures 6.7 (b,d,f) show that all these modes are in-phase and therefore their Fourier transform has a peak at the center (zero spatial frequency). Moreover as the number of intensity peaks within these lattice solitons increases the central peak in the spatial frequency domain becomes sharper and increases its amplitude compared to its sidelobes. This latter property is of course desirable for an array amplifier. The far-field side peaks at spatial frequency; $f=\pm 1/\Lambda$ arise from the array discreteness whereas the sidelobes clustered around the sharp central peak are caused by the soliton's multi-hump structure. All these modes were found to be stable using BPM analysis.

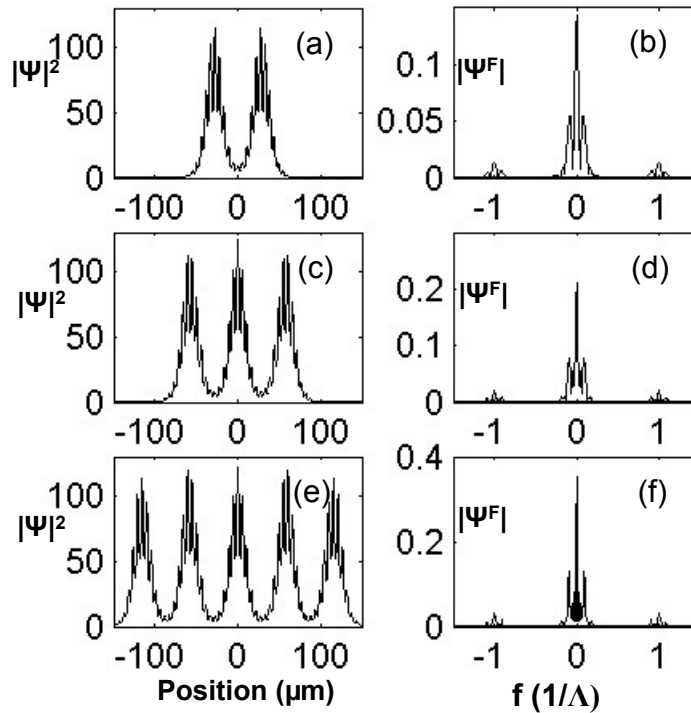


Figure 6.7 Bound lattice soliton intensity profiles ($\sqrt{W/cm}$) for $w_1=3\mu\text{m}$, $w_2=2.5\mu\text{m}$, $\Delta n = 1.5 \times 10^{-3}$, $\pi=25$ (a-c-e). Figures (b-d-f) show the Fourier spectrum or far-field pattern of the soliton modes corresponding to (a-c-e) respectively.

6.3 Conclusions

In conclusion, a discrete PPSOA array structure was analysed in order to facilitate the future observation of discrete dissipative spatial solitons. Such experiments are currently underway. The properties of these solitons were considered by mapping the soliton propagation eigenvalues onto the FB band diagrams. It was shown that the discreteness in the system breaks the zero-parameter property associated with dissipative solitons in continuous systems. These bound discrete amplifier solitons could have potential applications in solid state laser pumping schemes.

CHAPTER SEVEN: INCOHERENT INTERACTIONS

“A theory is something nobody believes, except the person who made it. An experiment is something everybody believes, except the person who made it”

Albert Einstein

7.1 Introduction

Solitons are typically formed by *coherent* beams as a balance of nonlinearity and diffraction. However in systems where the nonlinearity does not couple energy between two beams, or the response time of the nonlinearity is slow compared to the characteristic time for random phase fluctuations across a beam, *incoherent* interactions could take place. In reality there is no instantaneous nonlinearity. In contrast, the electronic nonlinearities which require multiple photon interactions (Kerr [7.1, 7.2] and quadratic [7.3] systems) are so fast that (<100fs) that it is very difficult to generate rapid random spatial fluctuations on the beams that are faster than the nonlinearity response time in these systems. In the case of incoherent solitons which have been observed in photorefractive media and liquid crystals, the nonlinearity affects the spatially random beam in a time-average fashion, and thus the propagating beam does not form into independent speckles. It was shown that the collisions between incoherent multi-component solitons can lead to the exchange of energy between the individual components associated with each soliton, but not to an energy exchange between solitons [7.4], a function that is potentially useful for optical computing.

Semiconductor resonant nonlinearities are not as fast as multi-photon effects. However the response time could be on the order of hundreds of picoseconds. This is still too rapid for present commercially available spatial diffusers. On the other hand, the semiconductor resonant nonlinearity has a wide spectral response for the gain and refractive index distribution due to the Kramers-Kronig relationship (see Chapter 2). Thus it should be possible to observe multicolor interactions of an incoherent nature in semiconductor devices. Multicolor solitons have been calculated previously for pulse propagation in optical fibers [7.5], beam propagation in slab waveguides [7.6] for Kerr media.

It is conjectured that the effect of such a two color nonlinearity on solitons should be vector-like [7.5, 7.6]. Vector systems have been previously introduced for Kerr AlGaAs media, through the interaction of TE and TM optical fields [7.1, 7.2]. Semiconductor devices usually supply the most gain for TE polarization, as a result of the quantum well properties (because of stress/strain during growth, one polarization experiences more gain than the other one). Actually the effects on TM polarization of the device nonlinearities are almost negligible. In any case, before going into the complex dissipative models, it is helpful to use the polarization coupled system (Kerr nonlinearity, non-dissipative system) in order to obtain insight into soliton behavior for *coupled soliton equations* in PPSOAs.

The vector coupled nonlinear Schroedinger equations in general for two mutually incoherent beams, fields u and v , could be written as;

$$iu_z + \alpha u_{xx} + (|u|^2 + \gamma |v|^2)u = 0 \quad (7.1a)$$

$$iv_z + \nu v_{xx} + (|v|^2 + \gamma |u|^2)v = 0 \quad (7.1b)$$

Equations 7.1 model a coupled nonlinear Schroedinger equation system, where α is the ratio of propagation vectors (k_v/k_u) used to describe diffraction, and γ is the ratio of cross-phase-modulation (XPM) to self-phase-modulation. The main effects of a difference in the beam carrier frequencies will be in the propagation vectors and also the nonlinearity. In this general form Equation 7.1 supports coupled soliton solutions for different α , as shown in Figure 7.1

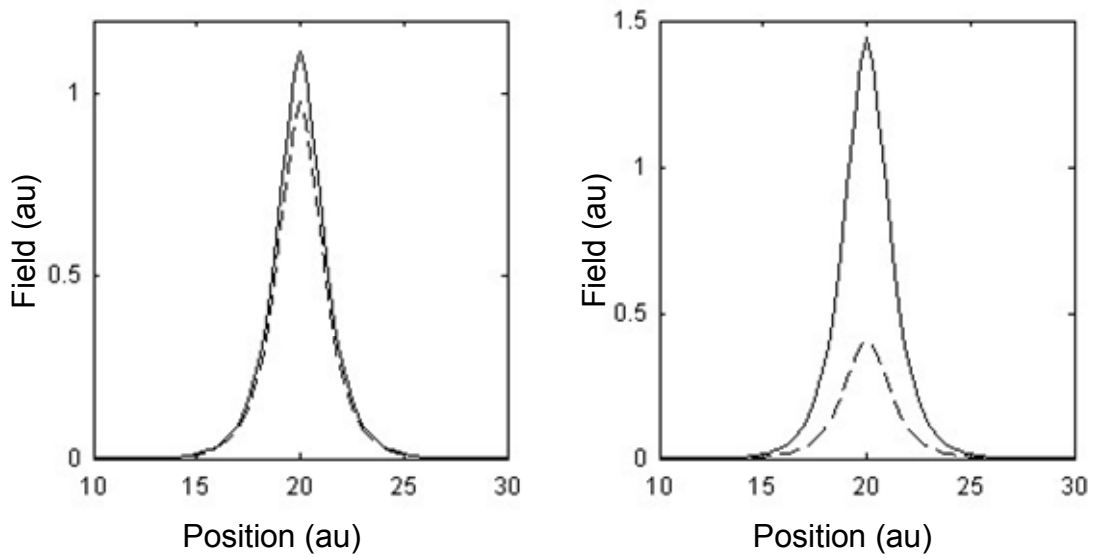


Figure 7.1 The soliton profiles found by relaxation simulations for a coupled nonlinear Schroedinger equation system given by Equations 7.1. The left figure shows profiles for $\alpha=1.01$ and the right for $\alpha=1.1$. The dashed line is u , and the solid line is v .

These simulations show that small changes in the diffraction could change the coupled soliton profiles significantly in a coupled nonlinear Schroedinger system. It is also important to remember that the solitons form an infinite family when equations are completely symmetric ($\alpha=1$). Solitons also change with the nonlinearity γ . Since this nonlinear property is not

dissipative, the dispersion in nonlinearity for small frequency changes is not very important. For comparison to the results for vector systems without gain, it is interesting to analyze if coupled dissipative solitons exist. If they do exist, under which conditions are these systems stable?

In addition to the fundamental properties of dissipative coupled solitons, there are also important questions about the interaction between two incoherent dissipative solitons. In Chapter 4 the interactions between two coherent beams were analyzed. The interactions were very strong because of the coherent coupling-or interference effects. Although coherent interactions could lead to several interesting soliton applications, in reality most of the all-optical logic gates will require incoherent beam interactions. This comes from the fact that multiple, mutually incoherent sources have to be used in order to supply the necessary bandwidth, and power for high data rate WDM traffic in networks. Therefore all-optical operations with different source inputs are very important.

7.2 Incoherent Interactions in Gain Systems

The existence of propagating dissipative solitons in periodically patterned semiconductor optical amplifiers (PPSOAs) at 10's mW power levels were discussed in Chapters 2 and 3 [7.7]. Due to their low power levels and zero parameter property, dissipative solitons could offer a very attractive option for collisions between incoherent solitons consisting of different frequency components for applications to mathematical operations and/or logic gates. Furthermore it should be possible to separate the outputs of these devices using a grating, which could improve the

problems of cross talk in predefined exit ports known to occur for coherent interactions [7.8, 7.9].

For active-dissipative systems, numerical simulations have shown the existence of stable solitons for the linearly coupled cubic Ginzburg-Landau equations with gain and dissipation in one subsystem and pure dissipation in the other one [7.10]. However to the best of our knowledge this is the first analysis of a coupled dissipative system where both gain and loss are applied at the same time to beams at different wavelengths, the case of PPSOAs. The existence and stability of multi-frequency soliton bound states is investigated experimentally and theoretically in this chapter.

The samples in which the first dissipative solitons (see Chapter 3) were reported were also used in these experiments. Two beams from different sources, one from a continuous wave Ti-sapphire (TS) laser (943nm), and another one from a laser diode (LD) at 948nm were coupled into the waveguide. The outputs of these two lasers have been modulated to produce 400ns pulses, overlapped in time, with the pulsed current source by using triggered AO modulators. The two beams incident onto the input waveguide facet had 15 μ m FWHM beam waists in the waveguide plane and were polarized along the waveguide axis. The power coupled into the waveguide from the LD was about 40mW, and the output power from the Ti-sapphire was tuned by using a half wave plate and polarizing beam splitter. The output facet was imaged by a CCD camera while the TS output power was tuned. The case where the two beams were completely overlapped at the input and aligned to propagate straight along the device was investigated. The outputs at the two frequencies were separated by a grating and detected by a CCD array.

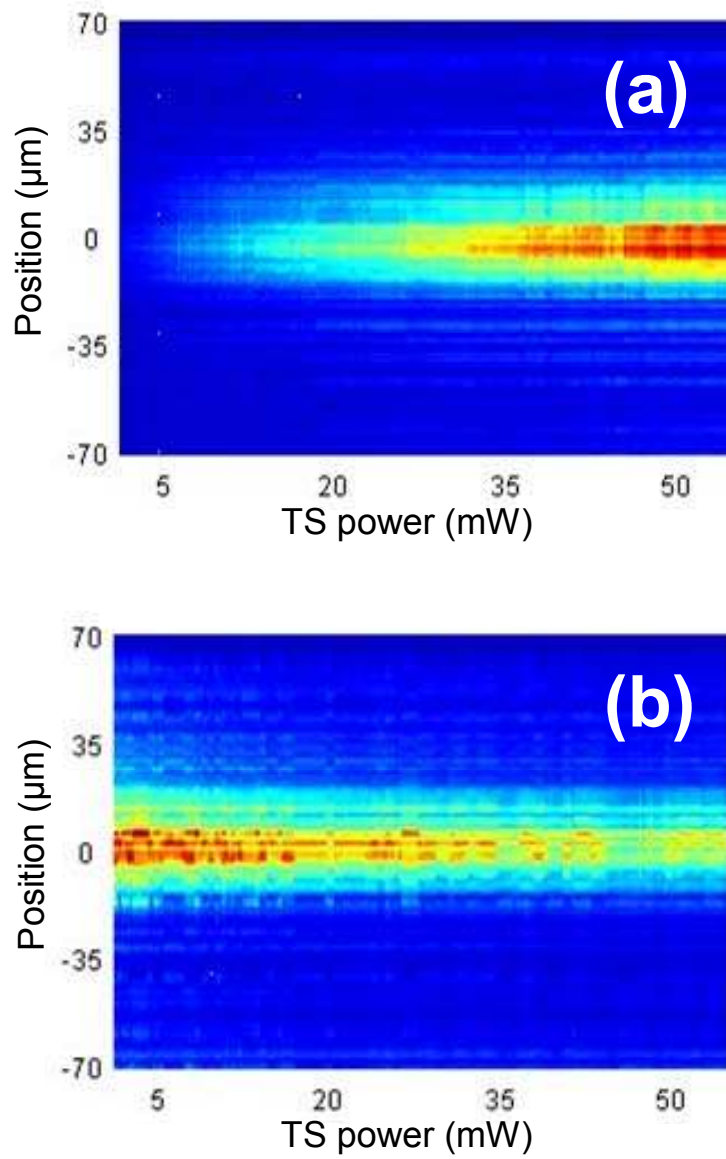


Figure 7.2 The output images for (a) the TS beam and (b) the LD beam obtained while TS power was increased.

Figure 7.2 shows that because the two optical beams share the same carrier population, there is a dissipative interaction between the two laser beams, even though they are mutually incoherent. As the power into the TS component is increased, the gain available for the LD beam decreases. Similarly, the two beams interact through the saturable absorption. There are small power fluctuations in the profiles caused by fluctuations in the peak lasing wavelength of both lasers, which are both smaller than $\pm 0.5\text{nm}$.

In order to understand these results it is necessary to analyze numerically the response of the PPSOA to power changes in the two input beams. The two coupled wave semiconductor modeling equations given below were used.

$$\psi_{1z} = \frac{i}{2}\psi_{1xx} + \psi_1[f(N)(1 - ih_1) - \alpha], \quad (7.2a)$$

$$\psi_{2z} = \frac{i\mu}{2}\psi_{2xx} + \frac{1}{\eta}\psi_2[f(N)(1 - ih_2) - \alpha], \quad (7.2b)$$

$$DN_{1xx} + \pi(z) - BN_1^2 - CN_1^3 - f(N_1)(|\psi_1|^2 + |\psi_2|^2/\eta) = 0, \quad (7.2c)$$

$$DN_{2xx} - BN_2^2 - CN_2^3 - f(N_2)(|\psi_1|^2 + |\psi_2|^2/\eta) = 0, \quad (7.2d)$$

where the subscripts 1 and 2 refer to the parameters associated with the TS and LD sources respectively. Furthermore $\mu = k_1/k_2$, $\eta = g_1/g_2$ where k_1, k_2 are the propagation constants, and g_1, g_2 are the gain coefficients of the two beams. Also $f(N_{1(2)})$ is a function that describes the carrier dependent gain, assumed to be of the form $f(N_{1(2)}) = \ln\left(\frac{N_{1(2)}N_{tr} + N_s}{N_{tr} + N_s}\right)$. N_s is a fitting constant, h is the linewidth enhancement (Henry factor), α is the internal loss, $\pi(z)$ is the periodic pumping coefficient ($\pi(z) = \pi_0$ for pumped and 0 for absorber sections), D is the carrier diffusion

coefficient, B is the spontaneous recombination coefficient and C is the Auger recombination rate. Normalized axes are used; z and x are defined as $z = z_{real}g$ and $x = x_{real}\sqrt{2\pi mg/\lambda_o}$. The parameters used were obtained from previous measurements on an InGaAs SQW wafer (also in chapter 3, [11]). Using $\mu = 1.003$, $\eta = 0.95$ the experiment was simulated, and output profiles plotted after 1cm of propagation (which corresponds to the device length). The results are shown in Figure 7.3.

The output simulations (Figure 7.3) show very similar results to the experiment curves. However, it was also desirable to analyze if two wavelength interactions in a dissipative system support stable bound solitons. The simulations in Figure 7.4 show the change in the beam profiles of the two beams for propagation distances much longer than the sample length. Here a sech profile ($|\psi_{1(2)}| = |\psi| \cdot \text{sech}(x/W)$) was fitted to the fields of the two beams since a sech profile is a reasonable approximation to the shape of dissipative semiconductor solitons [7]. The stability of each soliton was weakly affected by the existence of the second soliton at the other wavelength, and ψ_1 (for the TS beam) will be completely absorbed after a very long propagation distance. However during this energy exchange, these simulations predict a very interesting behavior, namely self-similar absorption and amplification. The beam *profiles* of the two beams do not change, but only their individual peak intensity is affected.

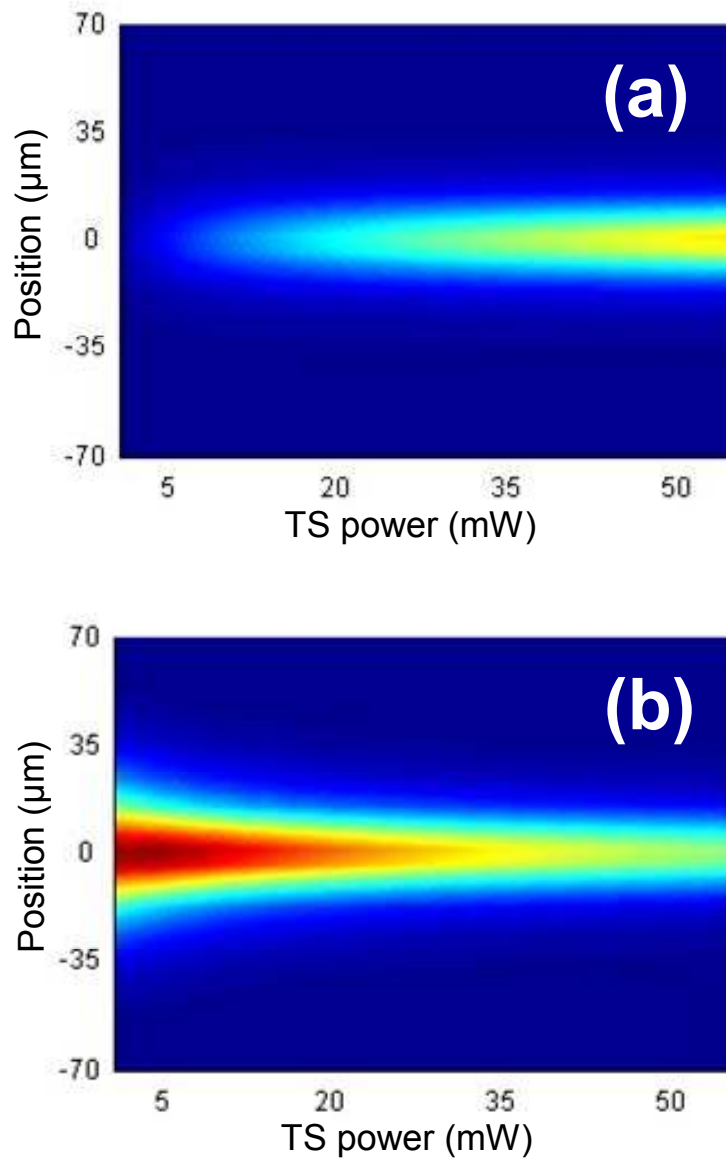


Figure 7.3 Simulations of the output from the PPSOA for two color interactions after 1 cm of propagation along the sample (a) TS power (b) LD power

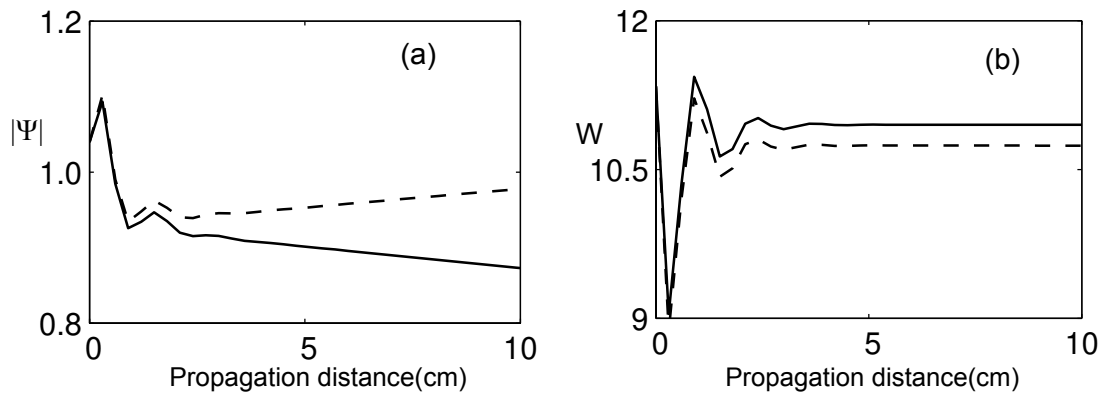


Figure 7.4 Solid line $|\psi_1|$, dashed line $|\psi_2|$ (a) The peak field values ($\sqrt{mW / \mu m}$) of the two beams, and (b) the fitted sech waists (μm)

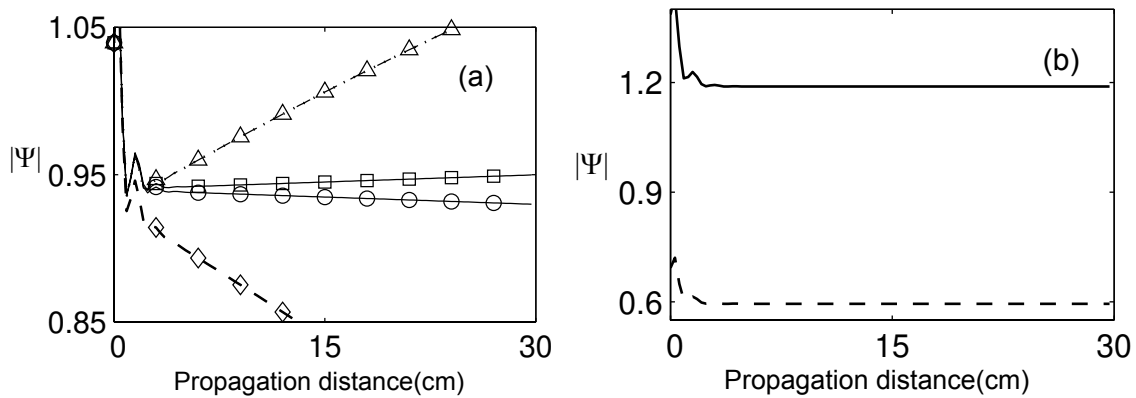


Figure 7.5 The peak field levels ($\sqrt{mW / \mu m}$) for two wavelength beam propagation simulations. (a) For $\mu=1.0$ and $\eta=0.95$, $|\psi_1|$ is shown by \diamond and $|\psi_2|$ by Δ ; and for $\mu=1.0$ and $\eta=0.95$, $|\psi_1|$ is \square , and $|\psi_2|$ is \circ . (b) For $\mu=1.0$ and $\eta=1.0$ coupled soliton formation occurs.

In order to analyze the source of this instability, a variety of different cases have been simulated in which the diffraction coefficient and the gain coefficient of the two beams are changed independently. In Figure 7.5a it is clear that both of these coefficients are a source of instability for stationary bound soliton states. When the gain of one beam is larger than the other one, the beams first try to stabilize to form bound pairs. Afterwards the beam with the stronger gain starts to grow, while the other beam loses intensity. Self similar amplification and absorption effects are also happening at the same time. Furthermore a diffraction coefficient change by itself could also lead to instability in forming this dissipative soliton bound state. Figure 7.5a shows that the beam with the larger propagation constant (k_1) starts to grow during propagation, while the other beam is absorbed. This effect is very different from that found for the coupled nonlinear Schroedinger equations, where bound solitons exist and they can propagate stably (as in the previous section solitons for different α). The bound state solitons have been identified only when the system modeling equations are completely symmetric, i.e. $\mu = 1.0$, $\eta = 1.0$. Such solitons propagate stably and form an infinitely bound family. The formation of these solitons depends on the input conditions. These solitons were also investigated by using a numerical relaxation algorithm [7.7]. Bound state solitons have only been found for the symmetric case and for the asymmetric cases no solution has been found. It was concluded that asymmetric equations do not support any soliton solutions, unstable or stable.

This property of dissipative solitons might be more general than the case studied here. Similar instabilities were found with a small change in diffraction in the coupled quintic complex Ginzburg-Landau equations (Equation 7.3) frequently used to study dissipative systems and given below.

$$\begin{aligned}
i\psi_{1(2)z} + \alpha_{1(2)}\psi_{1(2)xx} + (|\psi_{1(2)}|^2 + \gamma|\psi_{2(1)}|^2)\psi_{1(2)} = \\
i\delta\psi_{1(2)} + i\varepsilon(|\psi_{1(2)}|^2 + \theta|\psi_{2(1)}|^2)\psi_{1(2)} + i\beta\psi_{1(2)xx} \\
+ (i\mu - \nu)(|\psi_{1(2)}|^4 + |\psi_{2(1)}|^4)|\psi_{1(2)}
\end{aligned} \tag{7.3}$$

This equation has soliton solutions for specific parameters. In Figure 7.6 simulations were performed for soliton formation from a sech input at ($\beta=0.5$, $\varepsilon=0.38$, $\theta=1.0$, $\gamma=-0.1$, $\mu=-0.1$, $\nu=-0.1$). Again instabilities were found. Detailed numerical simulations need to be done for coupled dissipative systems in order to understand these instabilities.

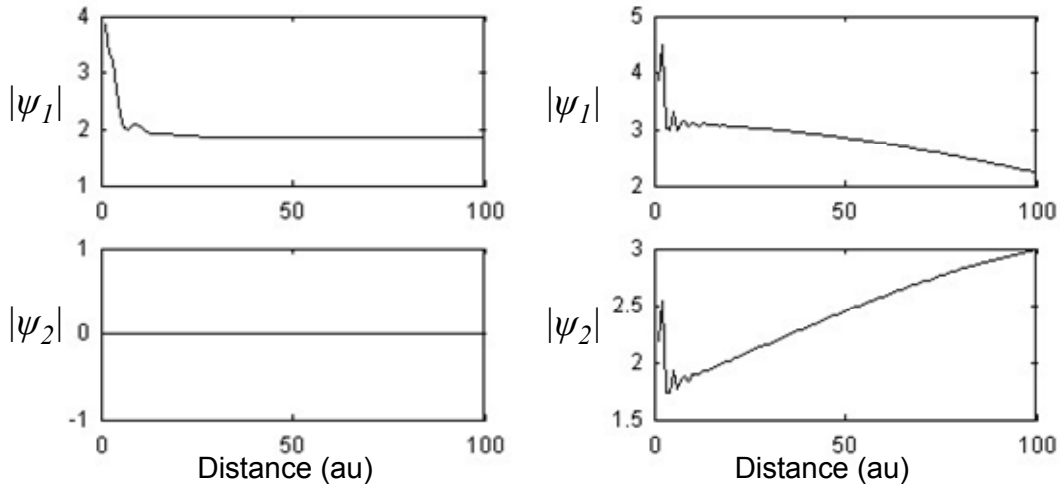


Figure 7.6 Propagation simulations based on the coupled quintic Ginzburg-Landau equations. (Left) Only one beam input. (Right) Two beams input.

In the current experiments it was not possible to observe this instability. Since for the small instability growth rates found theoretically, a very long device ($>30\text{cm}$) would be required in order to see these effects. Moreover very long sample lengths are not feasible with the current

fabrication technologies. However these results show that the stability of a dissipative soliton could easily be affected with another beam. Furthermore, stationary bound soliton states do not exist for multi-wavelength component beams.

7.3 Conclusions

In summary, multicolor solitary waves in PPSOA devices have been investigated. The instability caused by the diffraction and gain difference between two colors is very weak. However it prevents the formation of bound state solitons, unless two beams are experiencing the same diffraction and the same gain coefficients. Further investigations including one color in the transparent region, and one in the gain bandwidth of the semiconductor could be interesting.

CHAPTER EIGHT: CONCLUSIONS

“Finally, in conclusion, let me say just this.”
Peter Sellers

This PhD dissertation focused on the analysis and observation of stable solitons in semiconductor devices and their applications. A brilliant design; periodically patterned contacts on semiconductor devices was used in order to generate solitons propagating on a stable background. The solitons in these devices strongly depend on the material properties, and they do not form soliton families like the solitons in conservative systems. As a consequence of their formation with the balance of nonlinear gain and loss, the soliton profiles are always constant regardless of the inputs. This is not only a very interesting property at the fundamental level, but also could lead to an auto-signal property during applications.

The interactions of the solitons in these devices were examined in two limits, coherent and incoherent. On the coherent side, inputs from the same source generated a very strong interaction force through their interference. It has been shown that it is possible to generate all optical beam steering devices which can scan hundreds of micrometers at the output facets with phase difference control. Moreover the non-locality effect that is an outcome of the carrier diffusion did lead to the generation of additional solitons during these interactions. The incoherent interactions between beams from different sources resulted in very weak effects for soliton profiles. These interactions have resulted in the exchange of energies, that could also be used in soliton communication systems.

There are two completely analytical/numerical chapters in this thesis. One deals with Modulation Instability in dissipative systems. The analytical predictions on MI, are consistent with the soliton profiles that we have observed, and an experimental way to analyze all the spatial frequencies that could lead to filaments has been proposed and compared numerically with the analytical results. The other numerical chapter discusses new aspects of discrete dissipative systems. These systems are analyzed through a periodical contact pattern array device that could support discrete dissipative solitons. It is interesting to note that the arrays changed the zero-parameter property of the dissipative solitons. Thus observation of families of soliton solutions with multihumps should be possible. These multihump structures are phase locked. Thus discreteness in these arrays could help to observe a single lobe generation in the far-field with the application of solid-state laser pumping.

LIST OF REFERENCES

Chapter One

- 1.1. R. Eisberg and R. Resnick, *Quantum Physics*, Chapter 3 (John Wiley & Sons, 1985)
- 1.2. G. Assanto, M. Peccianti, and C. Conti, *Opt. & Phot. News* **14**, 44 (2003)
- 1.3. R. Y. Chia, E. Garmire, and C. H. Townes, *Phys. Rev. Lett.* **13**, 479 (1964); I. Talanov, *Radio Phys.* **7**, 254 (1964)
- 1.4. V. E. Zakharov and A. B. Shabat, *Sov. Phys. JETP* **34**, 62 (1971)
- 1.5. J. E. Bjorkholm and A. Ashkin, *Phys. Rev. Lett.* **32**, 129 (1974)
- 1.6. M. Segev, B. Crosignai, A. Yariv, B. Fischer, *Phys. Rev. Lett.* **68**, 923 (1992)
- 1.7. W. E. Torruellas et al., *Phys. Rev. Lett.* **74**, 5036 (1995)
- 1.8. Yu. N. Karamzin and A. P. Sukhorukov, *Sov. Phys. JETP* **41**, 414 (1975)
- 1.9. D. N. Christodoulides, R. I. Joseph, *Phys. Rev. Lett.* **62**, 1746 (1989)
- 1.10. B. J. Eggleton et al., *Phys. Rev. Lett.* **76**, 1627 (1996)
- 1.11. D. N. Christodoulides, R. I. Joseph, *Opt. Lett.* **13**, 794 (1988)
- 1.12. H. S. Eisenberg et al., *Phys. Rev. Lett.* **81**, 3383 (1998)
- 1.13. V. Yu. Bazhenov, V.B. Taranenko, and V.M. Vasnetsov, *Proc. SPIE* **1840**, 183 (1992)
- 1.14. M. Saffman, D. Montgomery, and D.Z. Anderson, *Opt. Lett.* **19**, 518 (1994).

- 1.15. N.N. Rosanov, *Progress in Optics XXXV*, edited by E. Wolf, (Elsevier Science, North-Holland, 1996).
- 1.16. N. N. Akhmediev and A. Ankiewicz, *Solitons: Nonlinear Pulses and Beams* (Chapman and Hall, London, 1997).
- 1.17. M. Saffman, D. Montgomery, and D.Z. Anderson, *Opt. Lett.* **19**, 518 (1994).
- 1.18. Z. Bakonyi et al., *J. Opt. Soc. Am. B* **19**, 487 (2002).
- 1.19. C.J. Chen, P. Wai, and C.R. Menyuk, *Opt. Lett.* **17**, 417 (1992).
- 1.20. V.B. Taranenko, I. Ganne, R.J. Kuszelewicz, and C.O. Weiss, *Appl. Phys. B* **72**, 377 (2001).
- 1.21. S. Barland et al., *Nature* **419**, 699 (2002).
- 1.22. G. Khitrova et al., *Phys. Rev. Lett.* **70**, 920 (1993).
- 1.23. C. Kutsche, P. LiKamWa, J. Loehr, and R. Kaspi, *Electron. Lett.* **34**, 906 (1998)
- 1.24. E. A. Ultanir, D. Michaelis, F. Lederer and G. I. Stegeman, *Optics Lett.* **28** (4), 251 (2003)
- 1.25. M. Mitchell and M. Segev, *Nature* **387**, 880 (1997)

Chapter Two

- 2.1. P. Bhattacharya, *Semiconductor Optoelectronic Devices* (Prentice Hall, New Jersey, Second Edition, 1997)
- 2.2. L. A. Coldren and S. W. Corzine, *Diode Lasers and Photonic Integrated Circuits*, (John Wiley & Sons, 1995)
- 2.3. B. E. A. Saleh and M. C. Teich, *Fundamentals of Photonics*, (John Wiley & Sons, 1991)

- 2.4. G. P. Agrawal, N. K. Dutta, *Semiconductor Lasers*, (Kluwer Academic Publishers, Second Edition, 1993)
- 2.5. H. Kroemer, *Proc. IREE* **51**, 1782 (1963)
- 2.6. Patent by Zh. I. Alferov and R. F. Kazarinov at Ioffe Physico-Technical Institute, Leningrad (now St. Petersburg)
- 2.7. G. P. Agrawal, *J. Appl. Phys.* **56**, 3100 (1984)
- 2.8. W. W. Chow, S. W. Koch and M. Sargent III, *Semiconductor Laser Physics* (Springer-Verlag, Berlin, 1994)
- 2.9. O. Hess and T. Kuhn, *Phys. Rev. A* **54**, 3347 (1996)
- 2.10. G. E. Schentegel et al, *IJHSES* **9**, 901 (1998)
- 2.11. D. J. Bossert, D. Gallant, *IEEE Photon. Technol. Lett.* **8**, 322 (1996).
- 2.12. S. Fauve and O. Thual, *Phys. Rev. Lett.* **64**, 282 (1990).
- 2.13. S. Longhi and A. Geraci, *Appl. Phys. Lett.* **67** (21) 3062 (1995).
- 2.14. S. V. Federov, A. G. Vladimirov, G. V. Khodova and N. N. Rosanov, *Phys. Rev. E* **61** (5) 5814 (2000) .
- 2.15. D. Mehuys, R. J. Lang, M. Mittelstein, J. Salzaman and A. Yariv, *IEEE J. Quant. Elect.* **23** (11), 1909-1920 (1987)
- 2.16. H. Paxtion, G. C. Dente, *J. Appl. Phys.* **70**, 2921 (1991).
- 2.17. L. Goldberg, M. R. Surette and D. Mehuys, *Appl. Phys. Lett.* **62**, 2304 (1993).
- 2.18. K. Okamoto, *Fundamentals of Optical Waveguides*, Chapter 7 (Academic Press, San Diego, 2000)
- 2.19. W.H. Press, S. A. Teukolsky, W.T. Vetterling, B.P. Flannery, *Numerical Recipes in Fortran 77*, Chapter 17 (Cambridge University Press, Second Edition, 1992)
- 2.20. N. N. Akhmediev, V. V. Afanasjev and J. M. Soto, *Phys. Rev. E* **53** (1) 1190 -1201 (1996).
- 2.21. Z. Bakonyi, , D. Michaelis, U. Peschel, G. Onishchukow and F. Lederer, *J. Opt. Soc. Am. B* **19** (3), 487 (2002).

Chapter Three

- 3.1. L. A. Coldren and S. W. Corzine, *Diode Lasers and Photonic Integrated Circuits*, Chapter 4, (John Wiley & Sons, 1995)
- 3.2. D. J. Bossert, D. Gallant, *IEEE Photon. Technol. Lett.* **8**, 322 (1996).
- 3.3. S. Kristjansson, N. Eriksson, P. Modh and A. Larsson, *IEEE J. Quantum Electron.* **37**, 1441 (2001).

Chapter Four

- 4.1. G. I. Stegeman and M. Segev, *Science* **286**, 1518 (1999).
- 4.2. M. Peccianti, K. A. Brzdakiewicz and G. Assanto, *Optics Lett.* **27**, 1460 (2002)
- 4.3. N. N. Akhmediev and A. Ankiewicz, *Solitons: Nonlinear Pulses and Beams* (Chapman and Hall, London, 1997).
- 4.4. E. A. Ultanir, G. I. Stegeman, C. H. Lange, and F. Lederer, *Optics Lett.*, **29** (3), 283 (2004)
- 4.5. A. W. Snyder and D. J. Mitchell, *Science* **276**, 1538 (1997)
- 4.6. E. A. Ultanir, G. I. Stegeman, D. Michaelis, C.H. Lange and G. I. Stegeman, *Phys. Rev. Lett.* **90** , 253903 (2003)
- 4.7. *IEEE J. Quant. Elect.* **39**, 1-64 (2003); Feature section on spatial solitons (Issue 1), Editor: F. Lederer
- 4.8. B. Luther-Davies and Y. Xiaoping, *Optics Lett.* **17**, 496 (1992)

- 4.9. T.T. Shi and S. Chi, *Optics Lett.* **15**, 1123 (1990)
- 4.10. N.N. Rosanov, *Spatial Hysteresis and Optical Patterns* (Springer 2002)

Chapter Five

- 5.1. G. P. Agrawal, *Nonlinear Fiber Optics*, 2nd Ed (Academic Press, San Diego, 1995), Chap5
- 5.2. V.I. Bespalov, V.I. Talanov, *JETP Lett.* **3**, 307 (1966), A. Hasegawa, W. F. Brinkman, *J. Quantum Electron.* **16**, 694 (1980), E. M. Dianov, P. M. Mamyshev, A.M. Prokhorov, S. V. Chernikov, *Opt. Lett.* **14**, 1008 (1989)
- 5.3. M. Soljagic, M. Segev, T. Coskun, D.N. Christodoulides, A. Vishwanath, *Phys. Rev. Lett.*, **84**, 467 (2000)
- 5.4. D. Kip, M. Soljagic, M. Segev, E. Eugeniya, D.N. Christodoulides, *Science* **290** 495 (2000)
- 5.5. M. Nakazawa, K. Suzuki, and H. A. Haus, *Phys. Rev. A* **38**, 5193 (1988); *IEEE J. Quantum Electron.* QE-**25**, 2036 (1989)
- 5.6. M. Haelterman, S. Trillo, and S. Wabnitz, *Phys. Rev. A* **47**, 2344 (1993); *Opt. Commun.* **91**, 401 (1992); *Opt. Lett.* **17**, 745 (1992)
- 5.7. D. Michaelis, U. Peschel, F. Lederer, *Phys. Rev. A* **56** (5) R3366 (1997), Spinelli L, Tissoni G, Brambilla M, Prati F, Lugiato LA, *Phys. Rev. A* **58** (3), 2542 (1998)
- 5.8. L. Goldberg, M. R. Surette and D. Mehuys, *Appl. Phys. Lett.* **62** (19), (1993)

- 5.9. A. H. Paxton and G. C. Dente, *J. Appl. Phys.* **70** (6), (1991)
- 5.10. M. I. Carvalho, S. R. Singh, D. N. Christodoulides, *Opt. Comm.* **126**, 167 (1996)
- 5.11. S. Trillo and P. Ferro, *Opt. Lett.* **20**, 438 (1995)
- 5.12. P. Ferro and S. Trillo, *Phys. Rev. E* **51**, 4994 (1995)

Chapter Six

- 6.1. A. L. Jones, *J. Opt. Soc. Am.* **55**, 261 (1965)
- 6.2. S. Somekh et al., *Appl. Phys. Lett.* **22**, 46 (1973)
- 6.3. E. Yablonovitch, *Phys. Rev. Lett.* **58**, 2059 (1987)
- 6.4. P. Russel, *Science* **299**, 358 (2003)
- 6.5. D. Hermann, M. Frank, K. Busch and P. Wolfle, *Optics Express* **8** (3), 167 (2000)
- 6.6. D. Mandelik, H. S. Eisenberg, Y. Silberberg, R. Morandotti, and J.S. Aitchison, *Phys. Rev. Lett.* **90**, 053902 (2003)
- 6.7. D. N. Christodoulides and R. I. Joseph, *Opt. Lett.* **13**, 794 (1988)
- 6.8. H. S. Eisenberg, Y. Silberberg, R. Morandotti, A. R. Boyd and J. S. Aitchison. *Phys. Rev. Lett.* **81**, 3383 (1998)
- 6.9. R. Iwanow et al, CLEO/QELS 2003, QThK4 “Discrete Quadratic Solitons in Waveguide Arrays”
- 6.10. J. W. Fleischer, T. Carmon, M. Segev, N.K. Efremidis and D. N. Christodoulides, *Phys. Rev. Lett.* **90**, 023902 (2003)
- 6.11. U. Peschel, D. Michaelis, C.O. Weiss, *IEEE Journal of Quant. Elect.* **39**, 54 (2003)

- 6.12. E. A. Ultanir, G. I. Stegeman, D. Michaelis, C.H. Lange and G. I. Stegeman, *Phys. Rev. Lett.* **90**, 253903 (2003).
- 6.13. D.N. Christodoulides, F. Lederer, Y. Silberberg, *Nature* **424** 817 (2003)
- 6.14. N. K. Efremidis and D. N. Christodoulides, *Phys. Rev. E* **67**, 026606 (2003)
- 6.15. K. Maruno, A. Ankiewicz A, N. Akhmediev, *Opt. Comm.* **221**, 199 (2003)
- 6.16. K. Staliunas, *Phys. Rev. Lett.* **91**, 053901 (2003)
- 6.17. E. J. Bochove, P.K. Cheo, G.G. King, *Opt. Lett* **28**, 1200 (2003)
- 6.18. D. Botez, *Diode laser arrays*, (Cambridge University Press, 1994)
- 6.19. L. Goldberg and D. Mehuys, *Appl. Phys. Lett.* **61**, 633 (1992)
- 6.20. E. A. Ultanir, D. Michaelis, F. Lederer and G. I. Stegeman, *Optics Lett.* **28**, 251 (2003)
- 6.21. D. J. Bossert, D. Gallant, *IEEE Photon. Technol. Lett.* **8**, 322 (1996).
- 6.22. P. Yeh, A. Yariv and C.S. Hong, *J. Opt. Soc. Am.* **67**, 423 (1977)
- 6.23. P. St. Russell, *Appl. Phys. B* **39**, 231 (1986)
- 6.24. E. A. Ultanir, G. I. Stegeman, C.H. Lange and G. I. Stegeman, *Optics Lett.* **29** (3), 283 (2004)

Chapter Seven

- 7.1. J. U. Kang, G. I. Stegeman, J. S. Aitchison, *Opt. Lett.* **20**, 2069 (1995)
- 7.2. J. Meier, et al, *Phys. Rev. Lett.*, **91**, 143907 (2003)
- 7.3. W.E. Torruellas et. al., *Phys. Rev. Lett.*, **74**, 5036 (1995)
- 7.4. M. Mitchell and M. Segev, *Phys. Rev. Lett.*, **80**, 4657 (1998)

- 7.5. C. R. Menyuk, *J. Opt. Soc. Am. B*, **5**, 392 (1988); G. P. Agrawal, *J. Opt. Soc. Am. B*, **7**, 1072 (1990); N. N. Akhmediev, A. V. Buryak, J. Soto-Crespo, and D. R. Andersen, *J. Opt. Soc. Am. B*, **12**, 434 (1995).
- 7.6. H. T. Tran and R. A. Sammut, *Phys. Rev. A*, **52**, 3170 (1995)
- 7.7. E. A. Ultanir, G. I. Stegeman, D. Michaelis, C.H. Lange and G. I. Stegeman, *Phys. Rev. Lett.* **90**, 253903 (2003).
- 7.8. E. A. Ultanir, G. I. Stegeman, C. H. Lange, and F. Lederer, *Opt. Lett.*, **29**, 283 (2004)
- 7.9. M. Peccianti, et al, *Appl. Phys. Lett.* **81**, 3335 (2002)
- 7.10. B. A. Malomed and H. G. Winful, *Phys. Rev. E*, **53**, 5363 (1996)
- 7.11. D. J. Bossert and D. Gallant, *IEEE Photon. Technol. Lett.*, **8**, 322 (1996).